DRAG ANALYSIS OF DIFFERENT SHIP MODELS USING COMPUTATIONAL FLUID DYNAMICS TOOLS

by

SALINA AKTAR

MASTER OF PHILOSOPHY

IN

MATHEMATICS

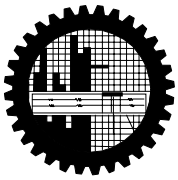

Department of Mathematics

BANGLADESH UNIVERSITY OF ENGINEERING AND TECHNOLOGY, DHAKA.

June, 2012

The thesis titled

DRAG ANALYSIS OF DIFFERENT SHIP MODELS USING COMPUTATIONAL FLUID DYNAMICS TOOLS

Submitted by

Salina Aktar

Student No. 100509003, Registration No. 100509003, Session: October-2005, a part time student of M. Phil. (Mathematics) has been accepted as satisfactory in partial fulfillment for the degree of

Master of Philosophy in Mathematics

June 26, 2012

BOARD OF EXAMINERS

1.	**Dr. Md. Abdul Alim** Associate Professor Dept. of Mathematics, BUET, Dhaka.	Chairman (Supervisor)
2.	**Dr. Goutam Kumar Saha** Associate Professor Dept. Naval Architecture and Marine Eng., BUET, Dhaka.	Member (Co-Supervisor)
3.	**Dr. Md. Elias** Professor & Head of the Dept. Dept. of Mathematics, BUET, Dhaka.	Member (Ex-Officio)
4.	**Dr. Md. Mustafa Kamal Chowdhury** Professor Dept. of Mathematics, BUET, Dhaka.	Member
5.	**Dr. Amal Krishna Halder** Professor Dept. of Mathematics, University of Dhaka, Dhaka	Member (External)

DECLARATION

It is hereby declared that this thesis or any part of it has not been submitted else where for the award of any degree or diploma.

Salina Aktar

DEDICATION

Dedicated

to

My Respectable Parents and Beloved Husband

ACKNOWLEDGEMENT

All praises and gratitude belong to Allah (Most Gracious and Most Merciful) for making things and situations congenial and favorable for me to complete this thesis.

First of all I would like to express my indebtedness to my respected supervisor Dr. Md. Abdul Alim, Associate Professor, Department of Mathematics and co-supervisor Dr. Goutam Kumar Saha, Associate Professor, Department of Naval Architecture and Marine Engineering, Bangladesh University of Engineering and Technology, Dhaka, Bangladesh. Especially, I acknowledge my gratitude to Dr Alim and Dr. Saha for their tireless guidance and support throughout the research. Their time input and advise were of immense help in completing this thesis in due time and I will be ever grateful to them. Besides I would like to be grateful to all of my teachers in the Department of Mathematics, BUET, for their kind help and cooperation.

I must mention here that the researchers listed in the reference section and the members of Fluent User Forum (FUF) with whom I have exchanged ideas through internet.

Moreover I would be pleased to my family members, specially my mother and my husband, because of their sacrifice, cooperation and mental support during my research.

Above all, all thanks are due to Almighty Allah for making things and situations congenial and favorable for me for the task undertaken.

ABSTRACT

Drag analysis based on CFD (computational Fluid Dynamics) simulation has become a decisive factor in the development of new, economically efficient and environmentally friendly ship hull forms. Recently, computational Fluid Dynamics (CFD) has been experiencing rapid advances due to both computer technology progress and efficient algorithms that have been developed to solve the Navier-Stokes(N-S) equations used in the flow analysis around ship hulls. Three-dimensional finite volume method (FVM) based on Reynolds averaged Navier-Stokes equations (RANS) has been used to simulate incompressible flow around two conventional models namely Wigely parabolic and Series 60 hull in steady-state condition. Different turbulence models such as Standard k-ε, Realizable k-ε and Shear stress transport (SST) k-ω are used with standard wall function to measure the drag coefficient. It is observed that k-ε turbulence model shows better performance than any other model. The numerical solutions of the governing equations have been obtained using commercial CFD software package FLUENT 6.3.26. Model tests conducted with these two models are simulated to measure various types of drag coefficient at different Froude numbers. The numerical results in terms of pressure coefficient and drag coefficient for different Froude numbers have been shown graphically or in the tabular form. The agreement between the numerical results and the experimental indicates that the implemented code is able to reproduce correctly the drag coefficient, pressure field, velocity field and the free-surface elevation around the Wigely parabolic and Series 60 hull. Velocity vectors as well as contour of pressure distribution have also been displayed graphically. The computed results show good agreement with the experimental measurements/numerical results at a Froude number below 0.3.

CONTENTS

DECLARATION ..... **iii**

DEDICATION ..... **iv**

ACKNOWLEDGEMENT ..... **v**

ABSTRACT ..... **vi**

LIST OF TABLES ..... **xiii**

LIST OF FIGURES ..... **xv**

CHAPTER 1 ..... **1**

1.INTRODUCTION **1**

1.1 What is Computational Fluid Dynamics? 1

1.2 Computational Fluid Dynamics in Research and Development 1

1.3 CFD Advantages versus Disadvantages 2

1.4 CFD in Ship Design Practice and Ship Hydrodynamics Analysis 3

1.5 Previous Research 5

1.6 Research Objectives 9

CHAPTER 2 ..... **10**

2. COMPUTATIONAL FLUID DYNAMICS MODELING CONSIDERATIONS **10**

2.1 Discretization Methods in Computational Fluid Dynamics 10

2.1.1 Finite Difference Method (FDM) 11

2.1.2 Finite Element Method (FEM) 11

2.1.3 Finite Volume Method (FVM) 11

2.1.4 Boundary Element Method (BEM) 12

2.2 Basics of Fluid Dynamics 12

2.2.1 Reynold's Number 12

2.2.2 Froude Number 13

2.3 Laminar and Turbulent Flow 13

2.4 Drag Forces 15

2.4.1 Frictional and Viscous Drag 16

2.4.2 Residuary and Wave Making Drag 16

2.5 Grid Generation 17
2.5.1 Solution Dependence on Grid 17
2.5.2 Structured Grids 18
2.5.3 Unstructured Grids 19
2.5.4 Hybrid Grids 21
2.6 Computational Fluid Dynamics Solver 22
2.7 The Fluent Code 23
CHAPTER 3 25
3. THEORETICAL BACKGROUND 25
3.1 Mathematical Formulations 25
3.1.1 Governing Equations 26
3.2 Solution using Finite Volume Method 27
3.3 Integration of the Transport Equation 27
3.4 Approximation of Integrals 29
3.5 Interpolation 30
3.6 Finite Volume Method for Three-Dimensional Diffusion Problems 32
3.7 Linear Equation System 33
3.8 Solution Algorithm for Pressure-Velocity Coupling 35
3.9 Spatial Discretisation 39
3.10 Turbulence Modeling 40
3.10.1 The Spalart-Allmaras (S-A) Model 44
3.10.2 The *k*-ε Model 45
3.10.2.1 The Standard *k*-ε Model 45
3.10.2.2 Realizable *k*- ε Model 46
3.10.3 The *k*-ω Turbulence Model 47
3.10.3.1 SST *k*-ω model 47
3.11 Ideal Turbulence Model 48
3.12 Grid Considerations for Turbulent Flow Simulations(Y^+) 49
CHAPTER 4 51
4. NUMERICAL SIMULATION 51
4.1 Simulation Using FLUENT 6.3.26 Based on Finite Volume Method 51
4.2 Steady Flow over the hull of a ship 52

4.2.1 Geometric Modeling 52
4.3 Computational Approaches to Free Surface Modelling 53
4.3.1 Free Surface 53
4.4 Computational Domain 54
4.5 Grid Generation 55
4.5.1 Mesh Studies 57
4.5.2 Grid Study 57
4.6 Initial Condition 58
4.7 Boundary Condition 59
4.8 Solver Initialization and Flow Solution 61
CHAPTER 5 64
5.RESULT AND DISCUSSION 64
5.1 Introduction 64
5.2 Test Cases 66
5.2.1 Wigley Parabolic Hull 66
5.2.1.1 Grid Independence and C_D Calculation 67
5.2.1.2 Comparison with other Researchers 71
5.2.1.3 Comparison with experimental result 72
5.2.2 Series 60 Hull 73
5.2.2.1 Grid Independence and C_D Calculation 74
5.2.2.2 Comparison with other Researchers 78
5.2.2.3 Comparison with experimental result 79
5.3 Effect of Turbulence Model 80
5.4 Improvement of the Convergence 81
5.5 Numerical Scheme 83
5.4 Free Surface Generation 84
5.5 Simulation Results with a Tetrahedral Mesh 84
CHAPTER 6 126
6. CONCLUSION AND RECOMMENDATIONS 126
6.1 Conclusion 126
6.2 Recommendation for further study 127
REFERENCE 128

APPENDICES.....131
Appendix A: 131
Appendix B:.....133
Appendix C:.....135
Appendix D: 137
Appendix E:.....139

NOMENCLATURE

a_{nb}	neighbouring coefficient
$\vec{a}$	fluctuating vector
A	reference surface area
A_f	reference face area
$\vec{A}$	surface area vector
B	beam of hull
C_B	block coefficient
C_D	drag coefficient
C_f	co-efficient of friction
C_F	frictional drag co-efficient
R_F	frictional resistance
C_V	viscous drag coefficient
C_W	wave drag coefficient
$C_{1\varepsilon}$,$C_{2\varepsilon}$, $C_{3\varepsilon}$	turbulence constants
dA	surface element
D	draft of hull
D_ω	cross-diffusion term
f_i	flux in the *i*th direction
F_i	convective flux
F_D	drag forces
Fn	Froude number
G	acceleration due to gravity
G_k	generation of turbulent kinetic energy
G_b	generation of turbulent kinetic energy due to buoyancy
$\tilde{G}_k$	generation of turbulent kinetic energy due to mean velocity gradients
G_ω	generation of ω
G_ν	production of turbulent viscosity
I	turbulence intensity
k	turbulent kinetic energy

l	length scale
L	length of hull
$\vec{n}$	unit normal vector
N_{faces}	number of faces enclosing cell
p	pressure
p^*	initial pressure field
p'	correction to pressure field
Re	Reynolds number
S	source term
S_p	function of φ
S_x, S_y, S_z	source term in x,y and z-direction
S_u	constant term
$S_{\tilde{\nu}}$	user-defined source term (for S-A)
S_φ	source of φ per unit volume
S_k ,S_ε	user-defined source terms (for k-ε)
S_k ,S_ω	user-defined source terms (for k-ω)
u,v,w	ith , jth and wth velocity components in Cartesian coordinates
$\vec{u}$	*flux*
u'	fluctuating velocity
u^*	frictional velocity
V	cell volume
U_{avg}	mean flow velocity
$\vec{U}$	constant velocity
U,V,W	mean velocity components in three dimensional axes
$\vec{V}_f$	mass flux face
x_i, x_j, x_k	ith , jth ,kth location components in Cartesian coordinates
Y_k,Y_ω	dissipation of k and ω due to turbulence
y	distance from wall surface
y^+	dimensionless parameter representing a local Reynold's number
Y_M	fluctuating dilatation
Y_V	destruction of turbulent viscosity

Greek symbols

ρ	density of fluid
φ	fluctuating parameter
μ	kinematic viscosity
ν	molecular kinematic viscosity
ε	turbulent dissipation
α	underrelaxation parameter
v_x	axial velocity
v_r	radial velocity
τ_{ij}	momentum transport
τ_w	wall shear
$\bar{\nu}$,	turbulent kinematic viscosity
ρ_{ref}	reference density
σ_k,σ_ε	turbulent Prandtl numbers for k and ε respectively
$\sigma_{\tilde{\nu}}$	constant term
Γ_k, Γ_ω	effective diffusivity of k and ω respectively
τ_w	shear stress at the wall
τ_{xz}, τ_{xy}, τ_{yz}	shear stress
τ_{xx}, τ_{yy}, τ_{zz}	normal stress
Γ_φ	diffusion coefficient for φ

LIST OF TABLES

Table No.	Caption	Page No.
4.1	Principal Particulars of Wigley and Series 60 Model	55
4.2	Mesh Analysis of Wigley and Series 60 Model	57

5.1	Grid Structure of Wigley Hull	68
5.2	Computed Value of C_D, C_V and C_W by Standard k-ε (SKE) Model	68
5.3	Comparison of Computed C_D by Different Turbulent Model	69
5.4	Comparison of Computed C_W of Various Turbulence Models and Boundary Element (BEM) Method.	70
5.5	Comparison of Computed C_D for Wigley hull	71
5.6	Comparison with the Experimental Results	72
5.7	Comparison with Other Numerical Result	73
5.8	Grid Structure of Series 60 Hull	75
5.9	Computed Value of C_D, C_V and C_W by Standard k-ε (SKE) Model.	76
5.10	Comparison of Computed C_D by Various Turbulent Models	77
5.11	Comparison of Computed C_W of Various Turbulence Models and Boundary Element (BEM) Method.	78
5.12	Comparison of Computed C_D for Series 60 hull	79
5.13	Comparison with the Experimental Results	79

LIST OF FIGURES

Figure No.	Caption	Page No.
2.1	(a)Laminar and (b)Turbulent Path Line .	14
2.2	Laminar and Turbulent Velocity Profiles.	14
2.3	Structured Multiblock Mesh using Point to Point.	18
2.4	Unstructured Mesh Consisting of Triangles and Tetrahedral Elements.	20
2.5	Quasi Structured Prismatic Mesh.	21
3.1	Three Dimensional Co-ordinate Systems for a Hull Design.	25
3.2	A Cell in Three Dimensions with Its Neighbouring Points and Faces.	28
3.3	The Upwind Difference Scheme for One Dimensional Flow.	31
3.4	Flow Chart for SIMPLE Algorithm.	38
4.1	(a) Hull of Model Wigley (b) Hull of Model Series 60.	54
4.2	Grid Lines in Mesh Around the Hull of Wigley	56
4.3	Grid Lines in Mesh Around the Hull of Series 60.	56
4.4	Grid Display with Nodes Around the Hull of (a) Wigley and (b) Series 60.	58
4.5	Schematic Diagram of the Flow Field around Hull with Boundary Condition.	60
5.1	Grid of (a) Wigley hull and (b) its computational domain.	67-68

5.2	Various Drag Coefficients Vs Froude Numbers.	69
5.3	Drag Coefficients for Different Models Vs Froude Numbers.	70
5.4	Wave Drag Coefficient Vs Froude Numbers.	71
5.5	Drag Coefficient Vs Froude Numbers.	73
5.6	Grid of (a) Series 60 hull and (b) Its Computational Domain.	74-75
5.7	Various Drag Coefficients Vs Froude Numbers.	76
5.8	Drag Coefficients of Different Models Vs Froude Numbers.	77
5.9	Wave Drag Coefficient Vs Froude Numbers .	78
5.10	Drag Coefficient Vs Froude Numbers.	80
5.11	Residual History of Model Wigley for Fn=0.476.	81
5.12	Residual History of Model Series 60 for Fn=0.476.	82
5.13	Drag Convergence History of Model Wigley.	82
5.14	Drag Convergence History of Model Series 60.	82
5.15	Contours of Pressure Coefficient of Wigley Hull for a) Fn = 0.173,b)Fn = 0.205, c) Fn = 0.267, d) Fn = 0.355 and e) Fn = 0.476.	86 -87
5.16	Contours of Pressure Coefficient of Wigley Hull and the Free Surface for a)Fn = 0.173,b)Fn = 0.205, c) Fn = 0.267,d) Fn = 0.355 and e) Fn = 0.476.	88 -89
5.17	Close Up View of Contours of Pressure Coefficient of Wigley Hull and Free Surface for a)Fn = 0.173,b)Fn = 0.205, c) Fn = 0.267, d) Fn = 0.355 and e) Fn = 0.476.	90-91
5.18	Contours of Wall Y+ of Wigley Hull for a)Fn = 0.173,b)Fn	92-93

	= 0.205, c) Fn = 0.267,d) Fn = 0.355 and e) Fn = 0.476.	
5.19	Contour Position of Free Surface about z axis of Wigley Hull for (a) Fn = 0.173, (b) Fn = 0.205, (c) Fn = 0.267, d) Fn = 0.355 and e) Fn = 0.476.	94-95
5.20	Contours of Velocity Magnitude of Wigley Hull and the Reference Surface for a)Fn = 0.173,b)Fn = 0.205, c) Fn = 0.267, d) Fn = 0.355 and e) Fn = 0.476.	96-97
5.21	Contours of Close up View of Velocity Magnitude of Wigley Hull and the Reference Surface for a) Fn = 0.173,b)Fn = 0.205, c) Fn = 0.267, d) Fn = 0.355 and e) Fn = 0.476.	98-99
5.22	Contours of Velocity Magnitude of Wigley Hull and Symmetric Top Side of the Volume for a)Fn = 0.173,b)Fn = 0.205, c) Fn = 0.267,d) Fn = 0.355 and e) Fn = 0.476.	100-101
5.23	Contours of Velocity Vectors of Wigley Hull and the Reference Surface for a) Fn = 0.173,b)Fn = 0.205, c) Fn = 0.267,d) Fn = 0.355 and e) Fn = 0.476.	102-103
5.24	Plot of Pressure Co-efficient of Wigley Hull and Free Surface for a) Fn = 0.173,b)Fn = 0.205, c) Fn = 0.267,d) Fn = 0.355 and e) Fn = 0.476.	104-105
5.25	Close Up View of Pressure Co-efficient of Wigley Hull and the Reference Surface for a)Fn = 0.173,b)Fn = 0.205, c) Fn = 0.267,d) Fn = 0.355 and e) Fn = 0.476.	106-107
5.26	Contours of Pressure Coefficient of Series 60 Hull for a)Fn = 0.173,b)Fn = 0.205, c) Fn = 0.267, d) Fn = 0.355 and e) Fn = 0.476	108-109
5.27	Contour Position of Free Surface about z Axis of Series 60 Hull for (a) Fn = 0.173, (b) Fn = 0.205, (c) Fn = 0.267, d) Fn =	

	0.355 and e) Fn = 0.476.	110-111
5.28	Contours of Pressure Coefficient of Series 60 Hull and the Free Surface for a)Fn = 0.173,b)Fn = 0.205, c) Fn = 0.267, d) Fn = 0.355 and e) Fn = 0.476.	112-113
5.29	Close Up View of Contours of Pressure Coefficient of Series 60 Hull and Free Surface for a)Fn = 0.173,b)Fn = 0.205, c) Fn = 0.267, d) Fn = 0.355 and e) Fn = 0.476.	114-115
5.30	Contours of Wall Y+ of Series 60 Hull for a)Fn = 0.173,b)Fn = 0.205, c) Fn = 0.267,d) Fn = 0.355 and e) Fn = 0.476.	116-117
5.31	Contours of Velocity Magnitude of Series 60 Hull and the Reference Surface for a)Fn = 0.173,b)Fn = 0.205, c) Fn = 0.267, d) Fn = 0.355 and e) Fn = 0.476.	118-119
5.32	Contours of Velocity Magnitude of Series 60 Hull and Symmetric Top Side of the Volume for a)Fn = 0.173,b)Fn = 0.205, c) Fn = 0.267,d) Fn = 0.355 and e) Fn = 0.476	120-121
5.33	Contours of Velocity Vectors of Series 60 hull and the Reference surface for a)Fn = 0.173,b)Fn = 0.205, c) Fn = 0.267,d) Fn = 0.355 and e) Fn = 0.476.	122-123
5.34	Plot of Pressure Co-efficient of Series 60 Hull and free Surface for a) Fn = 0.173,b)Fn = 0.205, c) Fn = 0.267,d) Fn = 0.355 and e) Fn = 0.476.	124-125

CHAPTER 1

1.INTRODUCTION

1.1 What is Computational Fluid Dynamics?

Computational fluid dynamics, usually abbreviated as CFD, is a branch of fluid mechanics that uses numerical methods and algorithms to solve and analyze problems that involve in fluid flows ,heat transfer, mass transfer and associated phenomena by means of mathematical modeling (partial differential equations), numerical methods (discretization and solution techniques),software tools (solvers, pre- and post- processing utilities).This is a very useful tool to solve the basics equations that model the flow movement. The majority of these equations do not have any analytical solution. For these reasons we resort to numerical analysis with CFD. The objective of these tools is to solve approximate (numerically) the flow basic equations whose solutions give us the movements and other characteristics of the flow. These techniques discretise the spatial and time domain for reaching the solution.

1.2 Computational Fluid Dynamics in Research and Development

Computational fluid dynamics (CFD) is one of the branches of fluid mechanics that uses numerical methods and algorithms to solve and analyze problems in fluid flows. Computers are used to perform the millions of calculations required to simulate the interaction of fluids and gases with the complex surfaces used in engineering. Research in fluid flow problems is necessary for the development of new fluid based systems. Computational Fluid Dynamics (CFD) has the power to model fluid flow and heat transfer in an abundance of situations. With the advent of more powerful computers and more comprehensive computer codes, CFD has come to the forefront

as a legitimate and effective research tool. CFD analysis can be much more cost effective compared to experimental models particularly in the ship design process. Since changes can be made quickly and easily to almost any characteristic of the simulation. Simulations can also be set up more quickly and easily than experimental methods. However, since it is a computer based solution technique, the results must be verified against experimental data. Not every simulation needs to be compared with experimental values. Only a few base cases are compared for validation purposes and then it is assumed safe to say that the other CFD simulations in that range are valid. Even if some simulations are analyzed both experimentally and numerically, CFD is still beneficial since it has the ability to offer more information to researchers about the flow. CFD not only gives the overall values that experimentation offers, but gives a value at every node in the domain. If the overall values match, it can be assumed that all the detail described by the CFD solution is legitimate, giving researchers the ability to investigate small but important regions of the flow more closely.

1.3 CFD Advantages versus Disadvantages

The advantages of CFD techniques will probably be summarized in the following lines:

- A great time and cost reduction in new designs.
- There is a possibility to analyze different problem whose experiments are very difficult and dangerous.
- The CFD techniques offer the capacity of studying system under conditions over its limits. These conditions will probably be dangerous to experimental.
- The level of detail is practically unlimited. The experimental methods are more expensive with the increasing of measure point. However CFD techniques permits to generate several pieces of information without any cost. This offers the possibility to carry along a lot of parametric studies.
- The possibility to generate different graphs permits to understand the features of result.

Unfortunately, there are drawbacks to computational fluid dynamics as well .Its accuracy is still in many aspects insufficient.

- It can be difficult to model accurately in all situations with current numerical algorithms. Boundary layer transition and separation are two phenomena that can be particularly troublesome to predict with a high degree of accuracy.
- Many problems must be simplified to make them tractable. With some problems, computer resources may not be available to solve the problem to the level of accuracy originally desired. Examples of problem simplification include modeling a three-dimensional problem as a two-dimensional or axisymmetric problem, reducing the computational domain size or solution resolution of a given flow field, or modeling a time-varying problem as a steady-state problem.
- Certain assumptions must be made to obtain a solution. Usually these assumptions appear as boundary conditions and are relatively accurate – examples are asymptotic behavior at far-field boundaries or prescribed inlet or exit conditions.
- Particular solution algorithm might not produce a converged solution for a given flow field. In many cases, simply using intuition and applying specifically suited algorithms to the problem at hand can avoid this problem.

1.4 CFD in Ship Design Practice and Ship Hydrodynamics Analysis

The practical application of the Computational Fluid Dynamics (CFD), for predicting the flow pattern around ship hull has made much progress over the last decade. Today, several of the CFD tools play an important role in the ship hull form design. CFD has been used for analysis of ship resistance, sea-keeping, manoeuvering and investigating its variation when changing the ship hull form due to vary its parameters, which represents a very important task in the principal and final design stages. However, due to the existence of free surface and complex ship geometry, CFD has fallen behind its counterparts in other industrial fields. But with the recent breakthrough in ship CFD technology, practical applications of CFD in analyzing and predicting ship performance now become possible.

The solution of Drag measurement problems using Computational Fluid Dynamics (CFD) analysis is now becoming tractable through the accessibility of high performance computing. In ship hydrodynamics drag is also being named as “resistance”. Resistance characteristic of ship is one of the most important topics in Naval Architecture, Offshore and Ocean Engineering. Resistance of a moving ship occurs when the fluid force acting on the ship to oppose its motion, exerting pressure on the body of ship hull that may cause deformation in the ship structure and alter the flow of the fluid itself. In ship hydrodynamics where the accurate result is never possible and getting the resistance consequences of a ship hull form, optimization based on CFD solutions quantitative accuracy of integral results such as drag is imperative. When designing a ship, it is necessary to determine the total drag in order to obtain the maximum speed of ship and to determine what size of engine is required to reach a desired cruising speed as size of the engine will affect the weight of the ship and as well as the amount of fuel the ship consumes. This allows the designers to determine if the drag of the ship is an acceptable level from a financial standpoint as well as a physical standpoint. The financial perspective relates to the cost of the engine, and the fuel that the engine consumes in order to meet the ship’s mission requirements. Overall drag measurement is an important parameter that has been thoroughly studied by Naval Architects since this determines the power required to propel a ship. In preliminary stage, model test is expensive and time concise. CFD computation might be more practical which could provide more accurate and more reliable full-scale power prediction simulating the optimum result with effective cost and least amount of time.

When designing a ship, a scale model can be constructed and tested in a towing tank so that performance of the full scale ship can be determined by the scale model. William Froude developed the earliest technique to measure the resistance of a ship based on the testing of a model in a towing tank. This technique is not so easy to implement as the one used when a body is fully immersed in a fluid, for example, the case of an aircraft wing in a wing tunnel by Schwabacher (2000).

An alternative to the expensive experimental method is to use computer simulations based on methodologies of Computational Fluid Dynamics (CFD) to analyze the

flow field and predict drag for actual flow conditions. These methodologies are robust and can provide detailed information about the flow field. Advances in Computational methods and computer hardware allow efficient and accurate predictions for most flow conditions. Application of CFD methods to complex flows, however, needs to be examined carefully and validated with experimental data.

In our present work we will analyze drag coefficients of the hull of various model of ship. The hull is the main body of the ship below the main weather deck. The hull consists of an outside covering (or skin) and an inside framework to which the skin is secured. The economic recession, the environmental impact as well as the continuous fossil fuel consumption encourage actions that focuses on saving energy. In the vessels sector, one of the main objectives has always been to reach a hydro-dynamically optimum hull which will give the desired speed with minimum power. In such cases, it is necessary to analyze ship hull with free surface by using a numerical model with non-linear free surface conditions. The simulation of free surface flows around ship hulls, from an engineering standpoint, provides the ability to predict or calculate important parameters such as drag, lift etc. The drag, in particular, is very sensitive to free surface conditions.

1.5 Previous Research

Considering the importance of calculating drag co-efficient, an extensive research work has been carried out by naval architects, offshore and ocean engineers, hydro-dynamists and mathematicians. Both experimental and numerical investigations have been carried out to examine the characteristic of turbulent flow around different hull designs. The prediction of total drag experienced by an advancing ship is a complicated problem which requires a thorough understanding of the hydrodynamics forces acting on the ship hull, the physical process from which these forces arise and their mutual interaction. For instance, it is well established that an advancing ship generates a complex flow field which consists both the wave structure and the viscous boundary layer. These two features referred to as the wave resistance and the viscous resistance, respectively. It is the mutual interaction that renders the prediction

of the total drag of an advancing ship a challenging task, whether by experimental, analytical or computational methods.

Modern Computational Fluid Dynamics (CFD) computer codes which solve the Reynolds-Averaged Navier Stokes(RANS) equations for complex geometries have been used to simulate viscous flow around ship hulls since the early 1990s. The first significant simulations were confined to tanker and were relatively simple by today's standards; wave effects were absent, the free surface was considered as a plane of symmetry, and the most sophisticated turbulence model employed was the k-ϵ model. A summary of these early simulations can be found in the proceedings of the SSPA-CTH-IIHR workshop on Ship Viscous Flow held in Gothenburg, Sweden by Larsson *et al.* (1991).

As the speed and memory capacity of the computers increased and more sophisticated RANS codes were developed more realistic simulations were able to be performed. These advances are well documented in the proceedings of several international conferences on the application of CFD techniques to ship flows which have been held every few years since 1990, most notably those in Tokyo by Kodoma (1994), in Gothenburg by Larsson *et al.* (2003) and in Tokyo by Hino (2005). Significant information on the application of CFD codes to naval ships and submarines can also be found in another proceedings of the "Symposium on Naval Hydrodynamics", which is a biennial symposium sponsored by the US Office of Naval Research (ONR) and was first held in 1956.

Sangseon (1983) from the university of IOWA, performed a study of the viscous resistance for the Wigley Parabolic ship. In this study, the resistance for the fixed and free conditions as well as the viscous resistances are analyzed. Using Computational Fluid Dynamics tools the frictional resistance of a Trimaran ship has been studied by Gray (2007). Repetto (2001) computed drag co-efficient with free surface flows of ships like like Wigley and Series 60 model and other Floating vessels. The numerical study of Series 60 hull to improve the resistance characteristic has been investigated by Fonfach *et al.*(2010). Recently Fluent code simulation has been implemented around another type of naval hull named DTMB5415 by Jones *et al* (2010). In this

simulation wave profile for different find of mesh has been showed using Volume of Fluid (VOF) model. Drag estimates and their error estimation comparing with the experimental values in the presence on free surface flows have been simulated by Muscientes *et al*. (2010).For their wide range of applicability interface capturing methods are most frequently for free surface flows, but they can be computationally expensive. In this work, the volume of fluid (VOF) method implemented in a RANS solver was employed to simulate the free surface wave flow around Wigley parabolic and Series 60 hulls. VOF formulation implemented in FLUENT(ANSYS 2006)is slightly different from the original formulation of Hirt and Nichols(1981) and more general. Numerical breaking waves around a surface piercing NACA 0012 hydrofoil has been implemented by Ungureanu *et al.* (2011). Reynolds-averaged Navier-Stokes method has been implemented with the numerical solution of free-surface wave flows around surface-piercing cylindrical structures using an unstructured grid in the work of Rhee (2012).Numerical test were also performed by Rhee *et al.*(2005) who proposed a VOF-based technique to simulate the flow around the foil and the validations suggested that the most efficient solutions were found when the high resolution interface capturing(HRIC) schemes are employed.

Applications of computational fluid dynamics (CFD) to the maritime industry continue to grow as this advanced technology takes advantage of the increasing speed of computers. Numerical approaches have evolved to a level of accuracy which allows them to be used during the design process to predict ship resistance. Simulation of flows around hull forms is of considerable importance in marine hydrodynamics. This is mainly due to lack of reliable and sufficiently accurate experimental data. Generation of quality experimental data requires a large number of hull forms and experimental facilities. In the last two decades, different areas of incompressible flow modeling - including grid generation techniques, solution algorithms and turbulence modeling, and computer hardware capabilities have witnessed tremendous development. In view of these developments, computational fluid dynamics (CFD) can offer a cost-effective solution to many problems in underwater vehicle hull forms. However, effective utilization of CFD for marine hydrodynamics depends on proper selection of turbulence model, grid generation and boundary resolution. On the other hand grid generation and boundary layer resolution

depends on the kind of turbulence model that is used in a solution process. However, it can be said that the main issue is turbulence modeling and grid generation and boundary layer resolution are sub-issues.

Traditional methods to predict resistance on real hulls are based on towing tank models running at corresponding different Froude numbers in the region $0.2< Fr <0.5$ and then scaling results taking into account a friction line for the respective Reynolds numbers from $10^6 < Re < 10^8$.Advantages of these methods are the knowledge and experience acquired through the years that make results reasonably trustworthy. This has been one of the motivations of attempting to predict hull behaviors using computational tools, for this specific case, resistance. An alternative to the expensive experimental method is to use computer simulations based on methodologies of computational fluid dynamics (CFD) to analyze the flow field and predict drag for actual flow conditions which can be compared with other previous numerical results with Olivieri *et al.* (2001) and Azcueta (2005). These methodologies are robust and can provide detailed information about the flow field. Advances in computational methods and computer hardware allow efficient and accurate predictions for most flow conditions with Wanderely *et al.* (2011) as for Series 60 model.In order to obtain accurate results even in steady state simulations, Pranzitelli *et al.* (2011) included sufficient nodes within boundary layer correct mesh for high zones and suitable time step sizes.

In our present work, in the case of Wigley hull we have compared the computed result with other numerical results with Azcueta (2005), Mucientes (2010), Pranzitelli *et al*.(2011) and also with the experimental result Anon (1983).Similarly for the Series 60 hull the computed result has been compared with the numerical results like Azcueta (2005), Pranzitelli *et al*.(2011) and also with the experimental result Toda *et al.* (1992).

Many researchers used turbulence modeling to simulate flow around axisymmetric bodies since late nineteenth. The flow around under water or floating bodies was investigated and the force acting on it was calculated by a large number of researchers. The present research is influenced by the work of Versteeg and Malalasekera (1995), Banawan *et al.* (2006), Ozdemir *et al.* (2007), Izaguirre *et al* .

(2010),Saha G.K (2004), Mulvany *et al.* (2004), Rahman (2008),Jones *et al* .(2008) etc.

1.6 Research Objectives

The main objective of the present study is to calculate ship resistance and observe on the flow pattern around the hull using CFD (computational fluid Dynamics) simulation and investigating its variation when changing the ship hull form parameters using different CFD tools. The investigation is carried out to simulate incompressible flow around hull of two models namely Wigley Parabolic and Series 60. The major objectives of this study are:

- To compute the total drag using CFD tools in Wigley Parabolic and Series 60 at different turbulent models at different forward speed as well as various Froude numbers.
- To compute the drag co-efficient of ship
- To model the problem with appropriate boundary conditions creating mesh on it.
- To validate present numerical results with experimental and other reported numerical results.
- To observe the flow pattern around the ship hull.

CHAPTER 2

2. COMPUTATIONAL FLUID DYNAMICS MODELING CONSIDERATIONS

2.1 Discretization Methods in Computational Fluid Dynamics

Every computational fluid dynamics, in one form or another, is based on the governing equations of fluid dynamics: the continuity, energy, and momentum equations. These equations mathematically state three things, respectively; that mass is conserved, that energy is conserved, and that force equals mass times acceleration. In general, these governing equations can be written in two forms: the integral form and the partial differential equation form. Though the form of the equations results little difference with regard to hydrodynamic theory, different form leads to vastly different CFD solution algorithm. Since computers are unable to directly solve the governing equations of fluid motion, these equations must be transformed into forms that computers can handle; namely, the partial derivative (or integral) equations must be replaced with discrete numbers. In short, the computational domain is discretized so that the dependent variables are computed only at discrete points. Derivatives and integrals are approximated, which lead to an algebraic representation of the governing equations. In this way, a calculus problem is effectively transformed into an algebraic problem. There are four discretization schemes in CFD: (i) Finite Difference Method (FDM) (ii) Finite Element Method (FEM) (iii) Finite Volume Method (FVM) which are discussed elaborately by Versteeg & Malalasekera, (1995) and (iv) Boundary Element Method (BEM).

2.1.1 Finite Difference Method (FDM)

The FDM is the oldest of the methods, considered to have been developed by Euler in 1968, and is used to obtain numerical solution to differential equations by simple calculations. Tailor's series expansions are used to generate finite difference approximations to the derivatives of the RANS equations. The derivatives appearing in the governing equations are then replaced by these finite difference expressions, yielding an algebraic equation for the flow solution at each grid point. It is the simplest method to apply, but requires a high degree of regularity of the mesh.

2.1.2 Finite Element Method (FEM)

The FEM was developed initially as a procedure for constructing matrix solutions to stress and displacement calculations in structural analysis. The method uses simple piecewise polynomial functions on elements to describe the variations of the unknown flow variables. When these approximation functions are substituted into the governing equations it will not hold exactly, and the concept of a residual is introduced to measure the errors. Multiplying by a set of then minimizes these residuals weighting functions and then integrating. This result is a set of algebraic equations for the unknown terms of the approximating functions and hence the flow solutions can be found. Finite element method is not used extensively as it requires greater computational resources and CPU effort than equivalent finite volume method.

2.1.3 Finite Volume Method (FVM)

The FVM method discretises the integral form of the governing equations directly in physical space. The resulting statements express the exact conservation of relevant properties for each finite cell volume. Finite-difference type approximations are then substituted for the terms of the integrated equations, forming algebraic equations that are solved by an iterative method which will be discussed in Chapter 3. As this method works with the cell volumes and not the grid intersection points, both structured and unstructured meshes can be used. Flow variables can be stored either at Cell Centre or Cell Vertex locations. Conveniently, the cells coincide with the control volumes if using the Cell Centered scheme. For the cell vertex scheme, additional volumes are required to be constructed; however, the scheme has the advantage that boundary conditions are more easily applied since the variables are known on all boundaries.

2.1.4 Boundary Element Method (BEM)

The boundary element method (BEM) is a numerical computational method of solving linear partial differential equations, which have been formulated as integral equations. It can be applied in many areas of engineering and science including fluid mechanics and fracture mechanics. The integral equation may be regarded as an exact solution of the governing partial differential equation. The boundary element method attempts to use the given boundary conditions to fit boundary values into the integral equation, rather than values throughout the space defined by a partial differential equation. Once this is done, in the post-processing stage, the integral equation can then be used again to calculate numerically the solution directly at any desired point in the interior of the solution domain.BEM is applicable to problems for which Green's functions can be calculated. In BEM, there is no need to discretize the volume into meshes; unknowns at chosen points inside the solution domain are involved in the linear algebraic equations approximating the problem being considered.

2.2 Basics of Fluid Dynamics

In order to understand the results of this study, one must first understand the basics of fluid flow concepts including viscosity (μ), density (ρ), laminar and turbulent flow and also Reynolds and Froude number. Firstly, all fluids, whether they are liquids or gasses, have a certain density and viscosity. While the definition of density is widely understood as the weight of set volume of material, the definition of viscosity is much less widely known. Viscosity is a measure of a fluids resistance to flow. When a fluid is sheared (a force is applied), it begins to strain at a rate inversely proportional to the viscosity (Versteeg and Malalasekera, 1995). Accordingly, a high viscosity translates to a slower moving fluid.

2.2.1 Reynold's Number

The Reynolds number can be defined for a number of different situations where a fluid is in relative motion to a surface. Reynolds number is represented by the expression:

$$\mathrm{Re} = \frac{\rho V L}{\mu}$$

Where, V is the free stream flow velocity and L is the length value suited for the situation, typically the length of the hull of a ship. Reynolds number is a dimensionless value describing the viscous behavior of all Newtonian fluids. Because density (ρ), viscosity (μ) and L remain constant throughout the experiment, the Reynolds number is directly proportional to the free-stream velocity.

2.2.2 Froude Number

The Froude number is a dimensionless number defined as the ratio of a characteristic velocity to a gravitational wave velocity. It may equivalently be defined as the ratio of a body's inertia to gravitational forces. In fluid mechanics, the Froude number is used to determine the resistance of an object moving through water, and permits the comparison of objects of different sizes. Froude number is represented by the expression:

$$Fn = \frac{V}{\sqrt{gL}}$$

where V is the velocity of the ship, g is the acceleration due to gravity, and L is the length of the ship at the water line level.

2.3 Laminar and Turbulent Flow

In general, viscous flow over a surface can be characterized in two ways.

Laminar flow: If the path lines of the various fluid elements that make up the flow move smoothly and evenly, as shown in Figure 2.1 (a), the flow is called laminar. Laminar flow is orderly in nature and follows smooth streamlines. In laminar flow the fluid appears to move by the sliding of limitations of the infinitesimal thickness relative to adjacent layers.

Turbulent flow: If the movement of the fluid elements is rough and erratic, as shown in Figure 2.1 (b), the flow is called turbulent. Turbulence is a random phenomenon of flow disorder paradoxically due to the destabilizing effects of viscosity (Versteeg & Malalasekera, 1995).

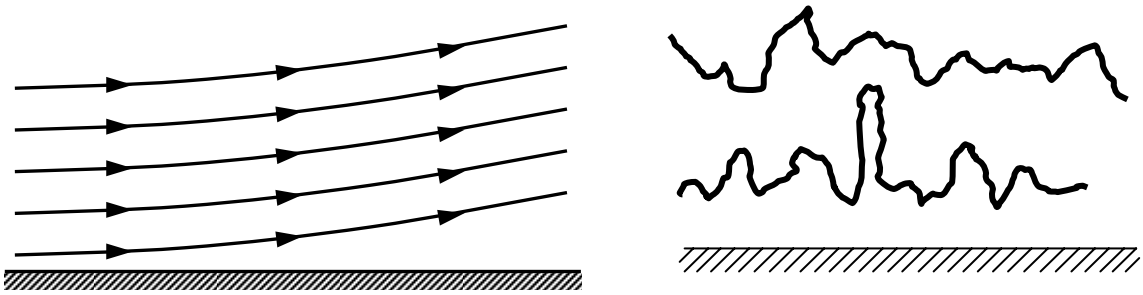

Figure 2.1: (a) Laminar and (b) Turbulent Path Line

Turbulent flow is characterized by fluctuation in velocity at all points of the flow field and these fluctuations with no definite frequency.

Due to the irregular motion of the fluid elements in a turbulent flow field, elements with higher kinetic energy from the outer regions of the flow are readily circulated close to the surface of the body. Thus, the average flow velocity near the body surface is larger for a turbulent flow than for a comparable laminar flow. This phenomenon is demonstrated in Figure 2.2, which shows the relative velocity profiles for laminar and turbulent flow.

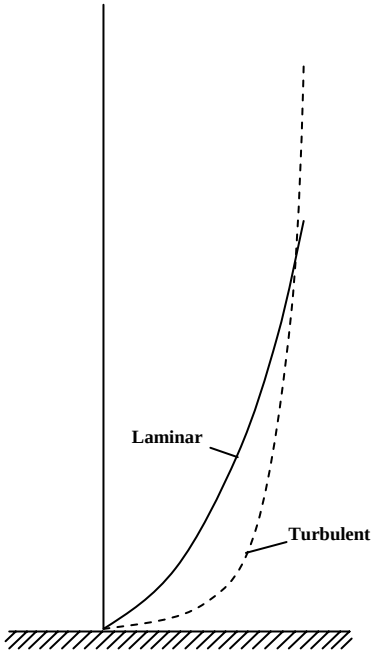

Figure 2.2: Laminar and Turbulent Velocity Profiles

Directly above the surface, the slope of the turbulent velocity profile is much greater than the laminar curve's slope. Since the shear stress (and skin friction force) on the body is directly proportional to the velocity gradient at the surface, it is clear that the skin friction drag is larger for the turbulent flow in comparison with the laminar flow. Reynolds number is used as a measure of when or where turbulent flow will occur.

When $\mathrm{Re} < 10^6$; the flow is laminar

$\mathrm{Re} \geq 10^{6;}$ the flow is turbulent.

2.4 Drag Forces

In fluid dynamics, drag (sometimes called resistance) refers to forces that oppose the relative motion of an object through a fluid. Drag forces act in a direction opposite to the oncoming flow velocity. When fluid flows over the hull of a ship then generally the ship is considered stationary. On the other hand, the ship moves through the fluid, while the fluid is more or less stationary. However, analyzing flow patterns past a moving body with stationary fluid is dynamically equivalent to analyzing the flow pattern around a stationary body as the flow moves. Drag of a moving ship occurs when the fluid force acting on the ship to oppose its motion, exerting pressure that may cause deformation in the structure and alter the flow of the fluid itself. In fluid dynamics, the drag equation is a practical formula used to calculate the force of drag experienced by an object due to movement through a fully enclosing fluid. The force on a moving object due to a fluid is:

$$F_D = \frac{1}{2}\rho V^2 C_D A \tag{2.1}$$

where

F_D is the force of drag, which is by definition the force component in the direction of the flow velocity,

ρ is the mass density of the fluid,

V is the velocity of the object relative to the fluid,

A is the wetted surface area and

C_D is the drag coefficient — a dimensionless constant related to the object's geometry and taking into account both viscous and wave making drag.

As a general rule, the wetted surface area is used as the frontal area for stream line bodies (e.g. pod, submarine).

2.4.1 Frictional and Viscous Drag

Frictional drag comes from friction between the fluid and the surfaces over which it is flowing. This friction is associated with the development of boundary layers, and it scales with Reynolds number. The viscous effects are a result of the friction between the fluid and the body and are generated in the boundary layer. The viscous resistance is defined as the component associated with the expenditure of energy in generating vorticity and turbulence.

Frictional drag , $R_F = C_f\left(\frac{1}{2}\rho V^2 A\right)$

and Viscous drag , $C_V = \frac{R_F}{\frac{1}{2}\rho V^2 S}$ (2.1)

where k is the form factor.

2.4.2 Residuary and Wave Making Drag

Wave-making and eddy-making drag components are often lumped into a single “residuary drag,” especially when drag measurements are extrapolated from model testing. Wave making is usually by far the larger component of residuary drag; it is therefore given more attention in research and in the designing of a hull.The residuary drag, RW can be further broken down into numerous individual components of drag, with the main component being the wave making drag.. Wave making resistance C_W is defined as the resistance due to the loss of energy to the formation of waves.

$C_W = \frac{R_W}{\frac{1}{2}\rho V^2 S}$ (2.3)

2.5 Grid Generation

Analytical solutions of fluid dynamics problems involve closed-form mathematical expressions that describe the variation of the dependent variables continuously throughout the flow domain. However, numerical solvers cannot generate closed-form analytical expressions, but it can calculate values of the dependent variables only at discrete points in the domain. These points are called grid points, or nodes. In order for a computational fluid dynamics code to provide a complete flow field description for a particular problem, the user must specify a grid that tells the flow solver at what locations in the problem domain the solution is to be computed. The specifications of the grid construction can have a major influence on the fidelity of the solution and can, in fact, determine whether a solution is even attainable.

Grid generation is often considered as the most important and most time consuming part of CFD simulation. The quality of the grid plays a direct role on the quality of the analysis, regardless of the flow solver used. Additionally, the solver will be more robust and efficient when using a well constructed mesh.

2.5.1 Solution Dependence on Grid

The quality and efficiency of the numerical solution is highly dependent on the construction of the grid used in the computational model. Several factors must be considered when generating a grid to ensure that the best possible numerical results are obtained with a particular solution algorithm. Grid point placement can have a substantial effect on the stability and convergence of the numerical solver. For example, if grid points are not adequately concentrated in regions of high flow parameter gradients (such as near shock waves, in boundary layer separation regions, or near stagnation points), the numerical solver may not be able to adequately resolve these gradients in the flow field. Because obtaining the solution numerically is an iterative process, it is possible, and quite likely, that an insufficiently fine mesh will preclude the adequate calculation of important flow features, leading to oscillations in computed parameters or even divergence of the solution.

In numerical grid construction, there is an important trade-off between mesh density, solution efficiency, and solution accuracy. Generally, the more grid points contained in

a given grid, the more accurate the final, converged solution will be. However, the density of the grid cannot be arbitrarily increased without bound. Computer processor speed and memory limitations often dictate how fine a mesh can realistically be. Increasing the density of a mesh too much can quickly cause a given problem to become intractable. Along these same lines, it is important for the CFD analyst to carefully concentrate grid points in high-gradient regions while keeping the grid density throughout the majority of the computational domain fine enough for accuracy yet sparse enough for speed. Clearly, the maximum allowable grid point density of a particular simulation is highly dependent on the speed and capabilities of the computer platform being used.

2.5.2 Structured Grids

Structured grid methods take their name from the fact that the grid is laid out in a regular repeating pattern called a block. These types of grids utilize quadrilateral elements in 2D and hexahedral elements in 3D in a computationally rectangular array. Although the element topology is fixed, the grid can be shaped to be body fitted through stretching and twisting of the block. Really good structured grid generators utilize sophisticated elliptic equations to automatically optimize the shape of the mesh for orthogonality and uniformity.

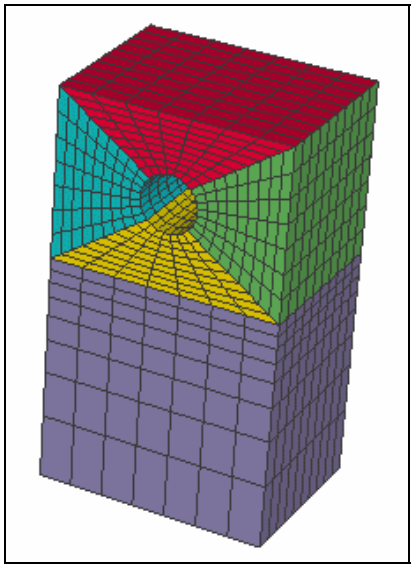

Figure 2.3: Structured Multiblock Mesh Using Point to Point

Structured grids enjoy a considerable advantage over other grid methods in that they allow the user a high degree of control. Because the user places control points and edges interactively, it has total freedom when positioning the mesh. In addition, hexahedral and quadrilateral elements, which are very efficient at filling space, support a high amount of skewness and stretching before the solution will be significantly affected. This allows the user to naturally condense points in regions of high gradients in the flow field and expand out to a less dense packing away from these areas. Also, because the user interactively lays out the elements, the grid is most often flow-aligned, thereby yielding greater accuracy within the solver. Structured block flow solvers typically require the lowest amount of memory for a given mesh size and execute faster because they are optimized for the structured layout of the grid. Lastly, post processing of the results on a structured block grid is typically a much easier task because the logical grid planes make excellent reference points for examining the flow field and plotting the results.

The major drawback of structured block grids is the time and expertise required to lay out an optimal block structure for an entire model. Often this comes down to past user experience and force placement of control points and edges. Some geometries, e.g. shallow cones and wedges, do not lend themselves to structured block topologies. In these areas, the user is forced to stretch or twist the elements to a degree which drastically affects solver accuracy and performance. Grid generation times are usually measured in days if not weeks.

2.5.3 Unstructured Grids

Unstructured grid methods utilize an arbitrary collection of elements to fill the domain. Because the arrangement of elements has no discernible pattern, the mesh is called unstructured. These types of grids typically utilize triangles in 2D and tetrahedral in 3D. While there are some codes which can generate unstructured quadrilateral elements in 2D, there are currently no production codes which can generate unstructured hexahedral elements in 3D.

It is interesting to note that discretization of a domain can be accomplished either directly in the physical space or in the transformed computational space; the choice depends mainly on the numerical solution method and the domain of the solution. For

those solution schemes where the governing fluid dynamics equations are integrated numerically on the physical domain and solved, the corresponding grid system is usually generated directly in the physical domain. In such cases, the domain of solution is divided into individual cells (usually triangles or quadrilaterals in 2D or pyramids or tetrahedrons in 3D) and for these cases, the grid points generally cannot be associated with grid lines. Instead locations of points must be individually specified.

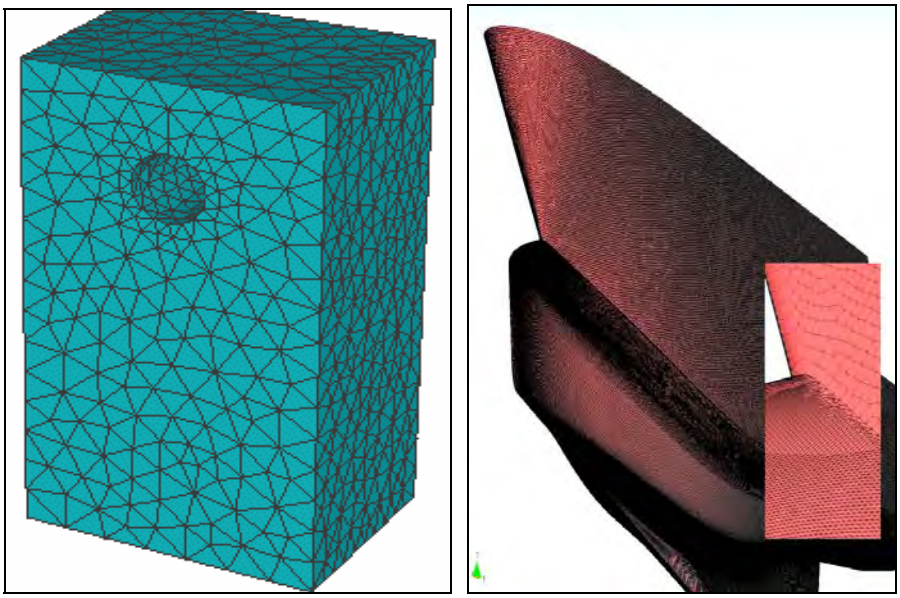

Figure 2.4: Unstructured Mesh Consisting of Triangles and Tetrahedral Elements

The advantage of unstructured grid methods is that they are much automated and, therefore, require little user time or effort. The user need not worry about laying out block structure or connections. Additionally, unstructured grid methods are well suited to inexperienced users because they require little user input and will generate a valid mesh under most circumstances. Unstructured methods also enable the solution of very large and detailed problems in a relatively short period of time. Grid generation times are usually measured in minutes or hours.

The major drawback of unstructured grids is the lack of user control when laying out the mesh. Typically any user involvement is limited to the boundaries of the mesh with the mesher automatically filling the interior. Triangle and tetrahedral elements have the problem that they do not stretch or twist well, therefore, the grid is limited to being

largely isotropic, i.e. all the elements have roughly the same size and shape. This is a major problem when trying to refine the grid in a local area, often the entire grid must be made much finer in order to get the point densities required locally.

2.5.4 Hybrid Grids

Hybrid grid methods are designed to take advantage of the positive aspects of both structured and unstructured grids. Hybrid grids utilize some form of structured grid in local regions while using unstructured grid in the bulk of the domain.

Hybrid grids can contain hexahedral, tetrahedral, prismatic, and pyramid elements in 3D and triangles and quadrilaterals in 2D. The various elements are used according to their strengths and weaknesses. Hexahedral elements are excellent near solid boundaries (where flow field gradients are high) and afford the user a high degree of control, but are time consuming to generate. Prismatic elements (usually triangles extruded into wedges) are useful for resolving near wall gradients. In almost all cases, tetrahedral elements are used to fill the remaining volume.

Another type of hybrid grid is the quasi-structured or "cooper" grid method. While basically a form of the prismatic grid extrusion technique, the quasi-structured method does allow for some sophisticated forms of growing the 3D mesh using a sweeping concept within a CAD solid model.

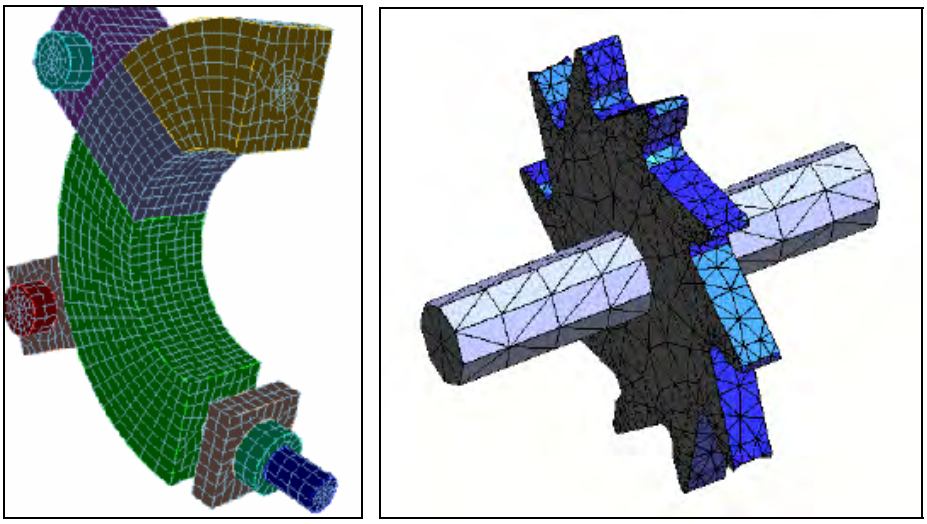

Figure2.5: Quasi Structured Prismatic Mesh

The advantage of hybrid grid methods it can be utilized the positive properties of structured grid elements in the regions which need them the most and use automated unstructured grid techniques where not much is happening in the flow field. The ability to control the shape and distribution of the grid locally is a powerful tool which can yield excellent meshes.

The disadvantage of hybrid methods is that they can be difficult to use and require user expertise in laying out the various structured grid locations and properties to get the best results. Hybrid methods are typically less robust than unstructured methods. The generation of the structured portions of the mesh will often fail due to complex geometry or user input errors. While the flow solver will use more resources than a structured block code, it should be very similar to an unstructured code. Post processing the flow field solution on a hybrid grid suffers from the same disadvantages as an unstructured grid. The time required for grid generation is usually measured in hours or days.

2.6 Computational Fluid Dynamics Solver

Today There is a great variety of CFD codes, from free codes to powerful commercial CFD codes. We can join these codes in some groups:

General Codes: Into these types we can find the codes that have the following tools at the service of the user to: to generate geometries, to apply boundary conditions, to discretise the spatial domain (generally this step is called mesh generating), solve the problem and show the results. Examples of these are: CFX, Fluent, Phoenix, Open FOAM etc.

When the fluid flow problems are numerically solved, the surfaces, BC and spaces around the boundaries of the computational domain are discretized to be used in Computational Fluid Dynamics (CFD) code. Typical CFD software contains three main modules: the preprocessor, the solver and the post-processor.

Pre-processor: In the pre-processor are included all variables that define the problem setup. In the region of fluid to be analysed it must be defined the properties of the fluid

acting on the domain, including external constraints or boundary conditions, such as pressure and velocity to implement realistic situations.

Solver: Here the solution to a CFD problem is computed. The governing equations are solved iteratively to compute the flow parameters of the fluid as the time lapses. Convergence is important to produce an accurate solution of the partial differential equations.

Post-processor: This module is used to process and visualize the results obtained from the solver. To obtain an approximate solution of the governing equations, a discretized method is used, which approximates the original differential equations with a system of algebraic equations, solved by the CFD software. Discretization in space and time must be defined. The accuracy of numerical solutions depends on the quality of the discretization used.

Spatial discretization divides the computational domain into small sub-domains where the mesh is generated. The fluid flow is described mathematically by specifying its velocity at all points in space and time. Meshes in CFD comprise nodes at which flow parameters are resolved.

2.7 The Fluent Code

Fluent is a computational fluid dynamics commercial computer code developed and marketed by Fluent Inc. and Ansis. The code solves the equations for conservation of mass, momentum, energy and other relevant fluid variables using a cell-centered finite volume method. First the fluid domain is divided into a large number of discrete control volumes(also known as cells) using a pre-processor code which creates a computational mesh on which the equations can be solved. The meshing software available with Fluent is called Gambit. This software allows the use of several types of computational cells including triangular, quadrilateral, hexahedral, tetrahedral, pyramidal, prismatic and hybrid meshes.

Once the fluid domain has been meshed, the governing equations (in integral form) are applied to each discrete control volume and used to construct a set of non-linear algebraic equations for the discrete dependent variables. Fluent then offers the user a

number of choices for the algorithm used to solve these equations, including coupled explicit, coupled implicit and segregated solvers. In all the calculations reported here only the coupled implicit has been used. In this approach the governing equations are solved sequentially. Since these equations are non-linear they are first linearised using an implicit method. This produces a scalar system of equations containing only one equation per computational cell per degree of freedom. An implicit (Gauss-Siedel) linear equation solver is then used in conjunction with an algebraic multigrid(AMG) method to solve the resultant scalar system of equations for the dependent variable in each cell. Since the equations are non-linear several iterations of the solution loop must be performed before a converged solution is obtained.

CHAPTER 3

3. THEORETICAL BACKGROUND

With the progress of computational fluid dynamics (CFD), it is now being used more often as a performance prediction tool for hull design. In particular, combining computation codes capable of accurately interpreting free surfaces and the multi-block grid technique has enabled highly accurate estimations of the drag co-efficient of various hull designs in free surface flow. Most CFD programs used for engineering applications provide a solution of the Reynolds averaged Navier-Stokes equations (RANS) .The solution obtained is thus a stationary, time-averaged representation of the flow and provides vast information on the turbulence characteristics.

3.1 Mathematical Formulations

We consider three dimensional moving bodies at a constant velocity $\vec{U}$ at the surface of a fluid of finite depth. The sketch of the body and free surface is depicted in Fig 3.1.The fluid is assumed to be inviscid and incompressible and the flow to be irrotational. We choose a cartesian frame of reference moving bodies and assume that the flow is steady. The cartesian coordinates (x, y, z) are chosen with the positive z-axis directed vertically upwards where the origin at the aft perpendicular to the hull form, the x-axis in the opposite flow direction of the velocity $\vec{U}$ and positive y in portside.

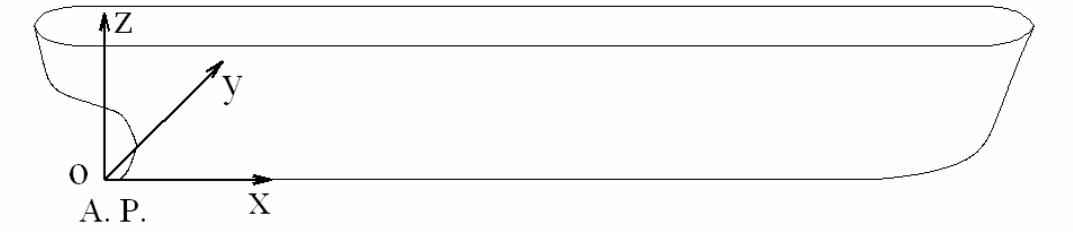

Figure 3.1: Three Dimensional Co-ordinate Systems for a Hull Design

3.1.1 Governing Equations

The conservative or divergence form of the system of equations, which governs the steady state three dimensional flow of an incompressible Newtonian fluid is [Versteeg and Malalasekera, 1995]:

Mass/continuity: $\text{div}(\vec{u}) = 0$ (3.1)

$$x\text{-momentum}: \text{div}(\rho u \vec{u}) = -\frac{\partial P}{\partial x} + \text{div}\left(\mu \text{ grad } u\right) + S_x \quad (3.2)$$

$$y\text{-momentum}: \text{div}(\rho u \vec{v}) = -\frac{\partial P}{\partial y} + \text{div}\left(\mu \text{ grad } v\right) + S_y \quad (3.3)$$

$$z\text{-momentum}: \text{div}(\rho u \vec{w}) = -\frac{\partial P}{\partial z} + \text{div}\left(\mu \text{ grad } w\right) + S_z \quad (3.4)$$

Where, ρ = density, p = pressure, t = time, $\vec{u} = ui + vj + wk$ = velocity vector, μ = viscosity, and S_x, S_y *and* S_y = source term. The above equations are known as conservation equations as these equations obey the conservation principles of mass, momentum and energy. It is clear that there are significant commonalities among above the various equations. So these equations can be written in a general form and that general equation can be solved numerically instead of solving each equation individually. By introducing a general variable φ the conservative form of all fluid flow equations can be written as:

$$div\left(\rho\phi\vec{u}\right) = div\left(\Gamma grad\,\phi\right) + S_\phi \quad (3.5)$$

In words

Rate of flow of		Rate of increase		Rate of increase
ϕ of fluid element	=	of ϕ due to diffusion	+	of ϕ due to source
(Convective term)		(Diffusive term)		(Source term)

Equation (3.5) is the so-called transport equation for property φ. In order to bring out the common features we have, of course, had to hide the terms that are not shared between the equations in the source terms. By setting φ equal to 1, u, v, w and selecting appropriate values for the diffusive coefficient Γ and source term we may obtain

Equations (3.1) to (3.4). Equation (3.5) is used as the starting point for computational procedures in the finite volume method.

3.2 Solution using Finite Volume Method

The Finite Volume Method (FVM) offers an alternative approach for deriving the discretized equations. This method is based on the principle that the divergence term, that frequently occurs in differential equations governing various interesting scientific phenomena, can be rewritten as a surface integral using the divergence theorem. The problem then simplifies to evaluating fluxes normal to the cell walls. Since this becomes a vector problem, the cell walls can take any shape and can be arbitrarily oriented. All that is required is that they enclose a closed volume. And since the method is based on evaluating fluxes, the Finite Volume Method is conservative. Outflow from one cell becomes inflow into another. This makes the FVM stable and flexible, and yet relatively easy to implement. This is why the Finite Volume Method is commonly implemented in commercial computational fluid dynamics (CFD) solvers.

As we have seen, all differential equations are conservation equations for mass, momentum, energy so it is necessary that all discretized equations also obey the conservation principle. Finite volume method is inherently conservative method because the flux going out through a face of one control-volume is exactly equal to the flux coming into the adjacent control-volume through the same face. Including discretization following steps are involved in finite volume method:

i. Divide the domain into finite control volumes.

ii. Integrate the differential equations over each control volume.

iii. Approximation of volume and surface integrals.

iv. Discretization and interpolation using UDS or CDS.

3.3 Integration of the Transport Equation

The key step of finite volume method is the integration of the transport Equation (3.5) over each control volume yielding

$$\int_{CV} div(\rho\phi\vec{u})dv = \int_{CV} div\left(\Gamma grad\phi\right)dv + \int_{CV} S_\phi dv \tag{3.6}$$

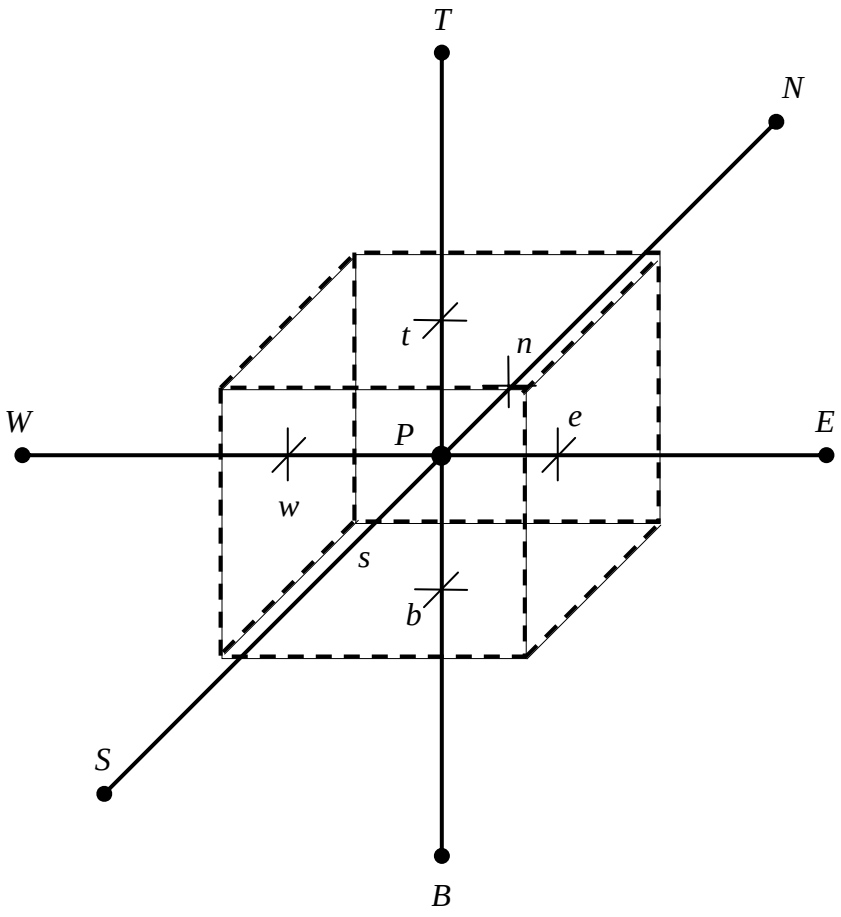

Figure 3.2: A Cell in Three Dimensions with Its Neighbouring Points and Faces.

The volume integrals in the first term on the left hand side, the convective term, and in the first term on the right hand side, the diffusive term, are re-written as integrals over the entire bounding surface of the control volume by using Gauss' divergence theorem. For a vector $\vec{a}$ this theorem states

$$\int_{CV} div\ \vec{a}\ dv = \int_{A} \vec{n}\ .\vec{a}\ dA$$

Where $\vec{n}$ is the vector normal to surface element *dA*.

Applying Gauss' divergence theorem, Equation (3.6) can be written as

$$\int_A \vec{n}.\left(\rho\phi\vec{u}\right)dA = \int_A \vec{n}.\left(\Gamma grad\phi\right)dA + \int_{CV} S_\phi dv \tag{3.7}$$

Here we are solving this problem in three dimensions that is, in x-y-z plane, so it can be written as

$$\rho\left[\int_e (u\phi)\,dx - \int_w (u\phi)\,dx + \int_n (v\phi)\,dy - \int_s (v\phi)\,dy + \int_t (w\phi)\,dz - \int_b (w\phi)\,dz\right] =$$
$$\int_e \left(\Gamma\frac{\partial\phi}{\partial x}\right)dx - \int_w \left(\Gamma\frac{\partial\phi}{\partial x}\right)dx + \int_n \left(\Gamma\frac{\partial\phi}{\partial y}\right)dy - \int_s \left(\Gamma\frac{\partial\phi}{\partial y}\right)dy + \int_t \left(\Gamma\frac{\partial\phi}{\partial z}\right)dz \qquad (3.8)$$
$$-\int_b \left(\Gamma\frac{\partial\phi}{\partial z}\right)dz + \int_{CV} S_\phi\,dxdydz$$

Here, the term $\rho u\varphi$ is the convective flux and $\Gamma grad\varphi$ is the diffusive flux.

3.4 Approximation of Integrals

The next step is to approximate the flux integrals which are done by two levels of approximation. Consider, f_i = the flux in the *i*th direction. In first level the integral is approximated in terms of the variable values at one or more location on the cell face. The simplest way is the midpoint rule flux, where f_i is approximated as the value at the centre of CV face. The midpoint rule is a second order approximation, so in order to preserve the second order accuracy the interpolation should also be of second order. On the east face of control-volume, the midpoint rule applied as:

$$\int_e f_i \Delta y = f_e \Delta y$$

Source term approximation is done by applying the centre value of the source as representative value for the whole CV. Thus, Equation (3.8) becomes

$$\rho\left[(u\phi)_e \Delta x - (u\phi)_w \Delta x + (v\phi)_n \Delta y - (v\phi)_s \Delta y + (w\phi)_t \Delta z - (w\phi)_b \Delta z\right]$$
$$= \left(\Gamma\frac{\partial\phi}{\partial x}\right)_e \Delta x - \left(\Gamma\frac{\partial\phi}{\partial x}\right)_w \Delta x + \left(\Gamma\frac{\partial\phi}{\partial y}\right)_n \Delta y - \left(\Gamma\frac{\partial\phi}{\partial y}\right)_s \Delta y + \left(\Gamma\frac{\partial\phi}{\partial z}\right)_t \Delta z \qquad (3.9a)$$
$$-\left(\Gamma\frac{\partial\phi}{\partial z}\right)_b \Delta z + \bar{S}\Delta x\Delta y\Delta z$$

This can also be written as

$$\rho\left[u_e\phi_e\Delta x - u_w\phi_w\Delta x + v_n\phi_n\Delta y - v_s\phi_s\Delta y + w_t\phi_t\Delta z - w_b\phi_b\Delta z\right] =$$
$$\Gamma_e\left(\frac{\partial\phi}{\partial x}\right)_e \Delta x - \Gamma_w\left(\frac{\partial\phi}{\partial x}\right)_w \Delta x + \Gamma_n\left(\frac{\partial\phi}{\partial y}\right)_n \Delta y - \Gamma_s\left(\frac{\partial\phi}{\partial y}\right)_s \Delta y \qquad (3.9b)$$
$$+\Gamma_t\left(\frac{\partial\phi}{\partial z}\right)_t \Delta z - \Gamma_b\left(\frac{\partial\phi}{\partial z}\right)_b \Delta z + \bar{S}\Delta x\Delta y\Delta z$$

To simplify the above equation, F_i, denotes the convective flux that is,

$$F_i = \rho\, u_i \Delta x$$

Equation (3.9b) now be simplified to

$$\begin{aligned} & F_e\phi_e - F_w\phi_w + F_n\phi_n - F_s\phi_s + F_t\phi_t - F_b\phi_b \\ & = \Gamma_e\left(\frac{\partial\phi}{\partial x}\right)_e \Delta x - \Gamma_w\left(\frac{\partial\phi}{\partial x}\right)_w \Delta x + \Gamma_n\left(\frac{\partial\phi}{\partial y}\right)_n \Delta y \\ & -\Gamma_s\left(\frac{\partial\phi}{\partial y}\right)_s \Delta y + \Gamma_t\left(\frac{\partial\phi}{\partial z}\right)_t \Delta z - \Gamma_b\left(\frac{\partial\phi}{\partial z}\right)_b \Delta z + \bar{S}\Delta x\Delta y\Delta z \end{aligned} \tag{3.9c}$$

3.5 Interpolation

After the approximation of the integrals we obtain Equation (3.11) involving the values of fluxes at each CV face, with φ as unknown. Since we want to calculate the variable at each grid point, it is required to write φ at face location in terms of their values at the grid points. Thus, we have to interpolate φ between grid points. There are many schemes available for approximation. Two basic schemes are the Central Differencing Scheme (CDS) or Linear Interpolation, and Upwind Differencing Scheme (UDS). Diffusive term is generally discretized using CDS approximation whereas convection term can be discretized by any scheme depending on the strength of the convection (Versteeg and Malalasekera, 1995).

In the present study, the convective term is discretized by upwind differencing scheme. In the upwind method the variation of φ between two grid points is approximated by a zeroth order polynomial, i.e., a constant value from the grid node in upstream direction. As for example for a flow in positive x direction we take ϕ_e is equal to the value of φ in upstream direction which is ϕ_p.

$$\begin{aligned} \phi_e &= \begin{cases} \phi_P & if \quad F_e>0 \\ \phi_e & if \quad F_e<0 \end{cases} & \phi_w &= \begin{cases} \phi_W & if \quad F_w>0 \\ \phi_P & if \quad F_w<0 \end{cases} \\ \phi_n &= \begin{cases} \phi_P & if \quad F_n>0 \\ \phi_N & if \quad F_n<0 \end{cases} & \phi_s &= \begin{cases} \phi_S & if \quad F_s>0 \\ \phi_P & if \quad F_s<0 \end{cases} \\ \phi_n &= \begin{cases} \phi_P & if \quad F_t>0 \\ \phi_T & if \quad F_t<0 \end{cases} & \phi_s &= \begin{cases} \phi_B & if \quad F_b>0 \\ \phi_P & if \quad F_b<0 \end{cases} \end{aligned} \tag{3.9d}$$

Flux approximation for F

$$F_e\phi_e = \max(F_e,0)\phi_P + \min(F_e,0)\phi_E$$
$$F_w\phi_w = \max(F_w,0)\phi_W + \min(F_w,0)\phi_P$$
$$F_n\phi_n = \max(F_n,0)\phi_P + \min(F_n,0)\phi_N \qquad (3.9e)$$
$$F_s\phi_s = \max(F_s,0)\phi_S + \min(F_s,0)\phi_P$$
$$F_t\phi_t = \max(F_t,0)\phi_P + \min(F_t,0)\phi_T$$
$$F_b\phi_b = \max(F_b,0)\phi_B + \min(F_b,0)\phi_P$$

Equations (3.9d) and (3.9e) are identical, both of them give the same information, but for generalization equation (3.9e) is used here. For implementation into the computer code, the expressions in equation (3.9e) are applied.

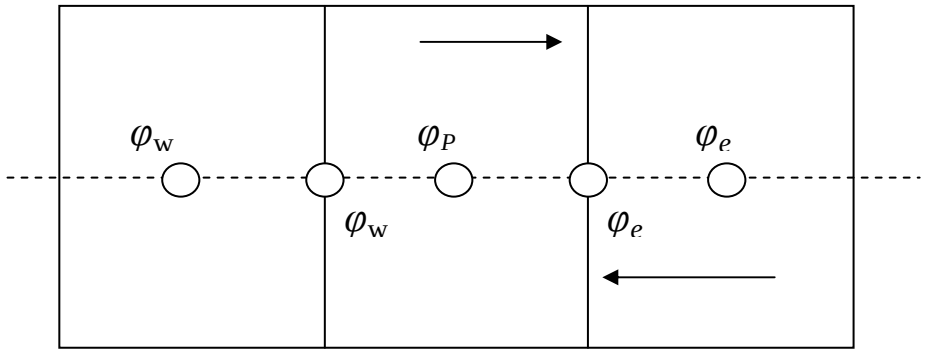

Figure 3.3: The Upwind Difference Scheme for One Dimensional Flow

Like the convective flux, the diffusive flux integral is approximated by midpoint rule. The derivatives of φ are generally approximated by the CDS as follows:

$$\left(\frac{\partial\phi}{\partial x}\right)_e = \frac{\phi_E - \phi_P}{x_E - x_P} \qquad \left(\frac{\partial\phi}{\partial x}\right)_w = \frac{\phi_P - \phi_W}{x_P - x_W}$$

$$\left(\frac{\partial\phi}{\partial y}\right)_n = \frac{\phi_N - \phi_P}{y_N - y_P} \qquad \left(\frac{\partial\phi}{\partial y}\right)_s = \frac{\phi_P - \phi_S}{y_P - y_S} \qquad (3.9f)$$

$$\left(\frac{\partial\phi}{\partial z}\right)_t = \frac{\phi_T - \phi_P}{z_T - z_P} \qquad \left(\frac{\partial\phi}{\partial z}\right)_b = \frac{\phi_P - \phi_B}{z_P - z_B}$$

3.6 Finite Volume Method for Three-Dimensional Diffusion Problems

Steady state diffusion in a three –dimensional situation is governed by

$$\frac{\partial}{\partial x}\left(\Gamma\frac{\partial\phi}{\partial x}\right)+\frac{\partial}{\partial y}\left(\Gamma\frac{\partial\phi}{\partial y}\right)+\frac{\partial}{\partial z}\left(\Gamma\frac{\partial\phi}{\partial z}\right)+S=0 \tag{3.10}$$

Now a three-dimensional grid is used to subdivide the domain. A typical control volume is shown in Figure 3.2:

A cell containing node *P* now has six neighboring nodes identified as west, east, south, north, bottom and top nodes (*W*, *E*, *S*, *N*, *B*, and *T*). As before, the notation, *w*, *e*, *s*, *n*, *b* and *t* are used to refer to the west, east, south, north, bottom and top cell faces respectively. Integration of equation (3.10) over the control volume shown gives

$$\begin{aligned}&\left[\Gamma_e A_e\left(\frac{\partial\phi}{\partial x}\right)_e-\Gamma_w A_w\left(\frac{\partial\phi}{\partial x}\right)_w\right]+\left[\Gamma_n A_n\left(\frac{\partial\phi}{\partial y}\right)_n-\Gamma_s A_s\left(\frac{\partial\phi}{\partial y}\right)_s\right]\\&+\left[\Gamma_t A_t\left(\frac{\partial\phi}{\partial z}\right)_t-\Gamma_b A_b\left(\frac{\partial\phi}{\partial z}\right)_b\right]+\bar{S}\Delta V=0\end{aligned} \tag{3.11}$$

The above equation represents the balance of the generation of ϕ in a control volume and the fluxes through its cell faces.

The diffusive flux terms are evaluated as

Flux across the east face, $\Gamma_e A_e\left(\frac{\partial\phi}{\partial x}\right)_e=\Gamma_e A_e\left(\frac{\phi_E-\phi_P}{\delta x_{PE}}\right)$

Flux across the west face, $\Gamma_w A_w\left(\frac{\partial\phi}{\partial x}\right)_w=\Gamma_w A_w\left(\frac{\phi_P-\phi_W}{\delta x_{WP}}\right)$,

Flux across the north face, $\Gamma_n A_n\left(\frac{\partial\phi}{\partial y}\right)_n=\Gamma_n A_n\left(\frac{\phi_N-\phi_P}{\delta y_{PN}}\right)$,

Flux across the south face, $\Gamma_s A_s\left(\frac{\partial\phi}{\partial y}\right)_s=\Gamma_s A_s\left(\frac{\phi_P-\phi_S}{\delta y_{SP}}\right)$,

Flux across the top face, $\Gamma_t A_t \left(\frac{\partial \phi}{\partial z}\right)_t = \Gamma_t A_t \left(\frac{\phi_T - \phi_P}{\delta z_{PT}}\right)$,

Flux across the bottom face, $\Gamma_b A_b \left(\frac{\partial \phi}{\partial y}\right)_b = \Gamma_b A_b \left(\frac{\phi_P - \phi_B}{\delta y_{BP}}\right)$

Following the above procedures the discretised form of the equation (3.11) is obtained

$$\left[\Gamma_e \frac{(\phi_E - \phi_P)A_e}{\delta x_{PE}} - \Gamma_w \frac{(\phi_P - \phi_W)A_w}{\delta x_{WP}}\right] + \left[\Gamma_n \frac{(\phi_N - \phi_P)A_n}{\delta y_{PN}} - \Gamma_s \frac{(\phi_P - \phi_S)A_s}{\delta y_{SP}}\right]$$

$$+ \left[\Gamma_t \frac{(\phi_T - \phi_P)A_t}{\delta z_{PT}} - \Gamma_b \frac{(\phi_P - \phi_B)A_b}{\delta z_{BP}}\right] + S_u + S_P \phi_P = 0 \qquad (3.12)$$

As before this can be arranged as to give the discretised equation for interior nodes:

$$a_P \phi_P = a_W \phi_W + a_E \phi_E + a_S \phi_S + a_N \phi_N + a_B \phi_B + a_T \phi_T + S_u \qquad (3.13)$$

where

a_W	a_E	a_S	a_N	a_B	a_T	a_P
$\frac{\Gamma_w A_w}{\delta x_{WP}}$	$\frac{\Gamma_e A_e}{\delta x_{PE}}$	$\frac{\Gamma_s A_s}{\delta y_{SP}}$	$\frac{\Gamma_n A_n}{\delta y_{PN}}$	$\frac{\Gamma_b A_b}{\delta z_{BP}}$	$\frac{\Gamma_t A_t}{\delta z_{PT}}$	$a_W + a_E + a_S + a_N + a_B + a_T - S_P$

The discretised equations for three dimensional diffusion problems take the following general form;

$$a_P \phi_P = \sum a_{nb} \phi_{nb} + S_u$$

3.7 Linear Equation System

It may be possible that sometimes source term is a non-linear function of unknown φ to improve convergence it can be linearized as:

$$\bar{S} \Delta x \Delta y \Delta z = S_u + S_P \phi_P$$

Where, S_u = constant term, S_P = function of φ.

Using the above schemes for the diffusive and convective fluxes and source term linearization the discretization Equation (3.9c) can be rearranged to:

$$a_P\phi_P = a_W\phi_W + a_E\phi_E + a_S\phi_S + a_N\phi_N + a_B\phi_B + a_T\phi_T + b \tag{3.14}$$

where, $a_E = -\min\left(F_e, 0\right) + \dfrac{\Gamma_e \Delta x}{x_E - x_P}$

$$a_W = \max\left(F_w, 0\right) + \frac{\Gamma_w \Delta x}{x_P - x_W}$$

$$a_N = -\min\left(F_n, 0\right) + \frac{\Gamma_n \Delta y}{y_N - y_P} \tag{3.15}$$

$$a_S = \max\left(F_s, 0\right) + \frac{\Gamma_s \Delta y}{y_P - y_S}$$

$$a_T = -\min\left(F_t, 0\right) + \frac{\Gamma_t \Delta z}{z_T - z_P}$$

$$a_B = \max\left(F_b, 0\right) + \frac{\Gamma_b \Delta z}{z_P - z_B}$$

$$a_P = a_E + a_W + a_N + a_S + a_T + a_B$$

$$b = S_u$$

Equation (3.15) can be written in the general form:

$$a_P\phi_P = \sum a_{nb}\phi_{nb} + b \tag{3.16}$$

Here, ‘nb’ represents neighbouring points.

Discretized equation of the form (3.16) must be set up at each of the nodal points in order to solve a problem. For control volumes that are adjacent to the domain boundaries the general discretized Equation (3.16) is modified to incorporate boundary conditions. The resulting system of linear algebraic equations is then solved to obtain the distribution of the property at nodal points which can be solved by applying several algebraic solvers using boundary conditions

i) Gauss elimination,

ii)LU decomposition,

iii) TDMA (Tri diagonal matrix algorithm).

Iterations should be done until a converged solution is achieved [Versteeg and Malalasekera, 1995].

3.8 Solution Algorithm for Pressure-Velocity Coupling

Using this approach an equation for each component of the momentum equation and then the continuity equation are solved sequentially.The solution procedure of the generalized transport equations discussed in Section 3.2 can be summarized as:

1. Define the geometry of the case

2. Split the region of flow into cells (CV)

3. Integrate the equations of interest over each cell (Discretization)

4. Invert the resulting matrix

5. Repeat for as many times steps as necessary.

Navier-Stokes Equations (3.1 to 3.4) three-dimensional flow of incompressible fluid can be written in vector notation as:

$$
\begin{aligned}
&(i) \quad \nabla.\vec{u} = 0 \\
&(ii) \quad \nabla.(u\,u_x) = -\frac{1}{\rho}\frac{\partial P}{\partial x} + \nu \nabla^2 u_x \\
&(iii) \quad \nabla.(v\,u_y) = -\frac{1}{\rho}\frac{\partial P}{\partial y} + \nu \nabla^2 v_y \\
&(iv) \quad \nabla.(w\,u_z) = -\frac{1}{\rho}\frac{\partial P}{\partial z} + \nu \nabla^2 w_z
\end{aligned}
\qquad (3.17)
$$

Where $\nu = \mu / \rho$

For momentum, ignore 1st equation and concentrate on the momentum equations (ii),(iii) & (iv) of equation (3.17).These are transport equation form, with a source term i.e. $-\frac{1}{\rho}\left(\frac{\partial P}{\partial x_i}\right)$ and a diffusion term on the R.H.S.

However there are two main problems:

• The equation is non-linear that needs to be known $\vec{u}$ to evaluate the transport of *(u, v, w)* into the domain

• The source term involves *P*, which is one of the variables we want to solve for.

Both of these problems relate to the tangled nature of the NSE. Of the four equations making up the NSE (continuity and the three components of velocity) all components of velocity appears in all the equations, and the pressure appears in the three velocity equations. It is not possible to evaluate the velocity until to know the pressure, and vice versa. In order to find both, one value should be guessed and solve for the other, then go back and correct the first. It might start by guessing the pressure, and use this to get a better estimate of the velocity and then correct the pressure, etc.

If we consider the discretised form of the Navier-Stokes system, the form of the equations shows linear dependence of velocity on pressure and vice-versa. This inter-equation coupling is called velocity pressure coupling. A special treatment is required in order to velocity-pressure coupling.

FLUENT provides four segregated types of algorithms:

- SIMPLE (Semi-Implicit Method for Pressure-Linked Equations) - used for steady state problems
- SIMPLEC (SIMPLE-Consistent) - used for steady state problems
- PISO (Pressure Implicit Splitting of Operators) - for time dependent flows-used for time dependent and transient calculations
- Fractional Step or coupled.

It is noted that, from Equation (ii) if *p* and the flux $\left(\vec{u}\right)$ are known then u_j can be found.

Also, Equations (ii)-(iv) and (i) can be combined to give an equation for p given the flux:

$\nabla.\left[\frac{1}{A}\nabla p\right]$ - (flux term) that has to satisfy the continuity Equation (i).

The SIMPLE Scheme

A widely-used scheme for coupling the pressure and velocity is the SIMPLE (Semi Implicit Method for Pressure Linked Equations) scheme .The basic SIMPLE algorithm uses a relationship between velocity and pressure corrections to enforce mass conservation and to obtain the pressure field. If a steady-state problem is being solved iteratively, it is not necessary to fully resolve the linear pressure-velocity coupling, as the changes between consecutive solutions are no longer small. The SIMPLE algorithm is

- an approximation of the velocity field is obtained by solving the momentum equation. The pressure gradient term is calculated using the pressure distribution from the previous iteration or an initial guess.
- the pressure equation is formulated and solved in order to obtain the new pressure distribution.
- Velocities are corrected and a new set of conservative fluxes is calculated.

The Simple algorithm is as follows:

Guess an initial pressure field p^*

Use equation (i)-(iv) to create a velocity field u^* from this pressure field.

Find a correction p' to the pressure field

$$p^{**} = p' + p^*$$

Correct the velocity flux to obey continuity

In theory, p and $\underline{u}$ should now be the desired solution. In practice, it is necessary to repeat this procedure as an iterative process.

If new solution $p^{**}, \underline{u}^{**}$ adopted at each step $\rightarrow$algorithm becomes unstable.

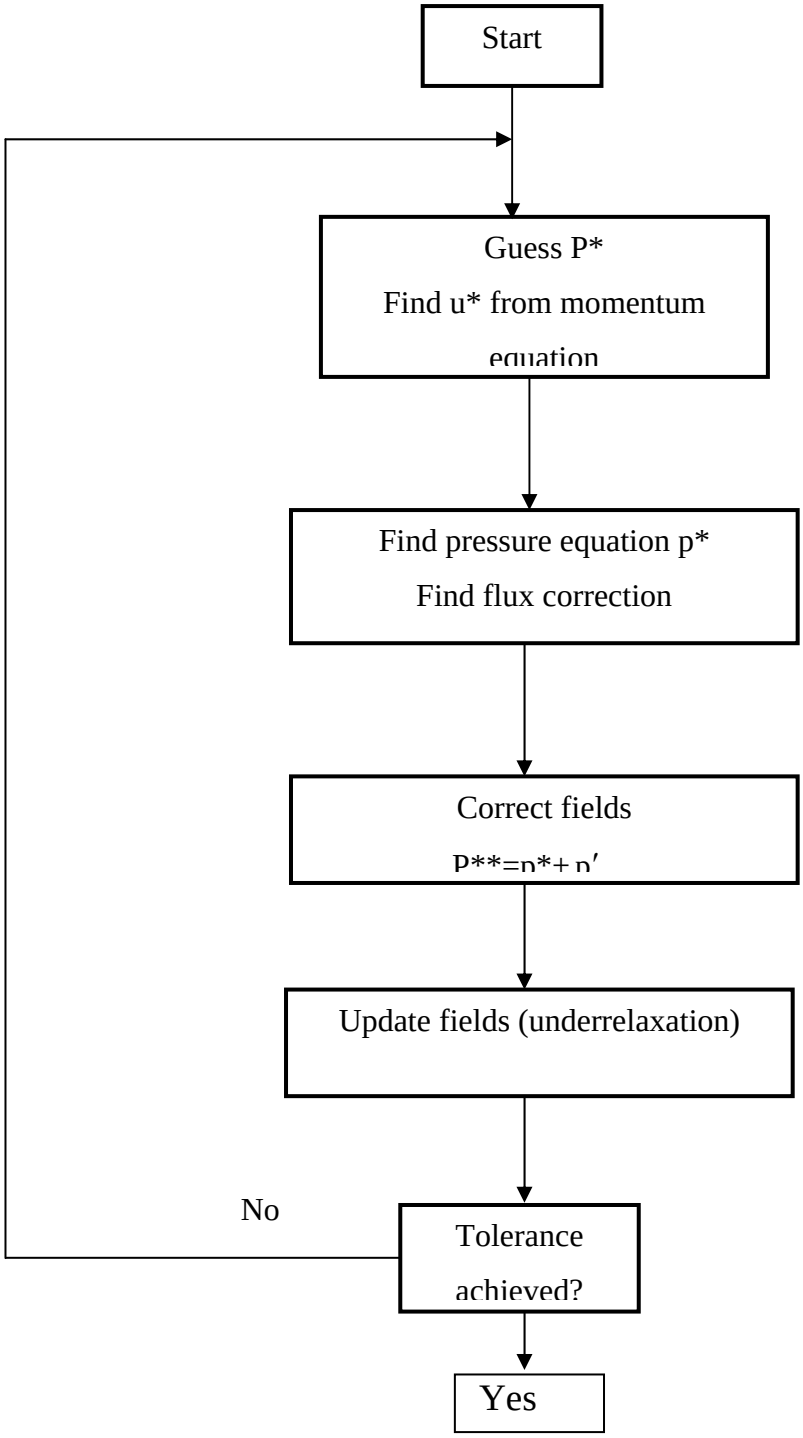

Figure 3.4: Flow Chart for SIMPLE Algorithm

Thus, use under relaxation :

Underrelax solution

$$p^{n+1} = \alpha p^{**} + (1-\alpha) p^{n}$$

α is under relaxation parameter. At each step of the iteration, the error in the solution (the residual) should decrease; residuals for all variables should be monitored to ensure this.

3.9 Spatial Discretisation

Fluent stores discrete values of the variables at the cell centres, however values of the variables are required at the cell faces for the convection terms in the equations and these must be interpolated from the centre values. In Fluent 6.3.26 this is accomplished using an upwind scheme and there are several alternatives: first-order upwind, second order upwind, power law and QUICK (Quadratic Upstream Interpolation Convective kinetics).

In the first order upwind scheme quantities at cell faces are determined by assuming that the cell-centre values of any variable represent a cell-average value and hold throughout the entire cell. Hence the face quantities are identical to the cell quantities. The Power-Law scheme is an improvement which interpolates the face value of a variable by using the exact solution to a one-dimensional convection-diffusion equation. When the flow is dominated by convection this implies that the face value of the variable is effectively equal to the cell value in the upwind direction. If the flow is weak and diffusion stronger then the Power-Law scheme amounts to a simple linear average of the value of the variable at the current cell location and the upstream cell. The Second-Order Upwind Scheme provides true second order accuracy by performing a Taylor series expansion of the cell-centered solution about centroid. The QUICK scheme also allows calculation of a higher-order value of the convected variable at the cell face by using a weighted average of second-order upwind and central interpolation.

3.10 Turbulence Modeling

Turbulence modeling is a key issue in most CFD simulations. Since most of the flows of engineering interest are turbulent, the appropriate treatment of turbulence will be crucial to the success of CFD. Turbulence could be thought of as instability of laminar flow that occurs at high Reynolds numbers. Whenever turbulence is present in a certain flow it appears to be the dominant over all other flow phenomena. The flow field of a Newtonian fluid is fully described by the Navier-Stokes equation. However, turbulent flows contain small fluctuations. The resolution of such small motions requires fine grids and time steps, such that a direct simulation becomes unfeasible for high Reynolds numbers. That is why successful modeling of turbulence greatly increases the quality of numerical simulations.

A review for the assessment of turbulence modeling is given by Spalart (2000). Commonly known models can be classified as follows:

- Zero and one equation models; Spalart-Allmaras model
- The• Reynolds stress model
- Algebraic stress model
- Detached eddy simulation (DES)model
- Larges eddy simulation (LES) model

Classes of Turbulence models

- RANS-based models
    - Linear eddy-viscosity models
        - Algebraic models
        - One and two equation models
    - Non-linear eddy viscosity models and algebraic stress models
    - Reynolds stress transport models
- Large eddy simulations
- Detached eddy simulations and other hybrid models

- Direct numerical simulations

In the present study, Reynolds-Averaged Navier-Stokes (RANS) is used for the simulation of turbulent flow. The RANS equations are time-averaged equations of motion for fluid flow. They are primarily used while dealing with turbulent flows. These equations can be used with approximations based on knowledge of the properties of flow turbulence to give approximate averaged solutions to the Navier-Stokes equations. To illustrate the influence of turbulent fluctuations on the mean flow we re-write the instantaneous continuity and Navier-Stokes equations for three dimensional flow of an incompressible Newtonian fluid.

$$\left.\begin{aligned} &\operatorname{div}\vec{u} = 0 \\ &\operatorname{div}(u\vec{u}) = -\frac{1}{\rho}\frac{\partial p}{\partial x} + \nu \operatorname{div}\operatorname{grad} u \\ &\operatorname{div}(v\vec{u}) = -\frac{1}{\rho}\frac{\partial p}{\partial y} + \nu \operatorname{div}\operatorname{grad} v \\ &\operatorname{div}(w\vec{u}) = -\frac{1}{\rho}\frac{\partial p}{\partial z} + \nu \operatorname{div}\operatorname{grad} w \end{aligned}\right\} \qquad (3.18)$$

Since div and grad are both differentiations then for a fluctuating vector $\vec{a} = \vec{A} + \vec{a}'$ and its combinations with a fluctuating scalar $\varphi = \Phi + \phi'$ we have the following relations (Versteeg and Malalasekera, 1995):

$$\begin{aligned} &\overline{\operatorname{div}\vec{a}} = \operatorname{div}\vec{A}; \qquad \overline{\operatorname{div}\operatorname{grad}\phi} = \operatorname{div}\operatorname{grad}\phi \\ &\overline{\operatorname{div}(\phi\vec{a})} = \operatorname{div}\left(\overline{\phi}\,\overline{\vec{a}}\right) = \operatorname{div}\left(\overline{\phi'\vec{a}'}\right) \end{aligned} \qquad (3.19)$$

To investigate the effects of fluctuations we replace in Equation (3.18) the flow variables $\vec{u}$ (hence also *u, v* and *w)* and *p* by the sum of a mean and fluctuating components. Thus

$$\vec{u} = \vec{U} + \vec{u'};\ u = U + u';\ v = V + v';\ w = W + w';\ p = P + p'$$

Then the time average is taken applying the rules stated in (3.19). Considering the continuity equation first we note that $\overline{\operatorname{div}\vec{u}} = \operatorname{div}\vec{U}$ .This yield the continuity equation for the mean flow

$$\text{div}\vec{U} = 0 \tag{3.20a}$$

A similar process is now carried out on the x-momentum equation. The time independent of the individual terms in this equation can be written as follows:

$$\overline{\text{div}(u\,\vec{u})} = \text{div}\left(U\,\vec{U}\right) + \text{div}\left(\overline{u'\,\vec{u}'}\right)$$

$$-\overline{\frac{1}{\rho}\frac{\partial P}{\partial x}} = -\frac{1}{\rho}\frac{\partial P}{\partial x};\ \overline{\nu\,\text{div}\,\text{grad}\,u} = \nu\,\text{div}\,\text{grad}\,U \tag{3.20b}$$

Substitution of these results gives the time-average *x*-momentum equation

$$\text{div}\left(U\vec{U}\right) + \text{div}\left(\overrightarrow{u'u'}\right) = -\frac{1}{\rho}\frac{\partial P}{\partial x} + \nu\ \text{div}\,\text{grad}\,U \tag{3.21a}$$

$$\text{div}\left(V\vec{U}\right) + \text{div}\left(\overrightarrow{v'u'}\right) = -\frac{1}{\rho}\frac{\partial P}{\partial y} + \nu\ \text{div}\,\text{grad}\,V \tag{3.21b}$$

$$\text{div}\left(W\vec{U}\right) + \text{div}\left(\overrightarrow{w'u'}\right) = -\frac{1}{\rho}\frac{\partial P}{\partial z} + \nu\ \text{div}\,\text{grad}\,W \tag{3.21c}$$

It is important to note that the 1st, 2nd, 3rd and 4th terms in Equations (3.21a, b &c) also appear in instantaneous Equations (3.18a-d)., but the process of time averaging has introduced new 3rd terms in the resulting time-average momentum equations. The terms involve products of fluctuating velocities and constitute convective momentum transfer due to the velocity fluctuations. It is customary to place these terms on the right hand sides of the equations (3.21a, b & c) to reflect their role as additional turbulent stresses on the mean velocity components *U*,*V* and *W*.

$$\text{div}\left(U\vec{U}\right) = -\frac{1}{\rho}\frac{\partial P}{\partial x} + \nu\ \text{div}\,\text{grad}\,U + \left[-\frac{\partial\overline{u'^2}}{\partial x} - \frac{\partial\overline{u'v'}}{\partial y} - \frac{\partial\overline{u'w'}}{\partial z}\right] \tag{3.22a}$$

$$\text{div}\left(V\vec{U}\right) = -\frac{1}{\rho}\frac{\partial P}{\partial y} + \nu\ \text{div}\,\text{grad}\,V + \left[-\frac{\partial\overline{u'v'}}{\partial x} - \frac{\partial\overline{v'^2}}{\partial y} - \frac{\partial\overline{v'w'}}{\partial z}\right] \tag{3.22b}$$

$$\text{div}\left(W\vec{U}\right) = -\frac{1}{\rho}\frac{\partial P}{\partial z} + \nu\ \text{div grad}\, W + \left[-\frac{\partial \overline{u'w'}}{\partial x} - \frac{\partial \overline{v'w'}}{\partial y} - \frac{\partial \overline{w'^2}}{\partial z}\right] \qquad (3.22c)$$

The extra stress terms have been written out in longhand to clarify their structure. Theresult from six additional stresses, three normal stresses and three shear stresses:

$$\tau_{xx} = -\rho\overline{u'^2}, \tau_{yy} = -\rho\overline{v'^2}, \tau_{zz} = -\rho\overline{w'^2}, \tau_{xy} = \tau_{yx} = -\rho\overline{u'v'}$$
$$\tau_{xz} = \tau_{zx} = -\rho\overline{u'w'}\ \ , \tau_{yz} = \tau_{zy} = -\rho\overline{v'w'}$$

These extra turbulent stresses are termed the Reynolds stresses. In turbulent flows the normal stresses $-\rho\overline{u'^2}$, $-\rho\overline{v'^2}$ and $-\rho\overline{w'^2}$ are always non-zero because they contain squared velocity fluctuations. The shear stresses $-\rho\overline{u'v'}$, $-\rho\overline{v'w'}$ and $-\rho\overline{w'u'}$ are associated with correlations between different velocity components. If, for instance, u', v' and w' are statistically independent fluctuations, the time-independent of their product $\overline{u'v'}, \overline{v'w'}$ and $\overline{w'u'}$ would be zero. However, the turbulent shear stresses are also non-zero and usually very large compared to the viscous stresses in a turbulent flow. The set of Equations (3.22 a, b & c) is called Reynolds equations. Similar extra turbulent transport terms arise when we derive a transport equation for an arbitrary scalar quantity.

Some models are used to solve the RANS equations. In this study the following models are used for the investigation of the incompressible turbulent flow over the underwater body.

- One equation model: The Spalart-Allmaras
- Two equation model: i) The *k*-*ε* model

  ii) The *k*-*ω* model

Models like the *k*-*ε* and the *k*-*ω* have become industry standard models and are commonly used for most of the fluid-engineering problems. Two equation turbulence models are also very much an active area of research and new refined two-equation models are still being developed.

3.10.1 The Spalart-Allmaras (S-A) Model

The Spalart-Allmaras turbulence model is a simple one equation model that solves a modeled transport equation for the turbulent viscosity. This model is designed for wall-bounded flows and gives good results for boundary layers subjected to adverse pressure gradients, much like the flow fields encountered in this study. Although the original Spalart-Allmaras model requires that the viscous-affected region of the boundary layer be properly resolved through the use of a fine mesh inside the boundary layer, the model has been modified for its implementation in FLUENT so that wall functions are used when the mesh resolution is not sufficiently fine near object surfaces. The fact that the S-A model is a one-equation model with relatively lax grid density requirements further enhances its suitability for this particular study since, for the computer platform used, maximum computational efficiency is critical. The transported variable in the Spalart-Allmaras model, $\bar{\nu}$ is identical to the turbulent kinematic viscosity except in the near-wall (viscous-affected) region (Fluent Inc. 2005).

The transport equation for $\bar{\nu}$ is

$$\frac{\partial}{\partial t}\left(\rho\bar{\nu}\right)+\frac{\partial}{\partial x_i}\left(\rho\bar{\nu}u_i\right)=G_\nu+\frac{1}{\sigma_{\bar{\nu}}}\left[\frac{\partial}{\partial x_j}\left\{\left(\mu+\rho\bar{\nu}\right)\frac{\partial\bar{\nu}}{\partial x_j}\right\}+C_{b2}\rho\left(\frac{\partial\bar{\nu}}{\partial x_j}\right)^2\right]-Y_V+S_{\bar{\nu}} \qquad (3.24)$$

Where, G_ν is the production of turbulent viscosity and Y_ν is the destruction of turbulent viscosity that occurs in the near-wall region due to wall blocking and viscous damping. $\sigma_{\bar{\nu}}$ and C_{b2} are constants and ν is the molecular kinematic viscosity. $S_{\bar{\nu}}$ is a user-defined source term. Note that the turbulence kinetic energy k is not calculated in the Spalart-Allmaras model.

To obtain the modified turbulent viscosity, ν, for the Spalart-Allmaras model from the turbulence intensity, I and length scale, l, the following equation can be used:

$$\nu=\sqrt{\frac{3}{2}}U_{avg}Il \qquad (3.25)$$

Where, $l=0.07\times L$

and $I=0.16\left(\mathrm{Re}\right)^{\frac{1}{8}}$

In this model the constants are considered as:

$C_{bi} = 0.1355, C_{b2} = 0.622, C_{v1} = 7.1, C_{w2} = 0.03, C_{w3} = 2, P_r = 0.667$

3.10.2 The *k*-*ε* Model

The *k*- *ε* model is one of the most common turbulence models. It is a two equation model that means, it includes two extra transport equations to represent the turbulent properties of the flow. This allows a two equation model to account for history effects like convection and diffusion of turbulent energy. The first transported variable is turbulent kinetic energy, (k). The second transported variable in this case is the turbulent dissipation, (ε). It is the variable that determines the scale of the turbulence, whereas the first variable, k, determines the energy in the turbulence (Fluent Inc. 2005). In this study, Standard *k*-*ε* model and Realizable k-ε model are used to simulate the flow around the hull of a ship.

In the derivation of the $k-\varepsilon$ model, it was assumed that the flow is fully turbulent, and the effects of molecular viscosity are negligible. The standard $k-\varepsilon$ model is therefore valid only for fully turbulent flows.

3.10.2.1 The Standard *k*-*ε* Model

The Standard *k*-*ε* turbulence model is presently the most widely applied turbulence model to practical engineering flows as it is robust, economical and provides reasonable accuracy for a wide range of flows. The standard $k-\varepsilon$ model is a semi-empirical model based on model transport equations for the turbulence kinetic energy *k* and its dissipation rate ε The model transport equation for *k* is derived from the exact equation, while the model transport equation for ε was obtained using physical reasoning and bears little resemblance to its mathematically exact counterpart..

Transport Equations for the Standard *k*-*ε* Model for turbulence kinetic energy, *k*, and its

rate of dissipation *ε*, are:

$$\rho u_i \frac{\partial k_j}{\partial x_i} = \frac{\partial}{\partial x_j}\left[\left(\mu + \frac{\mu_t}{\sigma_k}\right)\frac{\partial \varepsilon}{\partial x_j}\right] + G_k + G_b - \rho\varepsilon - Y_m + S_k \qquad (3.26)$$

$$\rho u_i \frac{\partial \varepsilon_j}{\partial x_i} = \frac{\partial}{\partial x_j}\left[\left(\mu + \frac{\mu_t}{\sigma_\varepsilon}\right)\frac{\partial \varepsilon}{\partial x_j}\right] + C_{1\varepsilon}\frac{\varepsilon}{k}\left(G_k + C_{3\varepsilon}G_b\right) - C_{2\varepsilon}\rho\frac{\varepsilon^2}{k} + S_\varepsilon \qquad (3.27)$$

In these equations G_k represents the generation of turbulent kinetic energy due to mean velocity gradients, G_b is the generation of turbulent kinetic energy due to buoyancy, Y_m represents the contribution of the fluctuating dilation in compressible turbulence to the overall dissipation. $C_{1\varepsilon}, C_{2\varepsilon}$ and $C_{3\varepsilon}$ are constants. σ_k and σ_ε are the turbulent Prandtl numbers for k and ε, respectively. S_k and S_ε are user-defined source terms.

The remaining constants applied in the Standard $k-\varepsilon$ turbulence model are equal to:

$$C_{1\varepsilon} = 1.44, C_{2\varepsilon} = 1.92, C_\mu = 0.09, \sigma_k = 1.0, \sigma_\varepsilon = 1.3$$

3.10.2.2 Realizable *k*- *ε* Model

In Realizable $k-\varepsilon$ model it satisfies certain mathematical constraints on the normal stresses, consistent with the physics of turbulent flows. The most straightforward way to ensure the realizability is to make C_μ variable by sensitizing it to the mean flow (mean deformation) and the turbulence (k, ε). The modeled transport equations for k is similar to Equation (3.26) and ε in the realizable *k-ε model* are

$$\rho u_i \frac{\partial \varepsilon}{\partial x_i} = \frac{\partial}{\partial x_j}\left[\left(\mu + \frac{\mu_t}{\sigma_\varepsilon}\right)\frac{\partial \varepsilon}{\partial x_j}\right] + \rho C_1 S_\varepsilon - \rho C_2 \frac{\varepsilon^2}{k + \sqrt{\nu\varepsilon}} + C_{1\varepsilon}\frac{\varepsilon}{k}(C_{3\varepsilon}G_b) + S_\varepsilon \qquad (3.28)$$

Where, $C_1 = \max\left[0.43, \frac{\eta}{\eta+5}\right]$, $\eta = S\frac{k}{\varepsilon}$, $S = \sqrt{2S_{ij}S_{ij}}$

In these equations, G_k represents the generation of turbulence kinetic energy due to the mean velocity gradients, G_b is the generation of turbulence kinetic energy due to buoyancy, Y_M represents the contribution of the fluctuating dilatation in compressible turbulence to the overall dissipation rate, C_2 and $C_{1\varepsilon}$ are constants. σ_k and σ_ε are turbulent Prandtl numbers for k and ε, respectively. S_k and S_ε are user defined source terms.

The turbulence kinetic energy, k is given by $k = \frac{3}{2}\left(U_{avg} I\right)^2$

Where, U_{avg} is the mean flow velocity.

The turbulence intensity *I* and is the turbulence length *l* can be found from the following equations:

$l = 0.07 \times L$ and $I = 0.16(\mathrm{Re})^{\frac{1}{8}}$

Also, the turbulence dissipation rate ε defined as

$$\varepsilon = C_{\mu}^{\frac{3}{4}} \frac{k^{\frac{3}{2}}}{l}$$

The constants applied in the Realisable k-ε turbulence model are equal to:

$\sigma_k = 1.0, \sigma_\varepsilon = 1.3, C_1 = 1.9$

3.10.3 The *k-ω* Turbulence Model

The Standard *k-ω* turbulence model incorporates modifications for low-Reynolds number effects and shear flow spreading. The shear flow spreading rates are in close agreement with measurements for far wakes, mixing layers, and plane, round, and radial jets, and are thus applicable to wall-bounded and free shear flows. In present work, Shear-Stress Transport (SST) *k-ω* (Fluent Inc.2005) are used to simulate the flow around the hull.

3.10.3.1 SST *k-ω* model

The SST *k-ω* turbulence model is a conglomeration of the robust and accurate formulation of the Standard *k-ω* model in the near-wall region, with the Standard *k-ε* in the far field. The SST *k-ω* is more accurate and reliable for a wider class of flows than the Standard *k-ω*, including adverse pressure gradient flows.

Transport equations for the SST *k-ω* model are given by:

$$\rho u_i \frac{\partial k}{\partial x_i} = \frac{\partial}{\partial x_j}\left(\Gamma_k \frac{\partial k}{\partial x_j}\right) + \tilde{G}_k - Y_k + S_k \qquad (3.29)$$

$$\rho u_i \frac{\partial \omega}{\partial x_i} = \frac{\partial}{\partial x_j}\left(\Gamma_\omega \frac{\partial \omega}{\partial x_j}\right) + G_\omega - Y_\omega + D_\omega + S_\omega \qquad (3.30)$$

In these equations, $\tilde{G}_k$ represents the generation of turbulence kinetic energy due to mean velocity gradients, G_ω represents the generation of ω, Γ_k and Γ_ω represent the effective diffusivity of k and ω, respectively, Y_k and Y_ω represent the dissipation of k and ω due to turbulence, D_ω represents the cross-diffusion term, S_k and S_ω are user -defined source terms.

It is so named because the definition of the turbulent viscosity is modified to account for the transport of the principal turbulent shear stress. It is such a feature that gives the SST k-ω model an advantage in terms of performance over both the standard k-ε and realizable *k-ε* model. Other modification includes the addition of a cross-diffusion term in the k-*ω* equation and a blending function to ensure that the model equations behave appropriately in both the near-wall and far-field zones. In SST *k-ω* model the specific dissipation rate *ω* can be found by

$$\omega = \frac{k^{\frac{1}{2}}}{C_\mu^{\frac{1}{4}} l}$$

The constants applied in the high Reynolds number form of the SST *k*-ω turbulence model are equal to:

k =0.41 and $C_\mu = 0.09$.

3.11 Ideal Turbulence Model

Solving CFD problem usually consists of four main components: geometry and grid generation, setting-up a physical model, solving it and post-processing the computed data. The way geometry and grid are generated, the set problem is computed and the way acquired data is presented is very well known. Precise theory is available. Unfortunately, that is not true for setting-up a physical model for turbulence flows. The problem is that one tries to model very complex phenomena with a model as simple as possible.

Therefore an ideal model should introduce the minimum amount of complexity into the modeling equations, while capturing the essence of the relevant physics.

Complexity of the Turbulence Model

Complexity of different turbulence models may vary strongly depends on the details one wants to observe and investigate by carrying out such numerical simulations. Complexity is due to the nature of Navier Stokes equation (N-S equation). N-S equation is inherently nonlinear, time-dependent, three-dimensional partial differential equation.

Turbulence could be thought of as instability of laminar flow that occurs at high Reynolds numbers (Re). Such instabilities origin form interactions between non-linear inertial terms and viscous terms in N-S equation. These interactions are rotational, fully time-dependent and fully three-dimensional. Rotational and two-dimensional interactions are mutually connected via vortex stretching. Vortex stretching is not possible in three dimensional spaces. That is also why no satisfactory three-dimensional approximations for turbulent phenomena are available.

Furthermore turbulence is thought of as random process in time. Therefore no deterministic approach is possible. Certain properties could be learned about turbulence using statistical methods. These introduce certain correlation functions among flow variables. However it is impossible to determine these correlations in advance.

3.12 Grid Considerations for Turbulent Flow Simulations(Y^+)

Successful computations of turbulent flows require some consideration during the mesh generation. Since turbulence (through the spatially-varying effective viscosity) plays a dominant role in the transport of mean momentum and other parameters, one must ascertain that turbulence quantities in complex turbulent flows are properly resolved if high accuracy is required. Due to the strong interaction of the mean flow and turbulence, the numerical results for turbulent flows tend to be more susceptible to grid dependency than those for laminar flows. It is therefore recommended that, one resolve with sufficiently fine meshes, the regions where the mean flow changes rapidly and there are shear layers with a large mean rate of strain. Three parameters are significant for a computational grid; total number of grid points, location of outer computational

boundaries, and minimum spacing (initial spacing normal to body surface). RANS computation on similar geometry usually guides the determination of minimum spacing of grid from wall. The minimum spacing is generally based on $y+$, a dimensionless parameter representing a local Reynold's number with standard wall function. This parameter is defined as:

$$y^+ \approx \frac{yu^*}{\nu} \tag{3.31}$$

Where, y = distance from the wall surface

u^* = frictional velocity

ρ = density

ν = kinematic viscosity

It is recommended that, for standard wall function in $k-\varepsilon$ model or when transitional flows option is not active in $k-\omega$ model the y-plus value should be $30 < y^+ < 300$. (y^+ value close to the lower bound $y^+ = 30$ is most desirable.) On the other hand, for enhanced wall treatment in k-ε model or when transitional flows option is enabled in SST k-ω model the y^+ at the wall-adjacent cell should be on the order of $y^+ = 1$.It should be noted here that the y^+ value is based on a turbulent boundary layer on a flat plate. Therefore, it is used only as an estimate in the present case as the geometry is not actually a flat plate. The y^+ values are also solution dependent. The actual value of y^+ for the hull form is obtained with the viscous flow solution. Furthermore, the real y^+ is not a constant but varies over the wall surface according to the flow in the boundary layer.

CHAPTER 4

4. NUMERICAL SIMULATION

The numerical simulation is conducted in two distinct stages. Firstly, computational models are created and simulations are run on 3d turbulent models on the hull of a ship. At first the main concentration is carried out for the simulation on the influence of different turbulence models like Standard k-ε, Realizable k-ε and Shear Stress Transport (SST) k-ω model. Secondly the computed results are compared to experimental and other numerical results to validate the computational models. All of the investigations are carried out using very efficient commercial software FLUENT 6.3.26.

4.1 Simulation Using FLUENT 6.3.26 Based on Finite Volume Method

FLUENT 6.3.26 uses a finite volume-based algorithm to transform the governing physical equations to algebraic equations that can be solved numerically. In such an approach, the computational domain is subdivided into individual, discrete control volumes, or cells. The governing equations about each cell are then integrated, yielding discrete equations that conserve each quantity on a control-volume basis. Consider the following steady-state conservation equation for transport of a scalar quantity ϕ written in integral form for an arbitrary control volume V (Fluent Inc., 2005):

$$\int \rho\varphi \vec{v}.\vec{dA} = \int \Gamma_{\varphi} \vec{\nabla} \varphi.\vec{dA} + \int_{V} S_{\varphi} dV \qquad (4.1)$$

where ρ = density

$\vec{v}$ = velocity vector (= $ui + vj + wk$ in 3D)

$\vec{A}$ = surface area vector

Γ_φ = diffusion coefficient for φ

$\vec{\nabla}$ = gradient of φ

S_φ = source of φ per unit volume

This equation is applied to each cell in the computational domain. FLUENT discretizes this integral equation as:

$$\sum_{f}^{N_{faces}} \nu_f \varphi_f A_f = \sum_{f}^{N_{faces}} \Gamma_\varphi \left(\vec{\nabla} \varphi \right)_n A_f + S_\varphi V \tag{4.2}$$

Where, N_{faces} = number of faces enclosing cell

φ = value of φ convected through face f

$\vec{\nu}_f$ = mass flux through the face

A_f = area of face f, $|A|$

$(\nabla \phi)_n$ = magnitude of $\vec{\nabla} \varphi$ normal to face f

V = cell volume

The equations solved by FLUENT that lead to a full description of the flow field around a given object take the same form as the discretized equation above (Fluent Inc., 2005).

4.2 Steady Flow over the hull of a ship

4.2.1 Geometric Modeling

The Wigley and Series 60 hull was selected as the benchmark to gain understanding of free surface simulations using CFD. The focus of the analysis is in modeling and comparison for the Wigley hull as a single body. This is a standard hull shape, which is defined by a parabolic profile for the beam(width of the hull),overall length and the draft(distance from the bottom of the hull to the water surface),as opposed to the

elevation, that is defined by a rectangular profile. The numerical form of the wigley hull is given by

$$y = \frac{B}{2}\left(1-\left(\frac{2x}{L}\right)^2\right)\left(1-\left(\frac{z}{D}\right)^2\right) \tag{4.3}$$

Where B is the maximum beam, L is the length of the vessel, D is the draft. For this study, this relationship between these three parameters will be given by 1:1/10:1/16. These values were calculated using the vessel's solid model and considering it as constant density which is an acceptable initial approximation.

4.3 Computational Approaches to Free Surface Modelling

An important aspect of any simulation of the fluid flow around a surface ship is the method used to model the air/water interface. Thanks to the advent of high performance computing, Computational fluid dynamics (CFD) techniques solving the Navier- Stokes equations are now abundant and widely used for various types of fluid flow problems. Free-surface wave flow is one of the subjects, which draws attention in the CFD community for hydraulics and hydrodynamics applications.

4.3.1 Free Surface

For Navier-Stokes equations there are two different types of free-surface wave solution methods: interface tracking and interface capturing. In the interface tracking methods only the waterside of the domain is simulated and the grid is adjusted to conform to the position of the free surface. Interface tracking methods track the free-surface by satisfying the kinematic condition and conform the grid to the interface every time step or iteration. Once the grid has been conformed, the Navier-Stokes equations are solved with dynamic free-surface boundary conditions on the free surface. These methods accurately predict the free surface, are computationally less demanding, but cannot handle highly distorted or breaking waves. Also it is sometimes difficult to conform to complex geometry, and grid quality degrades during the conforming process.

In the interface capturing approach, the computational domain includes both the water and air, and the location of the interface on the mesh is computed from the solution of an auxiliary equation. Interface capturing methods, on the other hand, capture the free

surface by solving a transport equation for the fraction of the cell occupied by the liquid phase, as in the volume of fluid (VOF) method (Hirt and Nichols 1981).This method are suitable for complex geometries and known to be the most general for free-surface wave flow simulations and adopted in many CFD codes with various numerical techniques. In our work, the VOF method implemented in a RANS solver was employed to simulate the free surface wave flow around two hulls. The method has been validated on two standard ship hull form , that is the wigley parabolic hull and the series 60.

4.4 Computational Domain

The ship model used for this study is Wigley parabolic and Series 60, which are standard for ship-hydrodynamics research, and are chosen because these are used by ITTC research program. Two types of hull modes used for the experimental and computational test are, given bellow, and the longitudinal profiles of the 3D model are shown in Figure 4.1 (a) and 4.1(b)

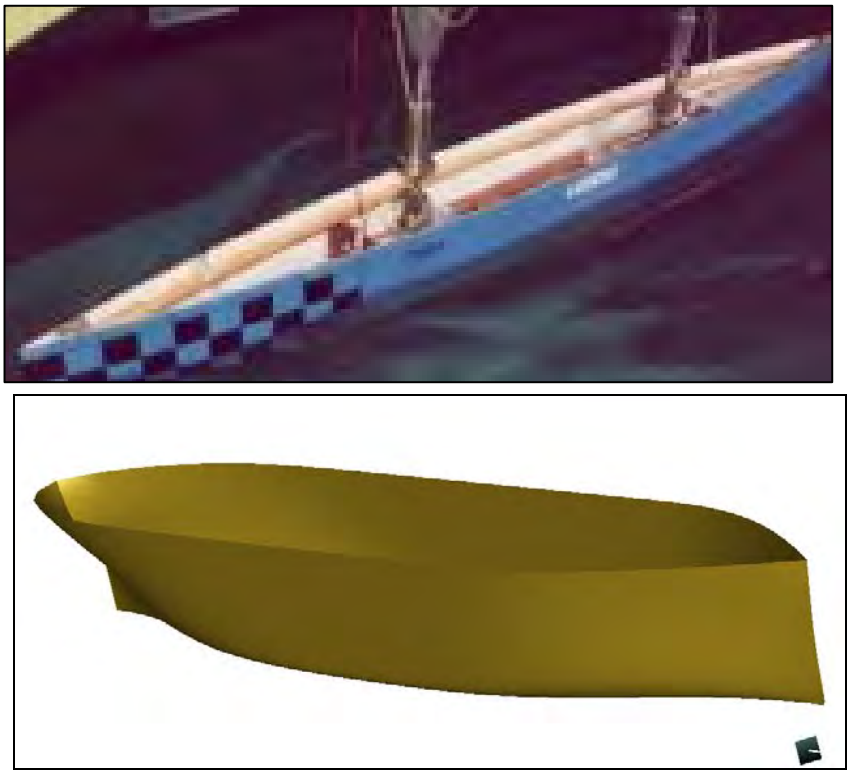

(b)

Figure 4.1: (a) Hull of Model Wigley (b) Hull of Model Series 60.

The flow from left to right submersed in an incompressible fluid is considered. The parabolic hull is located at the upper middle position of a rectangular flow domain. The hull is modeled as an ellipse and a square flow domain is created surrounding the hull. The computational domain consists of 10 times of the length of hull, 10 times of the beam and 10 times draught of the hull .Due to symmetry of the flow the calculations were carried out for full length of ship. Computations were performed in model scale for reduction of the computational effort. The flow was computed in rectangular domain surrounding the hull. A physical domain with water and air at standard conditions was specified.An homogeneous model allows two different phases when the interface is distinct and well defined everywhere, as it is the case of hulls riding on a free surface without breaking waves The control volume was made with these dimensions to ensure fully developed flow, and to be certain that the fluid/wall interactions of the control volume would not influence the frictional resistance calculations on the Wigley and Series 60 hull.

Table 4.1: Principal particulars of Wigley and Series 60 model

Parameters	Wigley	Series 60
Length Between Perpendicular([L_{PP})	1.00(m)	1.0(m)
Breadth (B)	0.1(m)	0.1333(m)
Draft (D)	0.0625(m)	0.053(m)
Block Coefficient(C_B)	0.44	0.60
Wetted surface area	0.135(m^2)	0.168(m^2)
L/B	10	7.5
L/D	16	18.75

4.5 Grid Generation

GAMBIT, the preprocessor of FLUENT 6.3.26 is used to generate the three-dimensional grid around a hull in this study. The quality and efficiency of the numerical

simulation is highly dependent on the construction of the grid used in the computational model. A typical computational mesh both for the two models is used for simulation shown in the following figures 4.2 and 4.3.

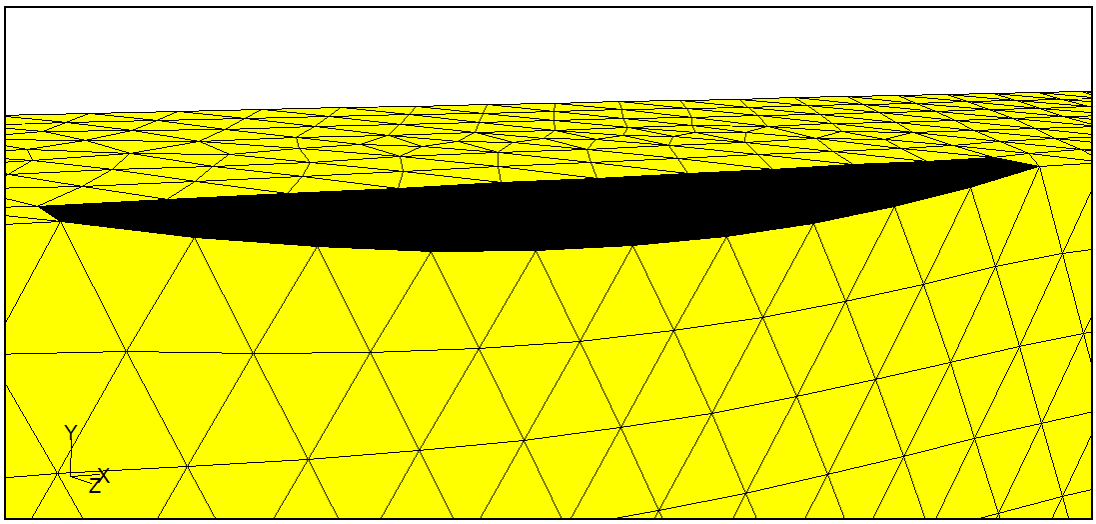

Figure 4.2: Grid Lines in Mesh around the Hull of Wigley

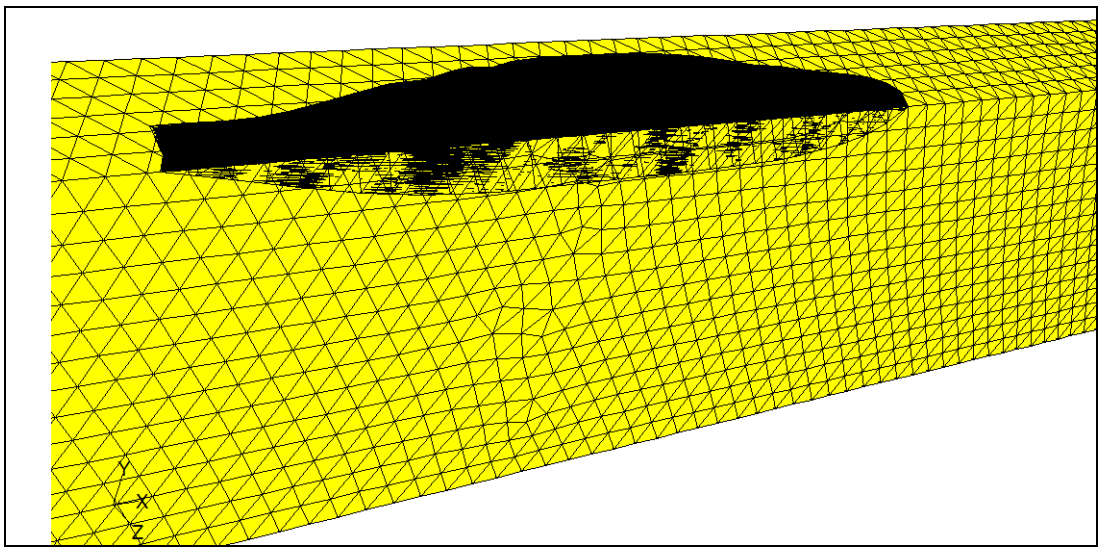

Figure 4.3: Grid Lines in Mesh around the Hull of Series 60

Several factors must be considered when generating a grid to ensure that the best possible numerical results are obtained with a particular solution algorithm. Grid point placement can have a substantial effect on the stability and convergence of the numerical solver. In order for a computational fluid dynamics code to provide a complete flow field description for a particular problem, the user must specify a grid that tells the flow solver at what locations in the problem domain the solution is to be computed. The specification of the grid's construction can have a major influence on the fidelity of the solution and can, in fact determine whether a solution is even attainable.

4.5.1 Mesh Studies

The particular mesh both for model Wigley and series 60 are given below in the following table with considerable mesh concentration around the hull.. To facilitate meshing, we employed a C-type grid system around the hull. Generally speaking, a value of 10x10x10 determinant over 0.4, and an aspect Ratio between 100 and 500 are good indicatives that a mesh could work properly.

Table 4.2: Mesh analysis of Wigley and Series 60 model

	Wigley	Series 60
nodes	9322	11258
wall faces	22	24
velocity-inlet faces	146	160
pressure outlet faces	146	158
interior faces	83977	101046
tetrahedral faces	43887	52835

4.5.2 Grid Study

A detailed grid study around the hull is carried out for the i) Wigley Parabolic and ii) Series 60 model ship using the commercial software FLUENT 6.3.26. The flow geometry, the inlet and outlet conditions are specified in Figure 4.5. The grid clustering near the ship hull to capture the velocity gradient can yield cells with high aspect ratio, potentially resulting in highly skewed grids. The *C*-grid topology is adopted, and the boundary condition used in the simulations is shown also in that figure 4.5.

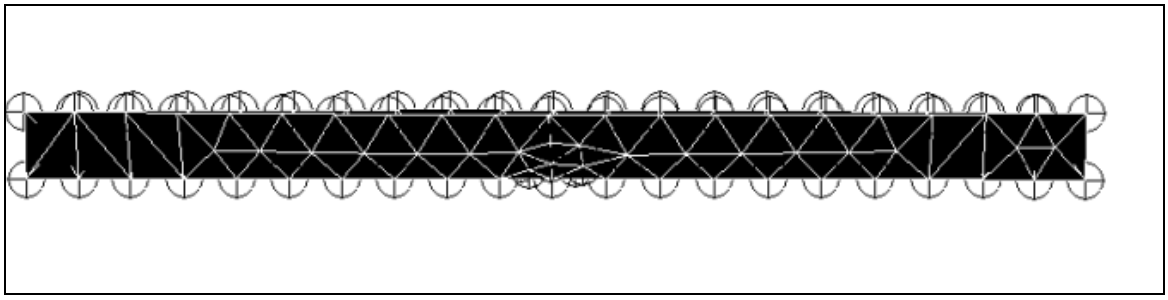

(a)

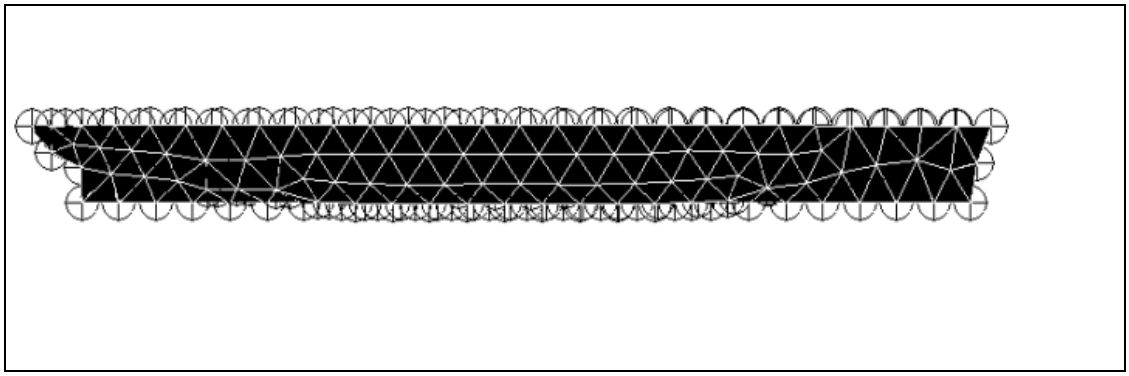

(b)

Figure 4.4: Grid Display with Nodes around the Hull of (a) Wigley and (b) Series 60.

First of all to minimize the CPU time, we tried to create a mesh topology that would allow a coarse grid in the region around the hull .The first configuration is rejected due to lack of required minimum spacing near the hull. Since selecting a few Grid do not provide good results, adaptation of region near the hull surface is performed since more cells are needed near the hull surface to obtain results with high accuracy. Three typical mesh densities can be chosen for analysis of grid sensitivity. We consider coarse mesh respectively. Small difference exists in pressure distribution with medium and fine mesh but there is a large discrepancy for using coarse mesh.

4.6 Initial Condition

There are three initial conditions that must be controlled in order to speed up the solutions and reduce the CPU time required. The first one is the pressure, which is configured as the hydrostatic pressure of flat wave field function, i.e., the current of the wave applies certain initial pressure, and the software calculates this value and reflects it in the initial condition. Secondly the velocity is set up as the velocity of the hull wave

field function, which reflects the wave current parameters in order to avoid the superposition of values. The third step is to set up the volume fractions of each one of the fluids. Thus the water and the air are set up as the volume fraction of heavy fluid and volume fraction of light fluid, respectively.

4.7 Boundary Condition

Four boundary conditions of the respective domain are used in this study. These are:

- The upstream
- The downstream
- Wall
- Symmetry

The upstream and the downstream boundary of the domain are modeled as velocity inlet and pressure outlet respectively and both the upper side , lower side and the side part of the domain have symmetry boundary conditions. The surface of the hull of the domain are modeled as a wall

For computations with a free surface, the water velocity is set (at the inlet) equal to the hull speed being investigated, but in the opposite direction. The air velocity is set equal to the water velocity, if a no wind condition is assumed, or otherwise in any other direction and speed.

For incompressible flows, as in the case of the flow around hulls, the inlet boundary condition can be specified at that portion of that boundary where the velocity distribution is known, usually in front of the hull. A velocity inlet boundary condition is used upstream; the flow velocity is considered equal to the velocity experimental of the model using the cases of experimental measurement to wave profile. The free surface elevation is fixed at the inlet. As this boundary condition is intended for incompressible flows where the magnitude and direction of the inlet velocity is known. The velocities are set to given values, and the first derivative of the pressure with respect to the axial direction is taken equal to zero.

$$(u, v, w) = (u, v, w)_{given} \ , \qquad \frac{\partial p}{\partial n} = \frac{\partial p}{\partial x} = 0$$

The outlet boundary condition is usually specified where the flow leaves the computational domain and where it can be assumed that the zero gradient condition applies. A hydrostatic pressure outlet boundary condition is used downstream; the hydrostatic pressure at the outlet is calculated assuming an undistributed free surface

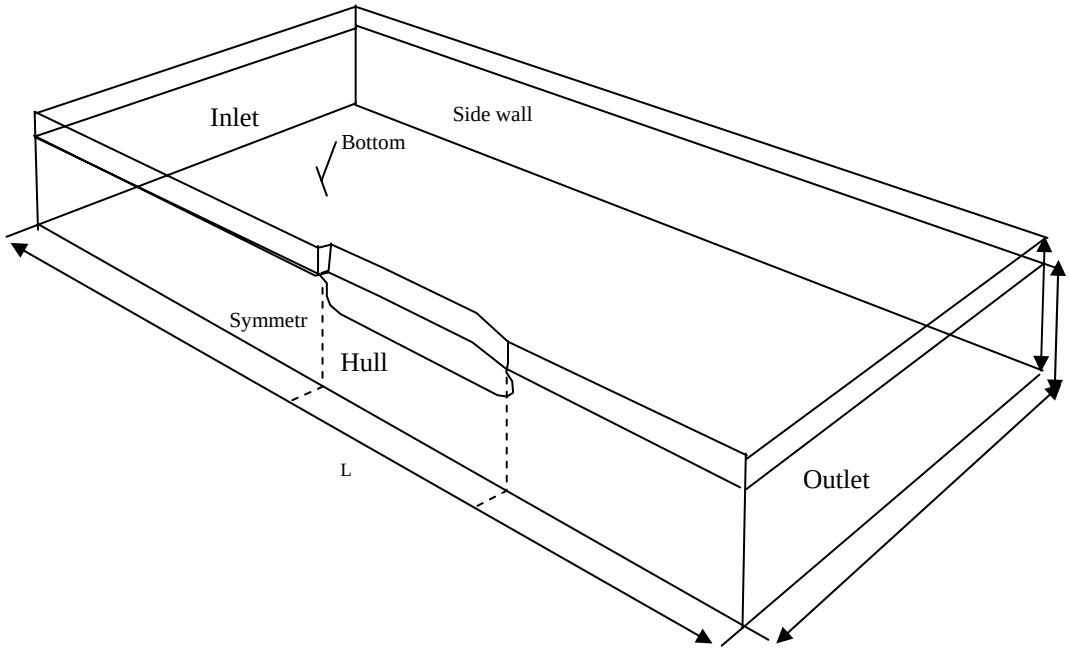

Figure 4.5: Schematic Diagram of the Flow Field around Hull with Boundary Condition.

The pressure outlet boundary condition is used to model flow exit where the details of the flow and gauge pressure are not known. Pressure outlet boundary conditions require the specification of a static (gauge) pressure at the outlet boundary.

On the other hand , the Y=0 plane was created as a symmetry plane in the boundary conditions in order to save computational resources in the simulation time by splitting the geometry in half. Symmetry boundary conditions are used for the physical geometry of interest, and the expected pattern of the flow solution. They can also be used to model zero-shear slip walls in viscous flows.

Fluent assumes a zero flux of all quantities across a symmetry boundary. There is no convective flux across a symmetry plane: the normal velocity component at the

symmetry plane is zero. There is no diffusion flux across a symmetry plane: the normal gradients of all flow variables are zero at the symmetry plane. The symmetry boundary condition can therefore be summarized as follows:

Zero normal velocity at a symmetry plane

Zero normal gradients of all variables at a symmetry plane

Since the shear stress is zero at a symmetry boundary, it can also be interpreted as a 'slip wall' when used in viscous flow calculations.

$$\frac{\partial p}{\partial n} = \frac{\partial u}{\partial n} = 0, \qquad v = w = 0$$

Finally, the hull of the ship was selected as no slip wall condition in order to model the viscous boundary layer effect on these surfaces.

4.8 Solver Initialization and Flow Solution

After the grids are constructed, the next step is to import them into FLUENT 6.3.26 the numerical solver. Since each grid is exported from GAMBIT in FLUENT 6.3.26's native format, the import process is straightforward. After the grids are imported, the solver is initialized. This procedure involved several steps, such as:

-Selecting the solver formulation

-Defining physical models

-Specifying fluid properties

-Specifying boundary conditions

-Adjusting residual

-Initializing the flow field

-Iterating

For all of the grids generated in this study, the pressure based solver formulation is used. This approach solves the continuity, momentum, and energy equations sequentially as

opposed to simultaneously. Because the pressure based solver is traditionally used for incompressible and mildly compressible flows, given the flow conditions being investigated, this study is well-tailored for its use. Next, the flows around the geometries modeled in this study are approximated as steady-state. Although this choice precluded the ability to capture other time-dependent effects, the majority of pertinent flow features and their associated drag effects (like separation point, pressure drag, and skin friction drag) could still be accurately modeled. One reason for choosing steady-state simulations is because of the reduced computational load they placed on the computer – given the total number of simulations needed, run time is a major limiting factor. The other, more compelling reason for choosing a steady-state modeling approach is that the properties of interest in this study is steady state values. Although, in reality, pressure, drag and wave profile all vary with respect to time on a microscopic scale, their net values and net effects can usually be considered steady properties and can accurately be modeled as such. The user interface updates based upon whether the steady or unsteady solver is selected. The time step size, the number of iterations per time step, the total number of time steps, and the convergence limit for each time step needs be specified when the unsteady solver is used. On the other hand, the total number of iterations and the convergence limit needs to be specified for steady solver.

For the geometries modeled in this research, definition of the physical model simply involves specifying turbulent simulation is desired in the solution computation. A turbulent model of two different hulls is also simulated to compare with experimental results. In this stage, the k-ε model with standard wall function is used in all of the cases. For velocity- pressure coupling the SIMPLE algorithm is used for steady case. The Presto scheme for the pressure equation and QUICK discretization for momentum equation are used throughout this study.

The VOF model is a simplified multiphase model that can be used to model multiphase flows where the phase moves at different velocities. In this study we consider two phase only, air as a primary phase and water-liquid as secondary phase. Specifying the fluid properties and the boundary conditions are straightforward. For every computational model in the study, the default fluid properties for water-liquid (water-liquid at standard conditions) and water vapor are used. Also, the boundary condition types are all

specified during the grid generation step, so the only addition needed is to specify the inlet velocity.

For all flow cases, the flow field is initialized from the inlet boundary condition. This process is necessary to provide a starting point for the evolution of the iterative solution process. In every case, after the flow is successfully initialized, the solution is iterated until one of the following two conditions is attained: convergence, divergence of the residuals. Convergence is declared if the *x*-velocity, *y*-velocity, z-velocity and continuity residuals all dropped below 0.001.

CHAPTER 5

5.RESULT AND DISCUSSION

5.1 Introduction

The major benefit of CFD analysis is its ability to compute the values of every flow parameter at each grid point in the domain studied, giving a very descriptive picture of the entire flow field. The present study can be classified to in two main parts: Firstly, the three dimensional turbulent flow over parabolic and semi-parabolic hull and then the turbulent flows with free surface over water surface bodies of revolution are simulated.

The drag coefficient is computed as

$$C_D = \frac{D}{\frac{1}{2}\rho_{ref} U_{ref}{}^2 A}$$

Where D = drag force

A = reference surface area

As explained earlier, the drag of the hull of a ship is estimated using two separate tests, by assuming that the ship drag is composed of wave drag (due to disturbances to the free surface characterize by the Froude number) and the friction drag(due to friction and characterize by the Reynolds number). Therefore in order to calculate the frictional resistance the model is approximated by the drag of the flat plate, using the same cross section of the hull and the wave drag would be equal to the total resistance of the model minus the estimated viscous resistance.

An alternative to the expensive experimental method is to use computer simulation based on methodologies of computational fluid dynamics (CFD) to analyze the flow field and predict drag for actual flow conditions. These methodologies are robust and

can provide detailed information about the flow field. Advances in computational methods and computer hardware allow efficient and accurate predictions for most flow conditions.

Application of CFD methods to complex flows, however, needs to be examined carefully and validated with experimental data.

Total drag coefficient is normally broken down into a Froude number dependent component-wave drag coefficient, C_W (residuary drag coefficient, C_R) and a Reynolds number dependent component-viscous drag coefficient , C_V (frictional drag coefficient, C_F).

The bracketed names give an alternative breakdown:

Total drag coefficient = Wave drag coefficient + Viscous drag coefficient

= Residuary drag coefficient+ frictional drag coefficient

Several approaches have been taken in order to assess the effectiveness of using CFD for the calculation of the frictional resistance.The CFD data was compared to analytically determined values of the frictional resistance of the full scale model of the ship,as well as data obtained from scaled model tests in a water towing tank.

Typically the friction drag coefficient is predicted using the ITTC 1957 Model-Ship Correlation Line or some similar formulation.

Frictional drag coefficient $C_F = \dfrac{R_F}{0.5\rho V^2 A}$,

Frictional resistance $R_F = C_f \left(\dfrac{1}{2} \rho V^2 A \right)$, where C_f is the co-efficient of friction .

Co-efficient of friction is a function of the Reynolds number and can be estimated by using the ITTC 1957 Model-Ship Correlation Line, which is produced by means of,

$$C_f = \frac{0.075}{(\log_{10} Rn - 2)^2}$$

Here, ρ is the density of the fluid

V is the velocity of the fluid and

A is the reference surface area.

Viscous drag coefficient $C_V = (1+k)\, C_F$, where k is the form factor which is counted as k=0.100 for IOWA.

Wave drag coefficient, $C_W = \frac{R_W}{0.5\rho V^2 A}$, where R_W is the force on the hull surface in the x-direction.

The viscous drag coefficient includes a form effect applied to the frictional drag coefficient .The frictional resistance arises from frictional forces set up by the flow of water along the surface of the hull, and is consequently influenced by fouling and the coatings of paints used for its prevention. The residual resistance is due to pressures developed in pushing the water aside, and arises from the form of the hull. William Froude first recognized that the residual resistance of a model could be scaled up to give the residual resistance of the full –scale ship by use of the principle of similitude developed by Newton.

5.2 Test Cases

In this section the test cases used to investigate the accuracy of the numerical resistance prediction is presented. The test cases were the Wigley hull, the Series 60 hull with turbulent –flow profile. The flow around the Wigley and the Series 60 hulls has been investigated and validated with the available experimental data.

5.2.1 Wigley Parabolic Hull

The classical test which is often considered in the naval engineering community is the simulation of the free surface flow around the Wigley-hull. Although the Wigley hull as

a test case has to some extent become obsolete for comparing the performance of numerical methods, it is sometimes still used because of its simple geometrical form, which simplifies grid generation, and also due to the large amount of experimental and computational data available for validation.

We consider a parallelepiped computational domain situated at -35 m ≤ x ≤ 65 m, -10 m ≤ y ≤ 0 m, -6.25 m ≤ z ≤ 0 m. The hull is centered at the origin and 1 m in length. Due to the symmetry of the problem with respect to the mid plane, only one half of the geometry is considered. Since both the air and water regions are modeled, the Wigley hull has been extended vertically upward 0 m to give it a rather large false free board. The vertical extent of the air zone should be large enough so that the presence of the upper boundary does not perturb the resulting solution. Standard boundary conditions (no-slip, inflow, outflow and symmetry) are considered.

5.2.1.1 Grid Independence and C_D Calculation

Two types of grids with different resolutions have been considered. The total number of cells and the total number of points along the hull(*x*), normal to the hull(*y)* and in the vertical direction (*z*) for the two grids is reported in Table 5.1. A view of the finer grid is presented in Figure 5.1.

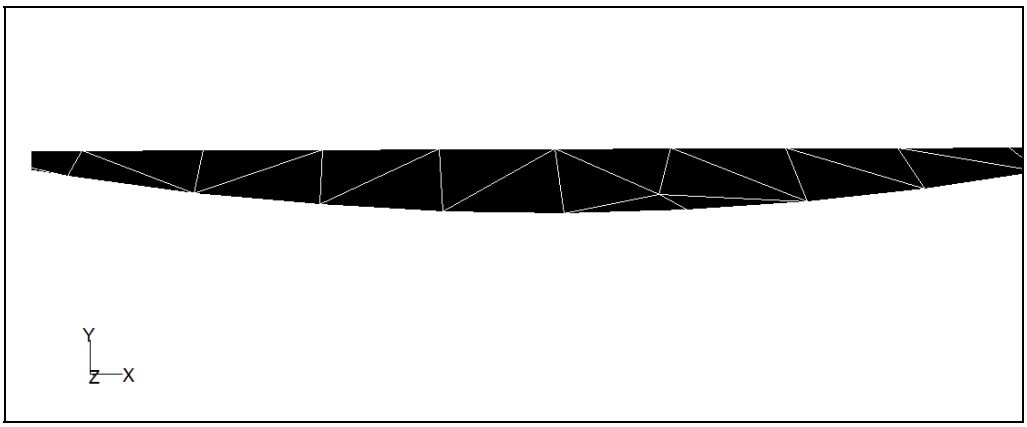

(a)

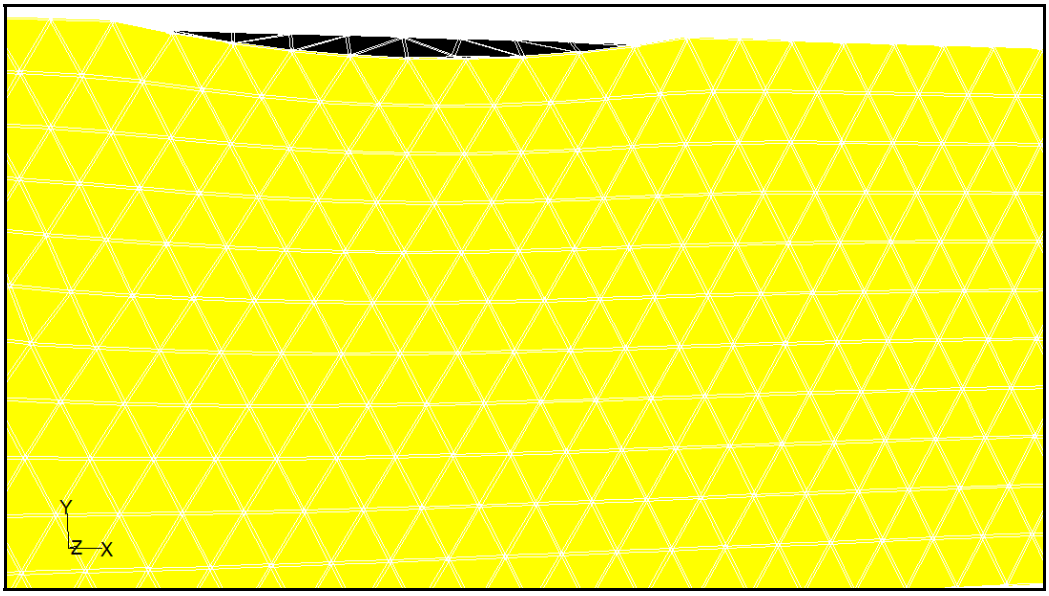

(b)

Figure 5.1: Grid of (a) Wigley Hull and (b) its Computational Domain

Table 5.1:Grid Structure of Wigley Hull

Types of Grids	Nodes	Types of Elements	Groups	Number of Elements
Structured Grid	7817	Hexahedral	8	6000
Unstructured Grid	9322	Tetrahedral	8	43887

The model considered here has a length of L=10m and advancing at different Froude numbers corresponding to Re =5.3×10^{6} to 1.48×10^{7}(both Reynolds and Froude numbers are based on L). For the RANS analysis, coarse grid for both the cases is generated. The Standard k- ε (SKE), Realizable k- ε (REA-KE), SST k-ω turbulence model and Boundary Element Method (BEM) are used.

.Table 5.2: Computed Value of C_D, C_V and C_W by Standard k-ε(SKE) Model.

Different Froude Numbers(Fn)	$C_D\times10^{-3}$	$C_V\times10^{-3}$	$C_W\times10^{-3}$
0.19	1.98	0.24	1.74
0.25	2.80	0.12	2.68
0.33	3.84	0.07	3.77
0.45	5.56	0.03	5.53
0.50	6.34	0.026	6.32

The computation of viscous (C_V), wave (C_W) and total (C_D) drag coefficient by Standard k-ε(SKE) model for the wigley hull have been showed in Table 5.2. In figure 5.2 we see that with the increasing values of *Fn*, C_D and C_W increases significantly but C_V decreases frequently. Froude number between the range [0.17, 0.5] has been taken because calculating wave making drag in these ranges, we get the approximate value.

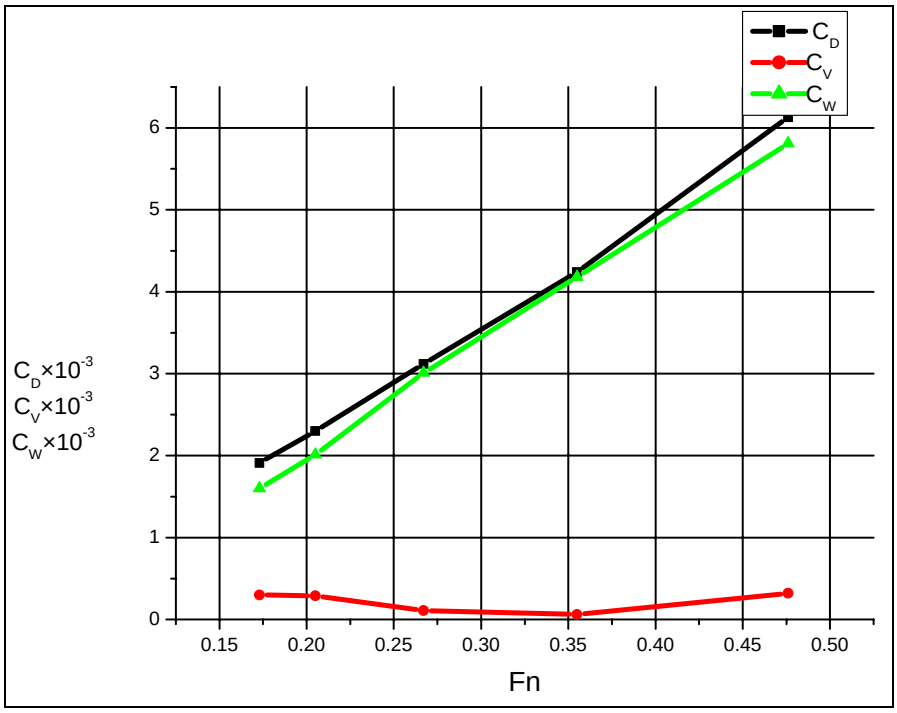

Figure 5.2: Various Drag Coefficients Vs Froude Numbers

Table 5.3: Comparison of Computed C_D by Different Turbulent Models

Different Froude Numbers(Fn)	Viscous Turbulent Models		
	Standard k- ε $C_D \times 10^{-3}$	Realizable k- ε $C_D \times 10^{-3}$	SST k-ω $C_D \times 10^{-3}$
0.19	1.98	3.08	2.30
0.25	2.80	4.29	3.10
0.33	3.84	5.61	4.20
0.45	5.56	7.75	6.02
0.50	6.34	8.67	6.86

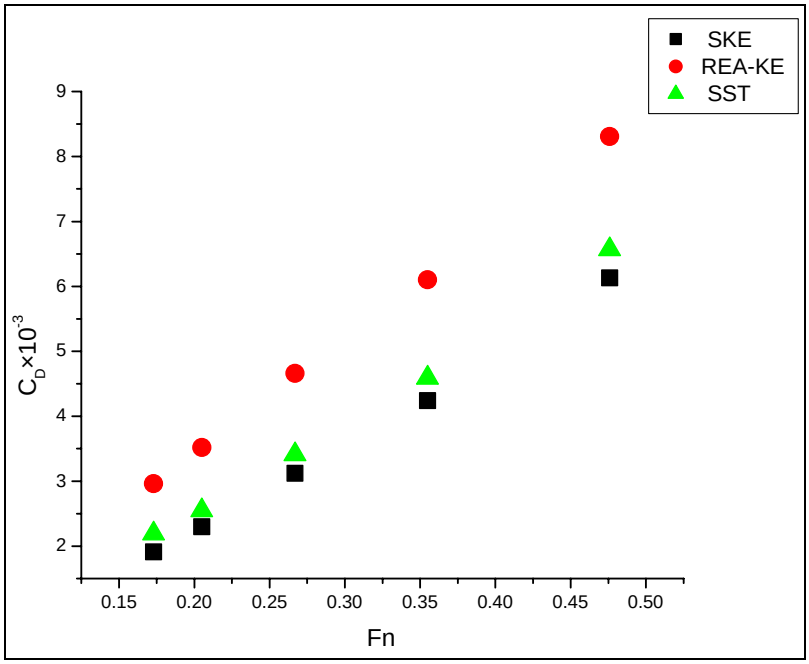

Figure 5.3: Drag Coefficients for Different Models Vs Froude Numbers

Table 5.4: Comparison of Computed C_W of Various Turbulence Models and Boundary Element (BEM) Method.

Different Froude Numbers(Fn)	Viscous Turbulent Models			BEM
	SKE	REA-KE	SST k-ω	
0.19	0.0017	0.0038	0.0020	0.37
0.25	0.0027	0.0041	0.0029	0.80
0.33	0.0037	0.0055	0.0041	0.82
0.45	0.0055	0.0077	0.0059	4.16
0.50	0.0063	0.0086	0.0068	

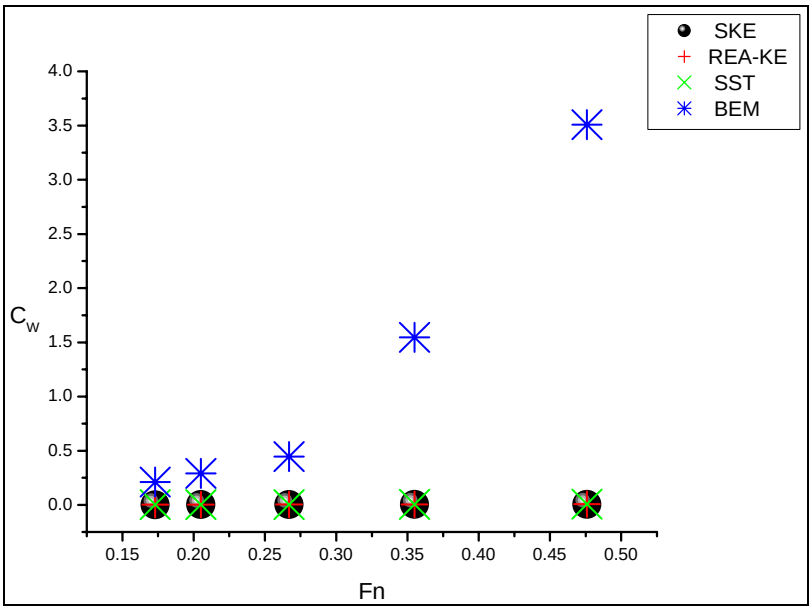

Figure 5.4: Wave Drag Coefficient Vs Froude Numbers

5.2.1.2 Comparison with other Researchers

The model considered here has a length L=1m and advancing at Fn=0.267 corresponding to Re= 8.3×10^6 (both Reynolds and Froude numbers are based on L).Computed drag coefficients with turbulence k- ε model is compared with the results of Azcueta (2005) ,Pranzitelli *et al.*(2011) and Mucientes(2010) for the same Froude number Fn=0.267 corresponding to Reynolds number Re= 5.95×10^6 , 5.94×10^6 and 6.66×10^6 respectively. In those cases the model considered there had a length L=4m.

Table 5.5: Comparison of Computed C_D for Wigley hull

	$C_D\times10^{-3}$
Present	4.66
Azcueta(2005)	4.39
Mucientes(2010)	4.15
Pranzitelli *et al.*(2011)	4.20

5.2.1.3 Comparison with experimental result

A Reynolds number Re= 5.95×10^{6} and a Froude number Fn=0.267 as in the model test (4 m model) of the Ship Research Institute (SRI), *N.N.(1983)* was set. Analogous results are obtained for the coefficient of total drag co-efficient C_D, (Table 5.6) where the difference $\Delta C_D = (C_{D,cfd}-C_{D,exp})/C_{D,exp,}$ between numerical and experimental results is greater than 12% in all of the cases. The present result shows a good agreement on the experimental results from Ship Research Institute (SRI), Anon (1983). As it can be noticed from results presented here, good free surface and C_D calculations can be obtained using one of the two types of grids reducing significantly in this manner CPU time without excessive loss of accuracy.

Table 5.6: Comparison with the Experimental Result

	$C_D\times10^{-3}$	$(C_{D,cfd}- C_{D,exp})/C_{D,exp,}$
Present	4.66	12%
SRI, Anon	4.16	

The drag coefficients as a function of different Reynolds numbers are compared with experimental and other numerical results in Figure 5.5 and in Tables 5.5 and 5.6.In most cases, the computed results show better agreement with experimental data compared to other predicted values.

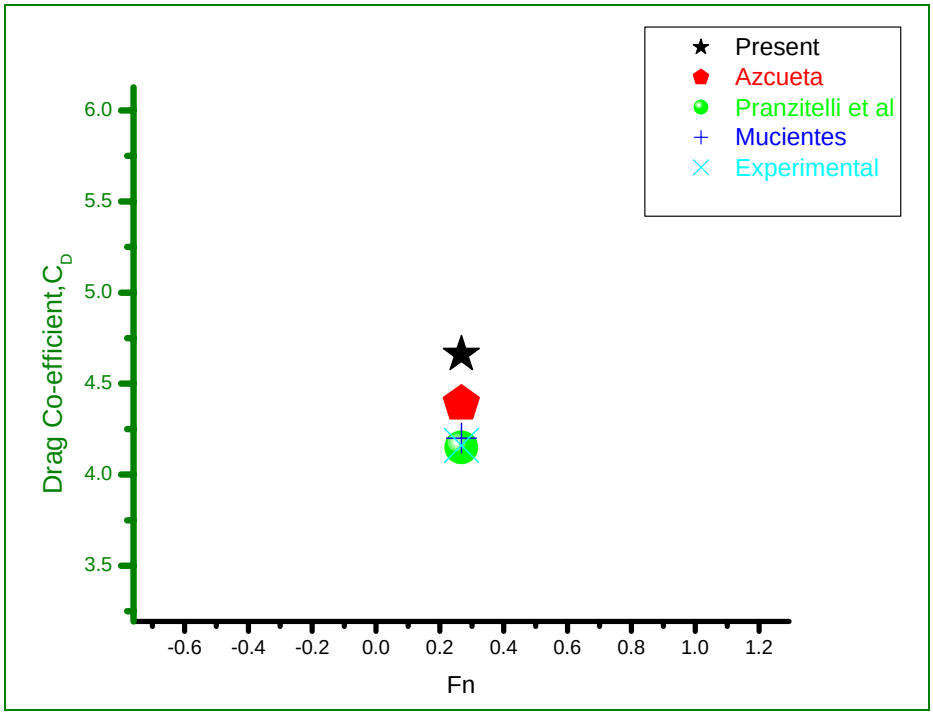

Figure5.5: Drag Coefficient Vs Froude Number

The present result has been compared with other nu merical and experimental results for a single Fr = 0.267 corresponding to Re = 8.3×10^6. We can also compare the total drag co-efficient(C_D), viscous drag co-efficient(C_V) and also wave drag coefficient(C_V) with the computed results of Sangseon(1983) and Olivieri *et.al.*(2001) .

Table 5.7: Comparison with Other Numerical Result

Fn	Present			Sangseon			Olivieri		
	$C_D\times10^{-3}$	$C_V\times10^{-3}$	$C_W\times10^{-3}$	$C_D\times10^{-3}$	$C_V\times10^{-3}$	$C_W\times10^{-3}$	$C_D\times10^{-3}$	$C_V\times10^{-3}$	$C_W\times10^{-3}$
0.173	2.96	2.36	0.60	4.22	4.0	.22	-	-	-
0.205	3.52	3.20	0.32	4.32	3.89	.41	4.25	3.38	0.86
0.267	4.66	4.17	0.49	4.51	3.72	.78	4.35	3.20	1.15
0.355	6.10	5.19	0.91	5.00	3.6	1.4	5.12	3.08	2.04

5.2.2 Series 60 Hull

The ship model used for this study is a series 60 hull with block coefficient C_B of 0.6, which is a single-propeller merchant type ship and is a standard for ship hydrodynamics

research, and widely used in ITTC research program. The series 60 hull form is largely used to design ships and it has been the subject of several numerical and experimental studies. Extensive towing tank tests were carried out at Iowa Institute of Hydraulic Research (IIHR) (Toda *et al* .1992).

We consider a parallelepiped computational domain situated at -50 m $\leq$ x $\leq$ 50 m, -13.3m $\leq$ y $\leq$ 0 m, -5.33 m $\leq$ z $\leq$ 0 m. The hull is centered at the origin and 1 m in length. Like the Wigley hull due to the symmetry of the problem with respect to the mid plane, only one half of the geometry is considered. Standard boundary conditions (no-slip, inflow, outflow and symmetry) are considered.

5.2.2.1 Grid Independence and C_D Calculation

In this section numerical simulations has been carried out of the Series 60 hull model of L=1.00 m for a direct comparison with the experimental tests cited. Five types of Froude numbers for two types of grids has been considered. The total number of cells and the total number of points along the three directions for the two grids is reported in table 5.8. A view of the finer grid is presented in figure 5.6.

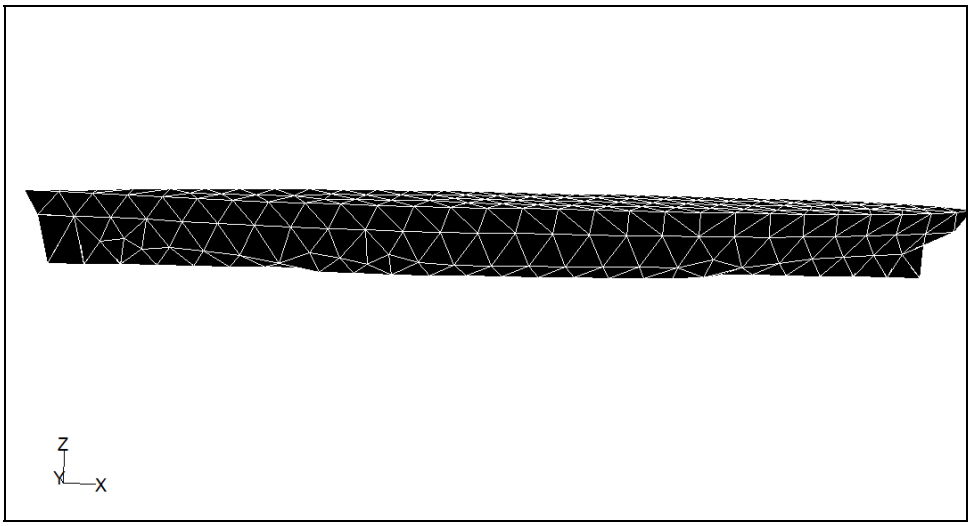

(a)

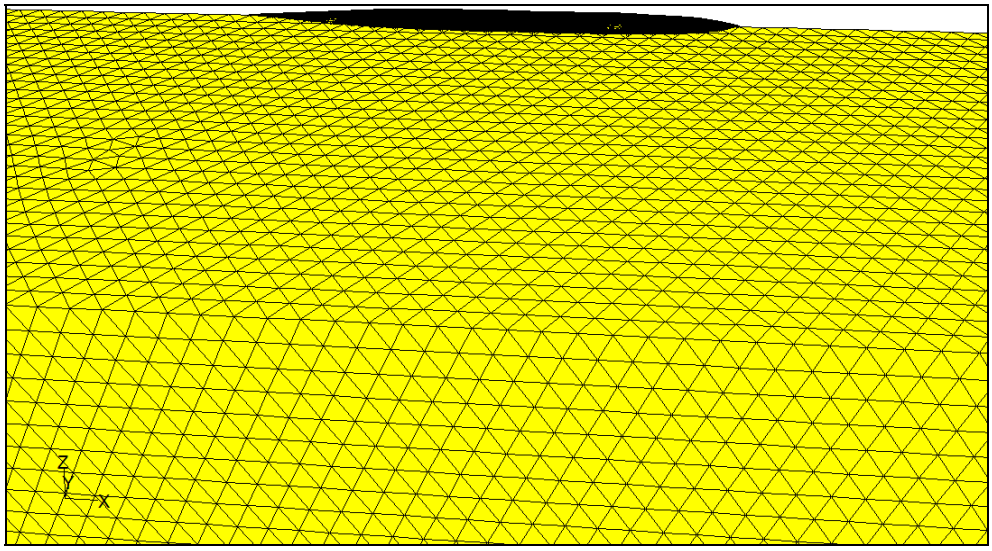

(b)

Figure 5.6: Grid of (a) Series 60 hull
and (b) its Computational Domain

Table 5.8: Grid Structure of Series 60 Hull

Types of Grids	Nodes	Types of Elements	Groups	Number of Elements
Structured Grid	67705	Hexahedral	8	59788
Unstructured Grid	76236	Tetrahedral	8	402887

Like the Wigley hull, the model considered here has a length of L=10m and advancing at different Froude numbers corresponding to Re $=5.3\times10^{6}$ to 1.48×10^{7}(both Reynolds and Froude numbers are based on L). For the RANS analysis, coarse grid for both the cases is generated. The Standard k- ε (SKE), and Boundary Element Method(BEM) are used to compare the computed result with other numerical and experimental results.

Table 5.9: Computed Value of C_D, C_V and C_W by Standard k-ε (SKE) Model.

Different Froude Numbers(Fn)	$C_D \times 10^{-3}$	$C_V \times 10^{-3}$	$C_W \times 10^{-3}$
0.19	1.98	0.19	1.79
0.25	3.19	0.09	3.10
0.33	7.21	0.05	7.16
0.45	11.43	0.03	11.40
0.50	19.18	0.02	19.16

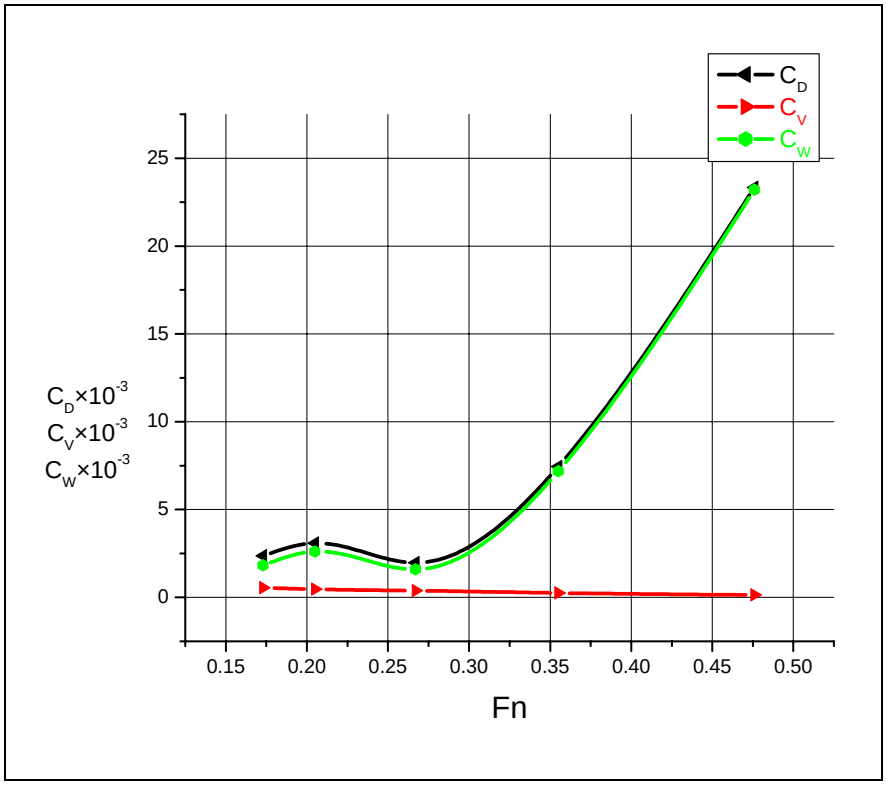

Figure 5.7: Various Drag Coefficients Vs Froude Numbers.

The computation of viscous (C_v), wave (C_w) and total (C_D) drag coefficient by standard k-ε model for the Series 60 hull have been showed in Table 5.8. In Figure 5.7 we see that with the increasing values of Fn, C_D and C_W increases significantly but C_V decreases slightly.

Both from the Figure 5.4 and 5.9 it has been observed that comparing the values of total drag co-efficient of different turbulent models with the BEM method, results shows a well agreement for Froude numbers in the range of [0.173,0.267]. Whenever the range exceeds 0.3 there occurrences a large variation between the computed result and other numerical and experimental results.

Table 5.10: Comparison of Computed C_D by Various Turbulent Models

Different Froude Numbers(Fn)	Viscous Turbulent Models		
	Standard k- ε $C_D \times 10^{-3}$	Realizable k- ε $C_D \times 10^{-3}$	SST k-ω $C_D \times 10^{-3}$
0.19	1.98	2.65	2.17
0.25	3.19	3.64	3.19
0.33	7.21	8.09	10.30
0.45	11.43	23.50	80.28
0.50	19.18	76.35	96.82

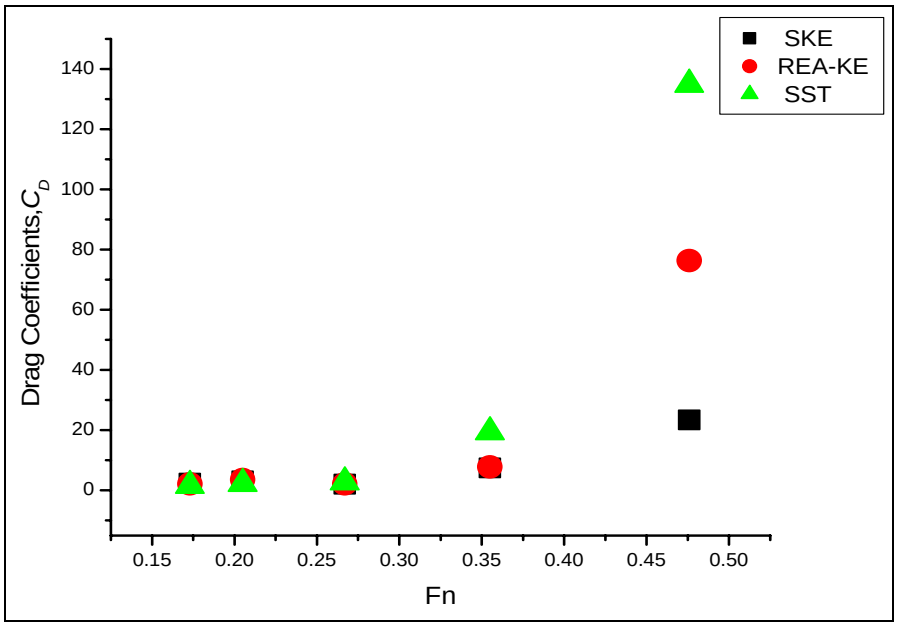

Figure 5.8: Drag Coefficients of Different Models Vs Froude Numbers.

Table 5.11: Comparison of Computed C_W of Various Turbulence Models and Boundary Element (BEM) Method.

Different Froude Numbers(Fn)	Viscous Turbulent Models			BEM
	SKE	REA-KE	SST k-ω	
0.19	0.0018	0.0025	0.0019	0.16
0.25	0.0031	0.0035	0.0031	0.24
0.33	0.0071	0.0080	0.0102	1.24
0.45	0.011	0.0235	0.0803	13.84
0.50	0.0192	0.0763	0.0968	

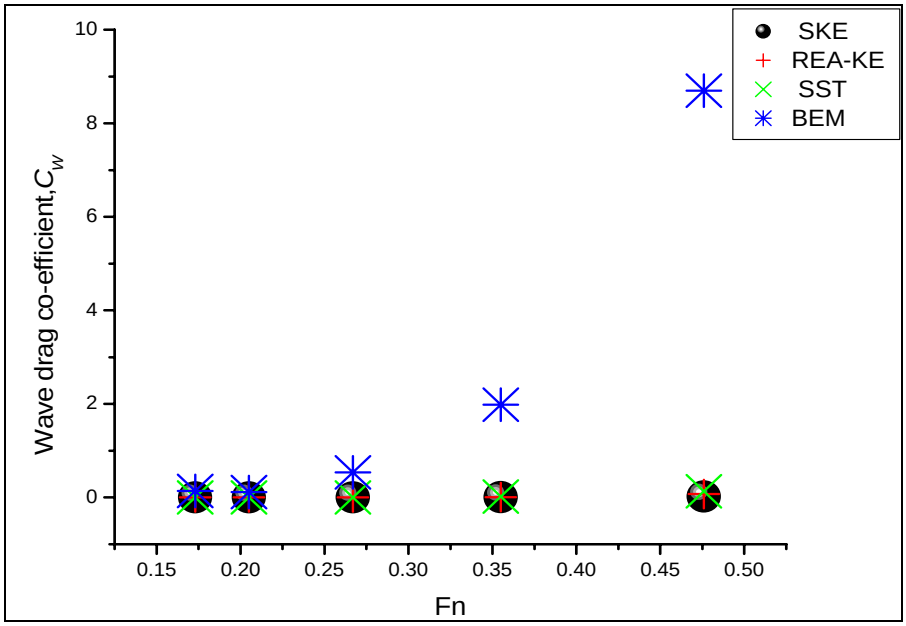

Figure 5.9: Wave Drag Coefficient Vs Froude Numbers.

5.2.2.2 Comparison with other Researchers

The model considered here has a length L=1m and advancing at Fn=0.316 corresponding to Re = 9.8×10^6 (both Reynolds and Froude numbers are based on L).Computed drag coefficients with turbulence k- ε model is compared with the results of Azcueta (2005) and Pranzitelli *et al.*(2011) for the same Froude number Fn=0.316 corresponding to Reynolds number Re = 4.0×10^6 and 5.24×10^6 respectively. While

comparing the result with the second case the model considered there had a length L=3.048m.

Table 5.12: Comparison of Computed C_D for Series 60 hull

	$C_D \times 10^{-3}$
Present	5.72
Azcueta (2005)	5.10
Pranzitelli *et al.*(2011)	5.41

5.2.2.3 Comparison with experimental result

Extensive towing tank tests were carried out at Iowa Institute of Hydraulic Research (IIHR)(Toda *et al.*1992) and results are partially available on the web in digital form. IIHR Towing tank is 100m long and 3m wide, test was carried out on a model 3.048m long at Froude numbers Fn = 0.316 corresponding to Re = 4.0×10^6.

In this section, numerical simulations were carried out of the Series 60 hull model of L=1m for a direct comparison with the experimental tests cited. Froude number considered is 0.316, corresponding to Re = 9.8×10^6.

Table 5.13: Comparison with the Experimental Result

	$C_D \times 10^{-3}$	$(C_{D,cfd}- C_{D,exp})/C_{D,exp,}$
Present	5.72	4.02%
Toda *et al.*(1992)	5.96	

Analogous results are obtained for the coefficient of total drag co-efficient CD,(Table 5.11)where the difference $\Delta C_D = (C_{D,cfd}-C_{D,exp})/C_{D,exp}$, between numerical and experimental results is less than 4.02% in all of the cases. Table 5.11 shows a remarkable variation in the C_D calculation that now falls in the range of uncertainty of the experimental tests both for the k- ε model and BEM method.

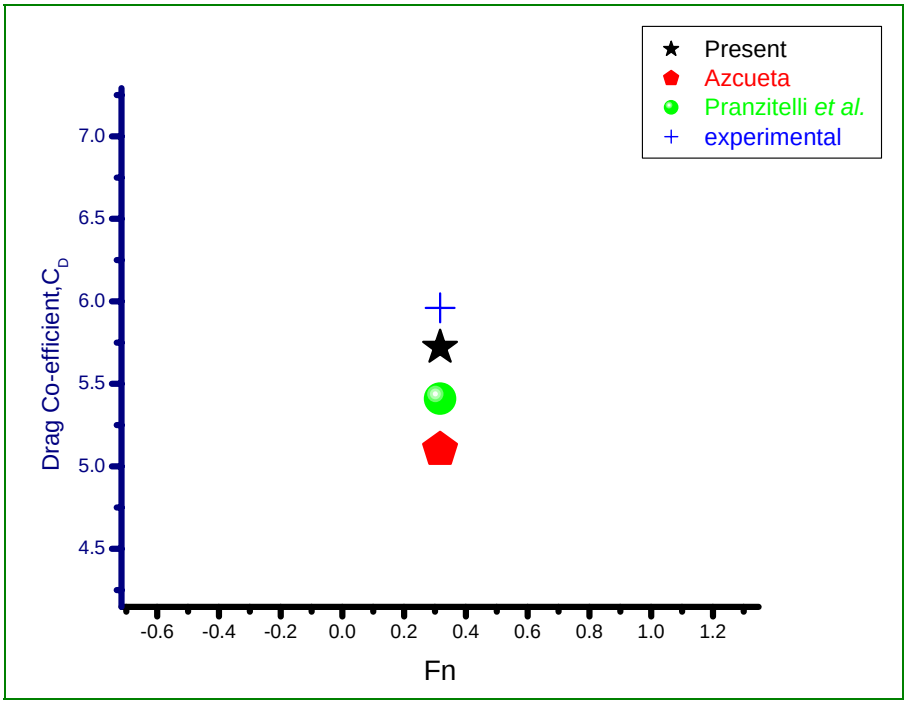

Figure5.10: Drag Coefficient Vs Froude Number

The drag coefficients as a function of different Froude numbers are compared with experimental and other numerical results in Figures 5.10 and in tables 5.12 and 5.13.In most cases, the computed results show better agreement with experimental data compared to other predicted values.

5.3 Effect of Turbulence Model

The turbulent flow structure in the proximity of the free-surface can be much more complex than the turbulent flow structure of single phase flows. Existing turbulence models, which have been mainly proposed for single phase flows may not adequately represent the turbulence structure at the free surface(Senocak and laccarino 2005).The creation of a turbulence model able to simulate correctly turbulent free- surface flows and the interaction between free- surface and turbulent boundary layer represents a challenge in CFD. Among the turbulence models available in FLUENT, the Realizable k- ε and the SST k-ω models are compared with the Standard k- ε model to investigate possible differences in resistance predictions.

5.4 Improvement of the Convergence

Using VOF model it is easy to encounter convergence problems in presence of a high difference between densities of fluids considered as equations become stiffer. This is the case of air and water where $\frac{\rho_w}{\rho_a} \approx 800$ .Convergence can be improved by altering the ratios between densities and viscosities of fluids; a value of 100 for $\frac{\rho_w}{\rho_a}$ and $\frac{\mu_w}{\mu_a}$ can be used without committing remarkable errors. As one can see in Figure 5.5 residuals, become more regular and reach lower values than in the real case. The effects on C_D are minimal and mainly due to the major forces acting on the surfaces exposed to air. However, this problem can be relevant only if superstructures are well defined and in the pre-design phase this error can be easily corrected or avoided by eliminating these surfaces from C_D calculation.

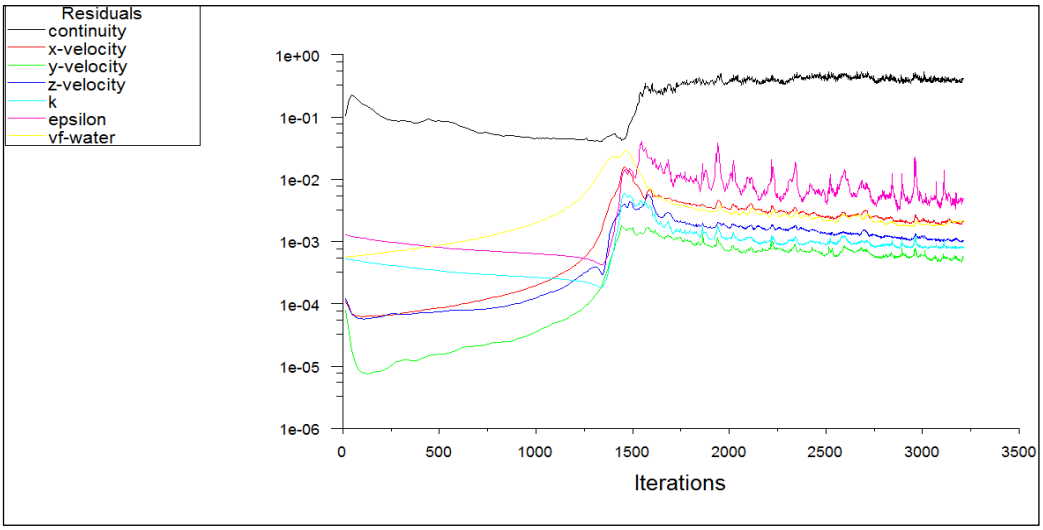

Figure 5.11: Residual History of Model Wigley for Fn=0.476

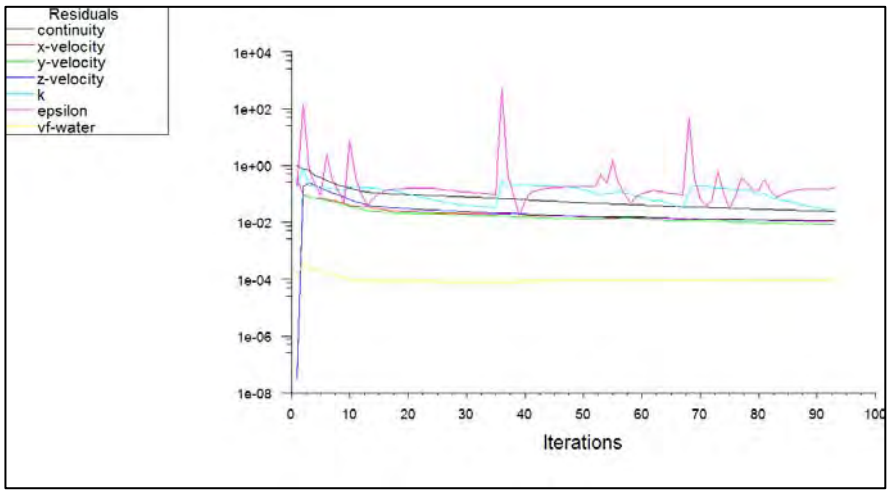

Figure 5.12: Residual History of Model Series 60 for Fn=0.476

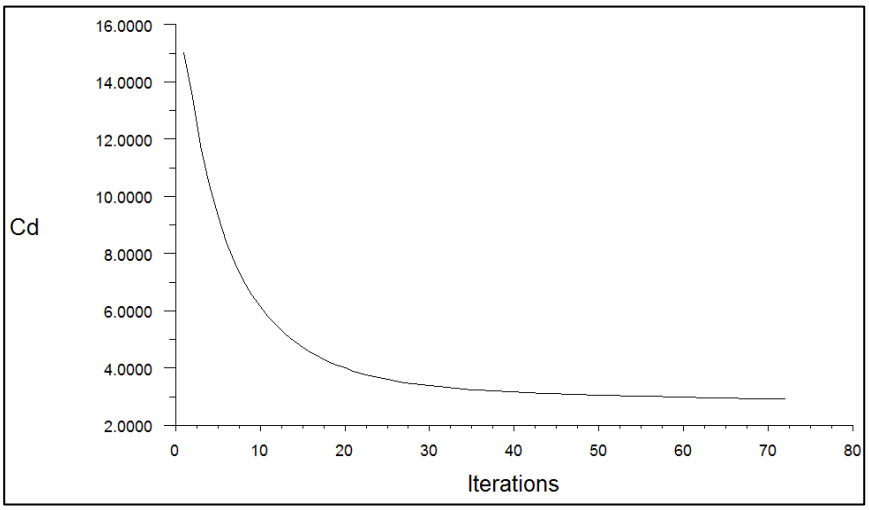

Figure 5.13: Drag Convergence History of Model Wigley

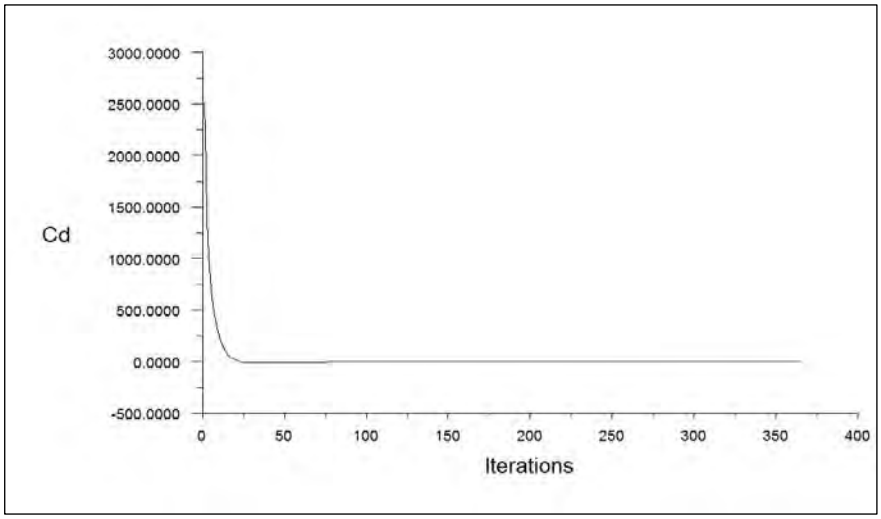

Figure 5.14: Drag Convergence History of Model Series 60

5.5 Numerical Scheme

In this simulation, the commercial software package FLUENT 6.3.26 is used. It is a two/three dimensional structure mesh code that solves a set of time independent Reynolds-averaged Navier Stokes equations(RANS) in a conservative form. The numerical model uses an implicit finite volume method associated with multiphase model. An implicit steady-state cell based solution procedure is used to solve the equations. Free surface calculations are performed with the VOF model which is employed to handle the free –surface wave flow around a surface-piercing structure. In the VOF method a single set of momentum equations is shared by the fluids and the volume fraction of each of the fluids in every computational cell is tracked throught the domain. Central differencing scheme, while generally able to retain the sharpness of the interface, are unbounded and often give unphysical results. To overcome these deficiencies, a modified version of the HRIC scheme that consists of a non-linear blend of upwind and downwind differencing is employed. The second order upwind scheme is used for convection and diffusion terms. The velocity-pressure coupling is employed and the overall solution procedure is based on the SIMPLE segregated algorithm. The PRESTO scheme is used for pressure calculation. Note that in the present study, all flows and phases of fluids are considered to be incompressible. The VOF formulation relies on the fact that two or more fluids/phases are not interpenetrating or mixing. For each additional phase, a new variable that in the volume fraction of the corresponding phase is introduced. The relaxation factors are typically set to 0.2.The y+ values for the wall adjacent cells over the hull is in the range $80.0 \leq y+ \leq 100.0$, which is comfortably within the guidelines for the use of the wall function approach.

Initial convergence of the simulation is found to be considerably enhanced by paying careful attention to the initialization procedure. The primary phase should always be set the lower density fluid, which is in this case is air. The specified operation density should be set to that of the primary phase and the reference pressure location should be set to a region which will always contain the primary phase .It is also found helpful to initialize the entire water domain with the correct hydrostatic pressure profile and to initialize both the water and air domain to the same velocity.

5.4 Free Surface Generation

It is instructive to visualize the free surface wave generated due to the motion of the hull. This was created using a derived part within FLUENT. The input part is selected to be the complete body, not just the hull itself, and the volume fraction of water at the scaler at 0.5. The free surface is considered at 0.5 volume fraction in each cell. The later means the iso- surface will be created at half of the domain (in z direction) and it will extend throught the entire dimension of it. Thus, since the geometry was generated in the middle of the domain, the generated iso- surface represents the water surface.

5.5 Simulation Results with a Tetrahedral Mesh

One of the advantages of the Fluent code for simulations of naval vessels is its ability to solve the RANS equations on either a structured hexahedral mesh or an unstructured hybrid mesh consisting of tetrahedral cells. It is generally accepted that hexahedral meshes provide more accurate simulation results but the one disadvantages of this approach in the time required to construct the mesh. Especially when using the Gambit Software package to create the mesh, the use of an unstructured hybrid mesh will result in considerable time savings. In our study we have used an unstructured hybrid mesh to gain some experience with this technique in anticipation of the need to consider more complicated geometries in future naval applications.

Both for the two models a half domain grid has been used but the size of the domain is smaller than that used with the unstructured mesh. The undisturbed sea surface is located on the z = 0 plane. A surface mesh for the hull is considered from triangular elements. A Gambit curvature size function is used to ensure smooth growth of the mesh size in highly curved regions of the hull. The hull top, undisturbed sea surface and symmetry plane have been meshed with triangular elements. Prism layers are then grown from the hull surface, the symmetry plane and the plane representing the undisturbed sea surface. A tetrahedral volume mesh is then from each of these surfaces, again using appropriate size functions to ensure a uniform rate of change in cell size, and the resulting mesh has 43887 cells and 52835 cells in the case of Wigley and Series 60 respectively.

In the case of Wigely hull one of the reference surfaces has been created in terms of the contours of z co-ordinate at z = -0.051 and compared the contours of pressure co-efficient, velocity magnitude of the hull with free surface and symmetric top of the computational domain for different Froude numbers which are shown in figures 5.15 - 5.25.Also in the case of series 60 hull another reference surface has been created in terms of the contours of z co-ordinate at z = -0.54 and compared the contours of pressure co-efficient, velocity magnitude of the hull with free surface of the computational domain for different Froude numbers which are shown in figures 5.26-5.34.

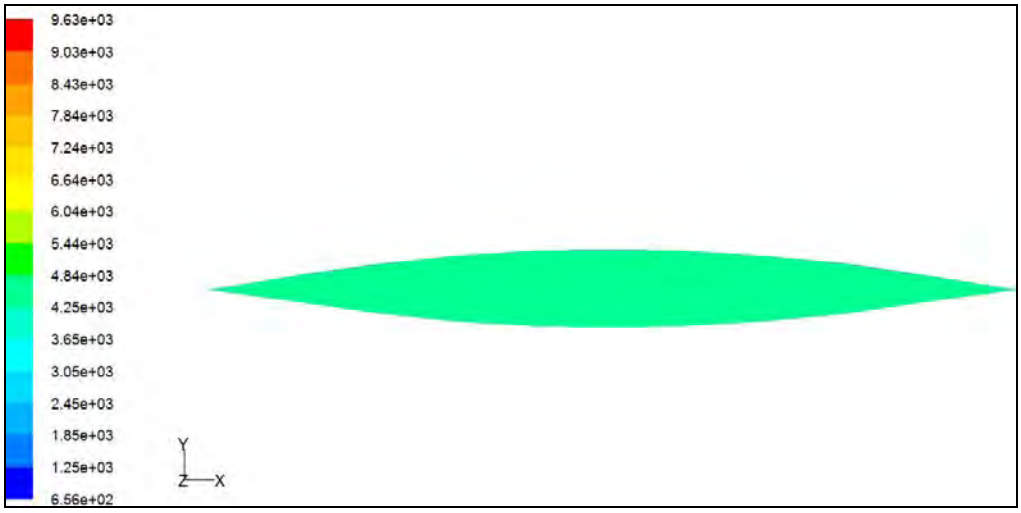
9.63e+03
9.03e+03
8.43e+03
7.84e+03
7.24e+03
6.64e+03
6.04e+03
5.44e+03
4.84e+03
4.25e+03
3.65e+03
3.05e+03
2.45e+03
1.85e+03
1.25e+03
6.56e+02
Y
Z
X

(a)

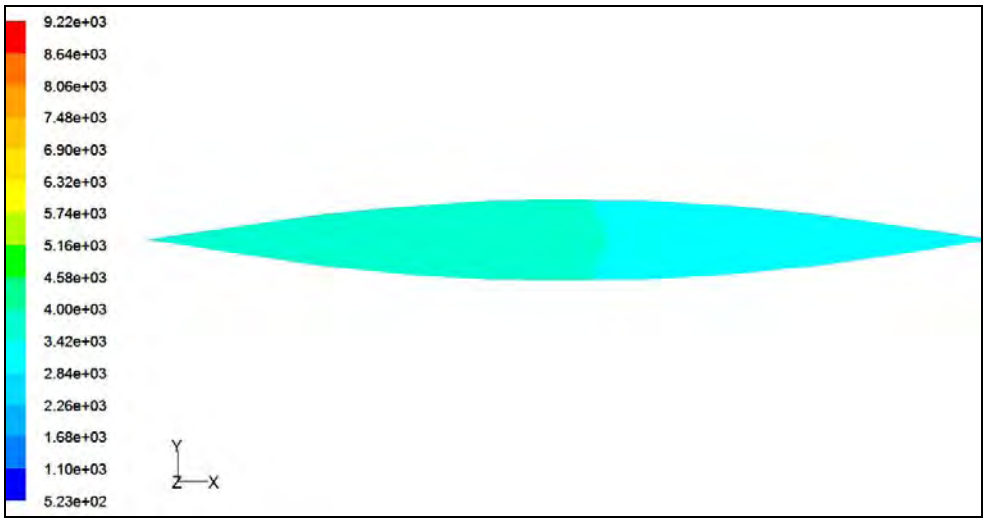
9.22e+03
8.64e+03
8.06e+03
7.48e+03
6.90e+03
6.32e+03
5.74e+03
5.16e+03
4.58e+03
4.00e+03
3.42e+03
2.84e+03
2.26e+03
1.68e+03
1.10e+03
5.23e+02
Y
Z
X

(b

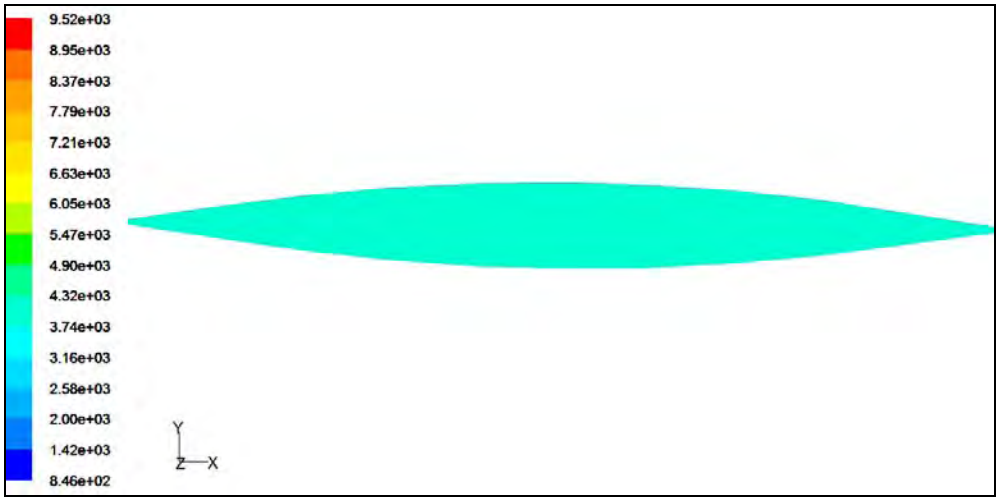
9.52e+03
8.95e+03
8.37e+03
7.79e+03
7.21e+03
6.63e+03
6.05e+03
5.47e+03
4.90e+03
4.32e+03
3.74e+03
3.16e+03
2.58e+03
2.00e+03
1.42e+03
8.46e+02
Y
Z
X

(c)

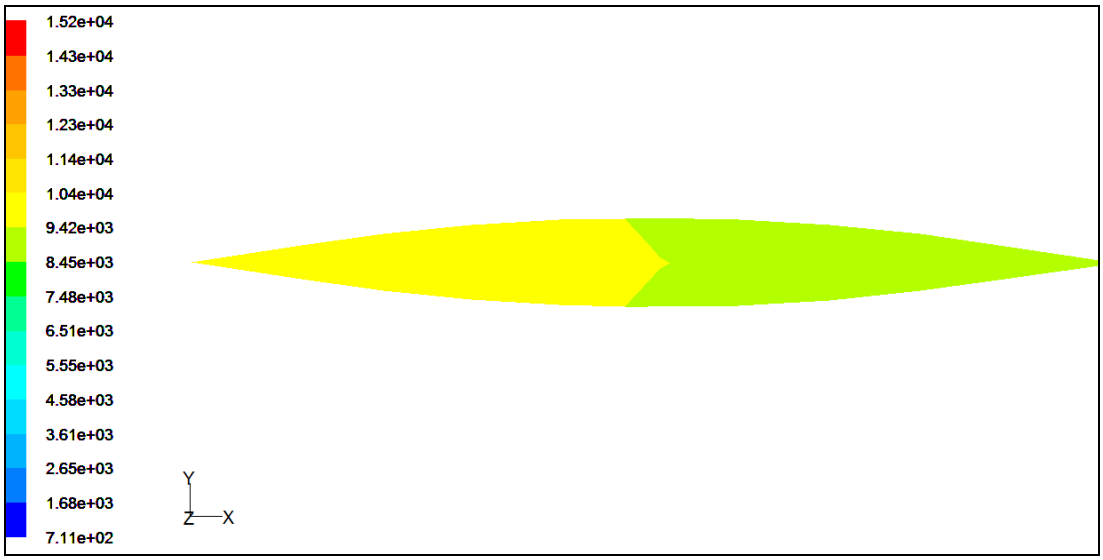

(d)

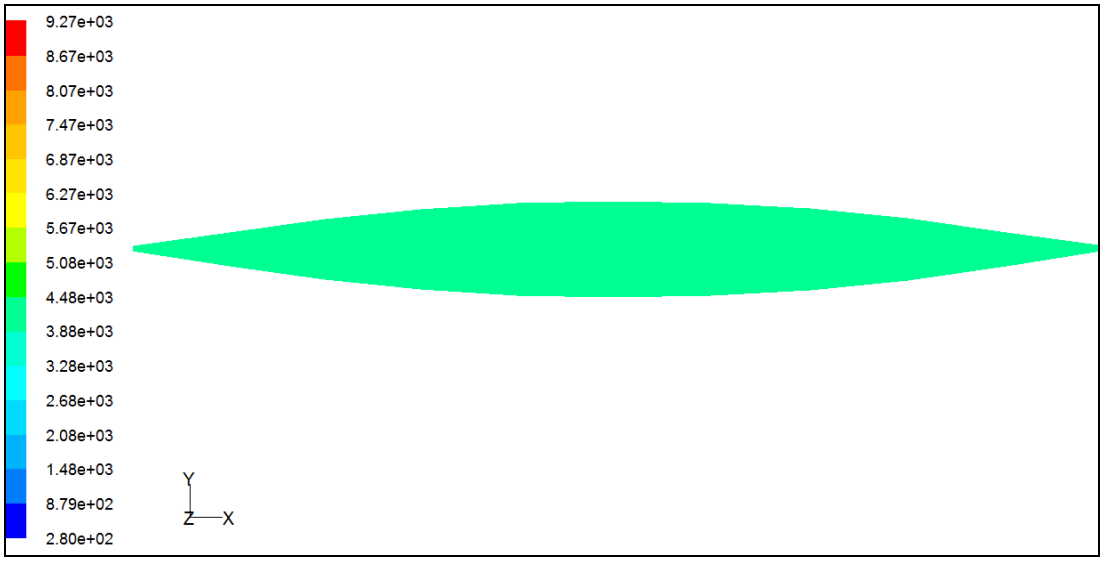

(e)

Figures 5.15: Contours of Pressure Coefficient of Wigley Hull for a)Fn = 0.173,b)Fn = 0.205, c) Fn = 0.267, d) Fn = 0.355 and e) Fn = 0.476.

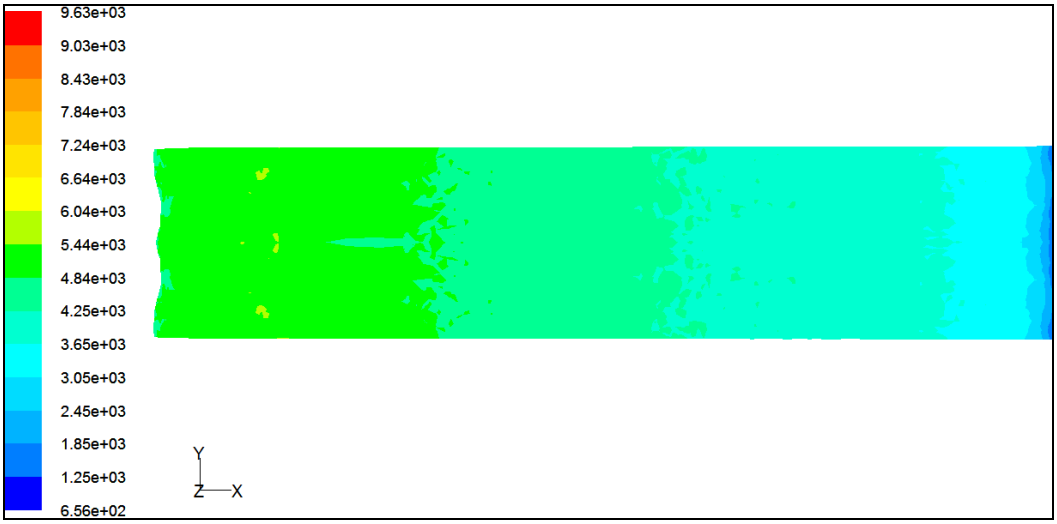
9.63e+03
9.03e+03
8.43e+03
7.84e+03
7.24e+03
6.64e+03
6.04e+03
5.44e+03
4.84e+03
4.25e+03
3.65e+03
3.05e+03
2.45e+03
1.85e+03
1.25e+03
6.56e+02
Y
Z
X

(a)

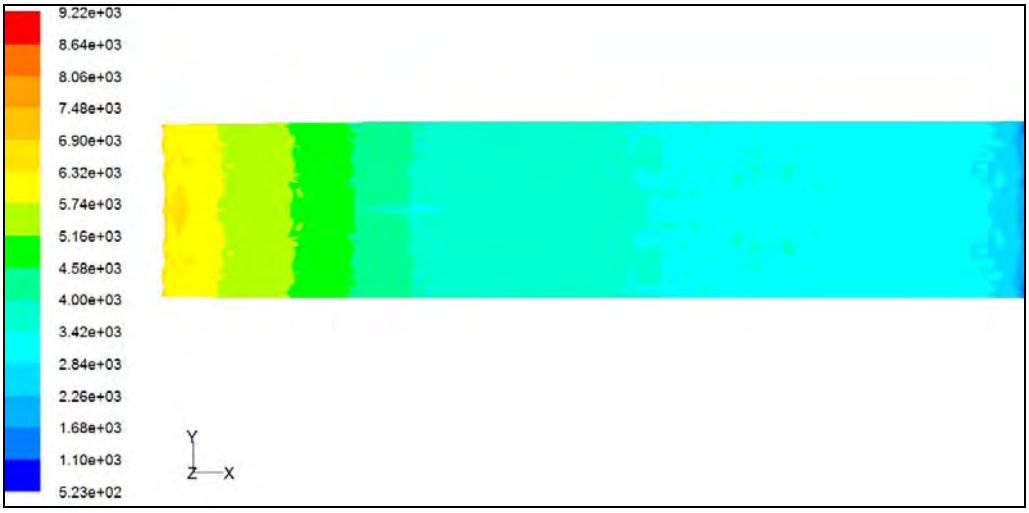
9.22e+03
8.64e+03
8.06e+03
7.48e+03
6.90e+03
6.32e+03
5.74e+03
5.16e+03
4.58e+03
4.00e+03
3.42e+03
2.84e+03
2.26e+03
1.68e+03
1.10e+03
5.23e+02
Y
Z
X

(b)

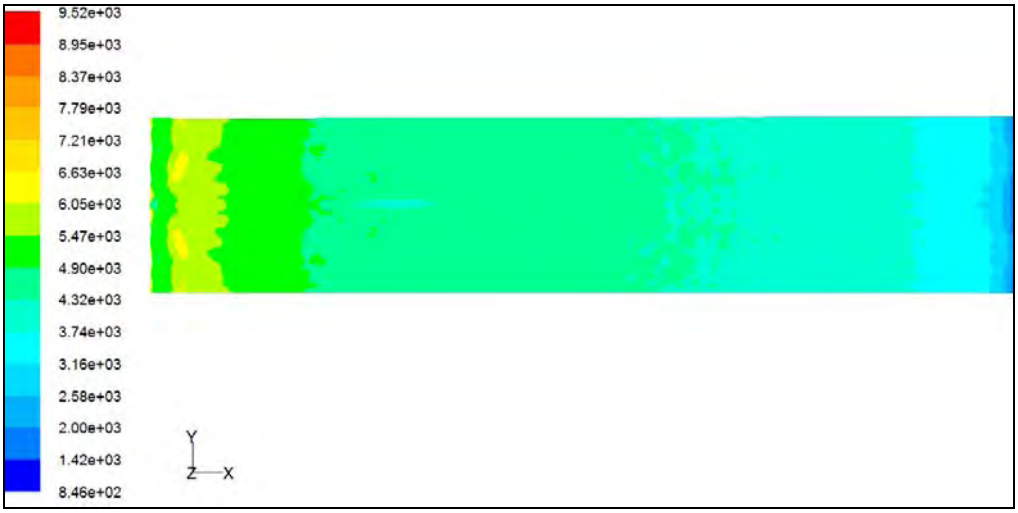
9.52e+03
8.95e+03
8.37e+03
7.79e+03
7.21e+03
6.63e+03
6.05e+03
5.47e+03
4.90e+03
4.32e+03
3.74e+03
3.16e+03
2.58e+03
2.00e+03
1.42e+03
8.46e+02
Y
Z
X

(c)

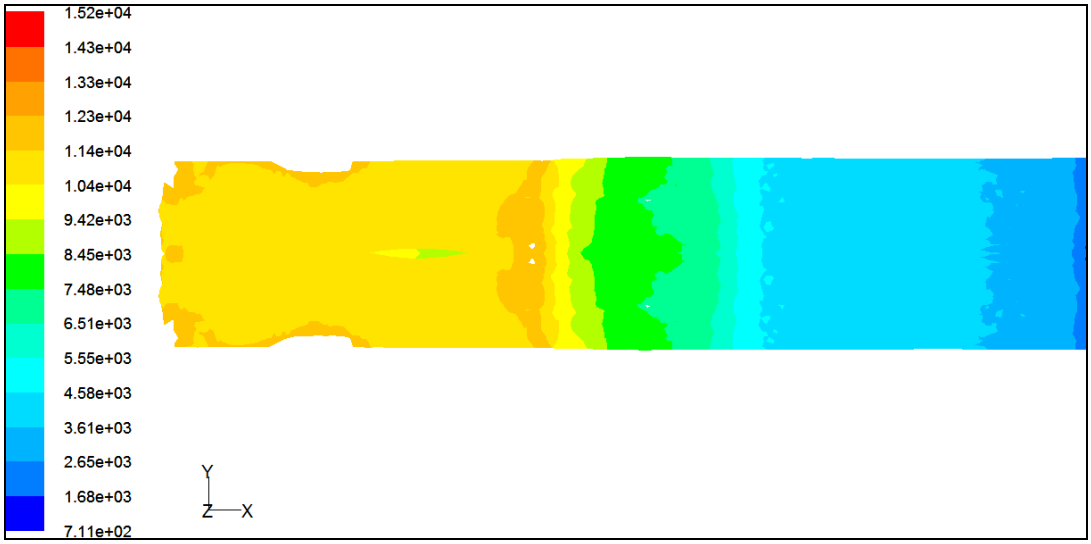

(d)

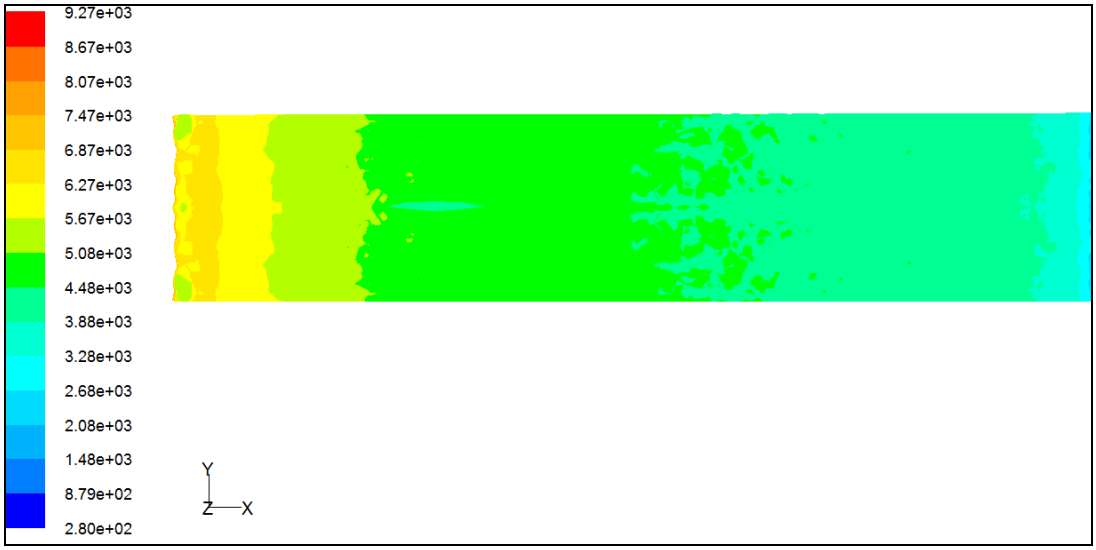

(e)

Figures 5.16: Contours of Pressure Coefficient of Wigley Hull and its Free Surface for a) Fn = 0.173,b)Fn = 0.205, c) Fn = 0.267,d) Fn = 0.355 and e) Fn = 0.476

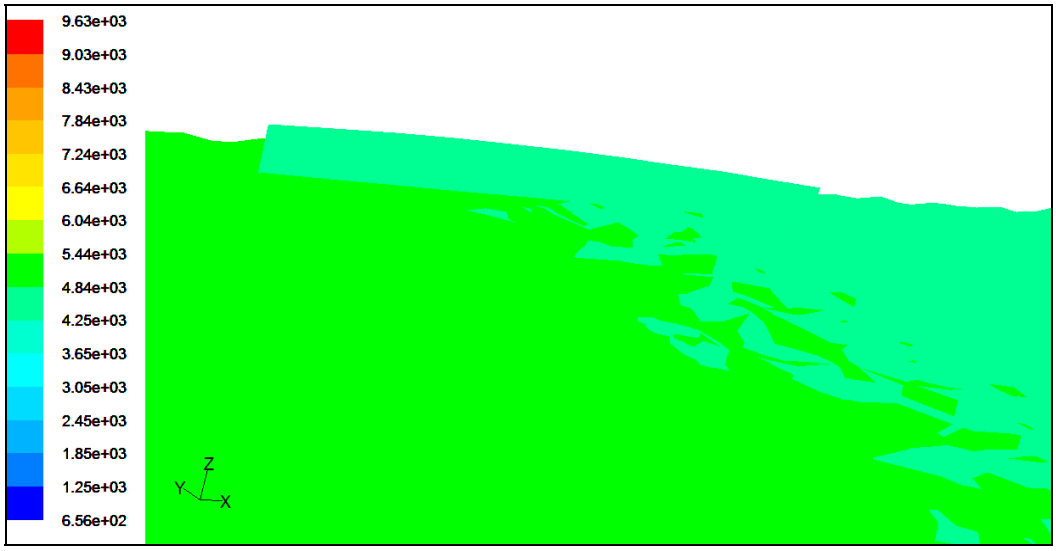
9.63e+03
9.03e+03
8.43e+03
7.84e+03
7.24e+03
6.64e+03
6.04e+03
5.44e+03
4.84e+03
4.25e+03
3.65e+03
3.05e+03
2.45e+03
1.85e+03
1.25e+03
6.56e+02
Z
Y
X

(a)

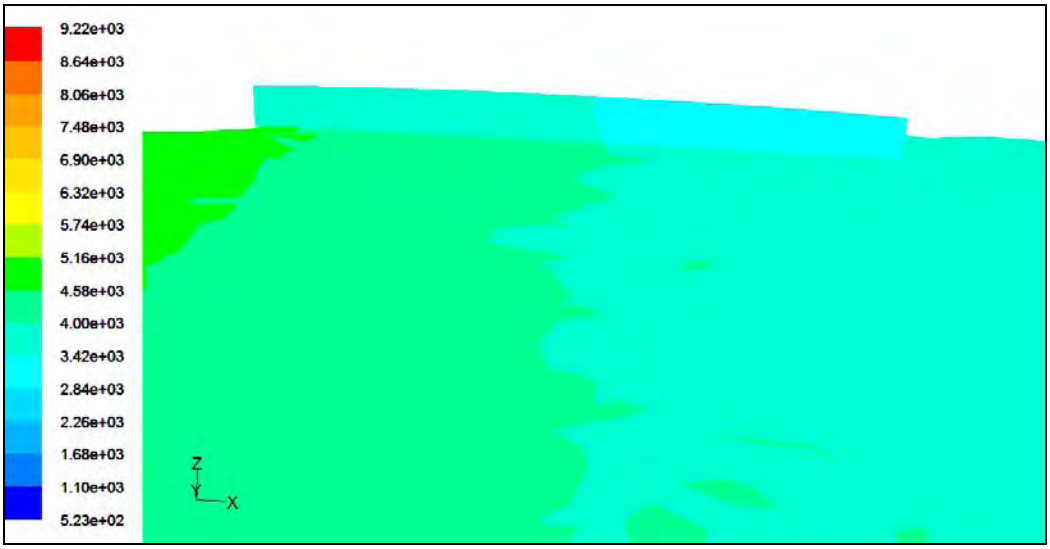
9.22e+03
8.64e+03
8.06e+03
7.48e+03
6.90e+03
6.32e+03
5.74e+03
5.16e+03
4.58e+03
4.00e+03
3.42e+03
2.84e+03
2.26e+03
1.68e+03
1.10e+03
5.23e+02
Z
Y
X

(b)

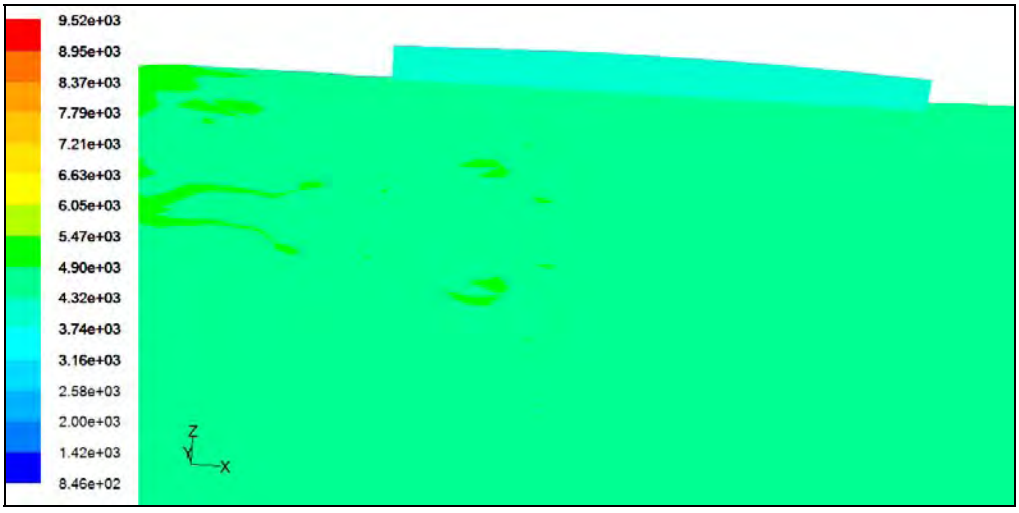
9.52e+03
8.95e+03
8.37e+03
7.79e+03
7.21e+03
6.63e+03
6.05e+03
5.47e+03
4.90e+03
4.32e+03
3.74e+03
3.16e+03
2.58e+03
2.00e+03
1.42e+03
8.46e+02
Z
Y
X

(c)

(d)

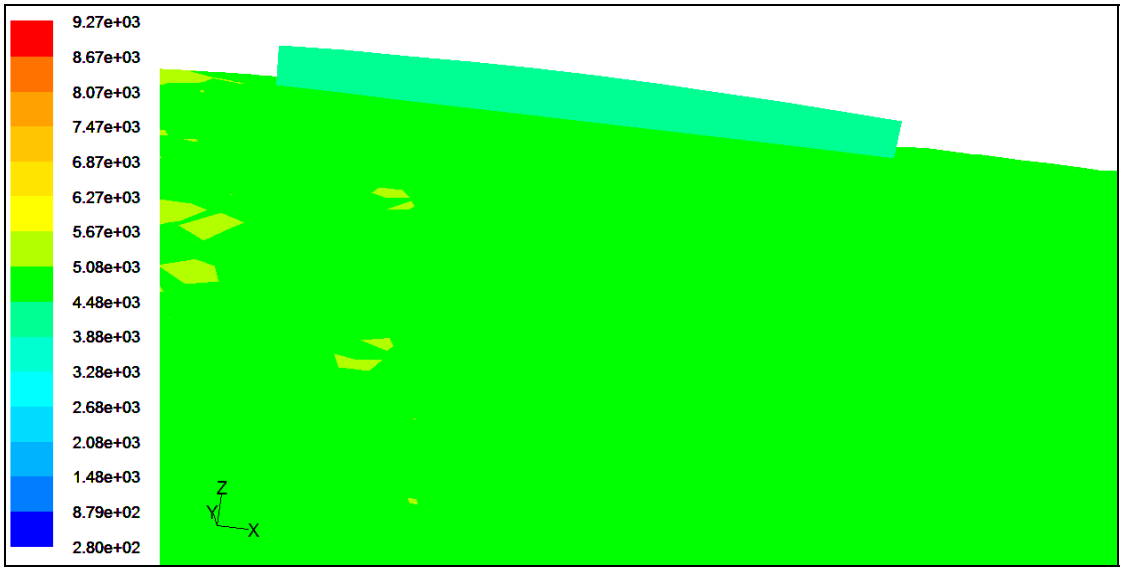

(e)

Figures 5.17: Close up View of Contours of Pressure Coefficient of Wigley Hull and its Free Surface for a)Fn = 0.173,b)Fn = 0.205, c) Fn = 0.267, d) Fn = 0.355 and e) Fn = 0.476.

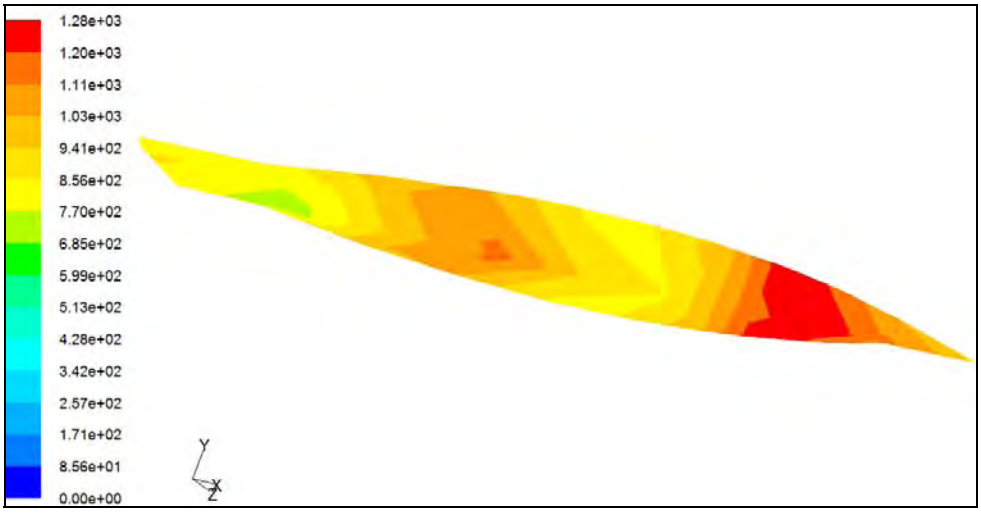
1.28e+03
1.20e+03
1.11e+03
1.03e+03
9.41e+02
8.56e+02
7.70e+02
6.85e+02
5.99e+02
5.13e+02
4.28e+02
3.42e+02
2.57e+02
1.71e+02
8.56e+01
0.00e+00
Y
X
Z

(a)

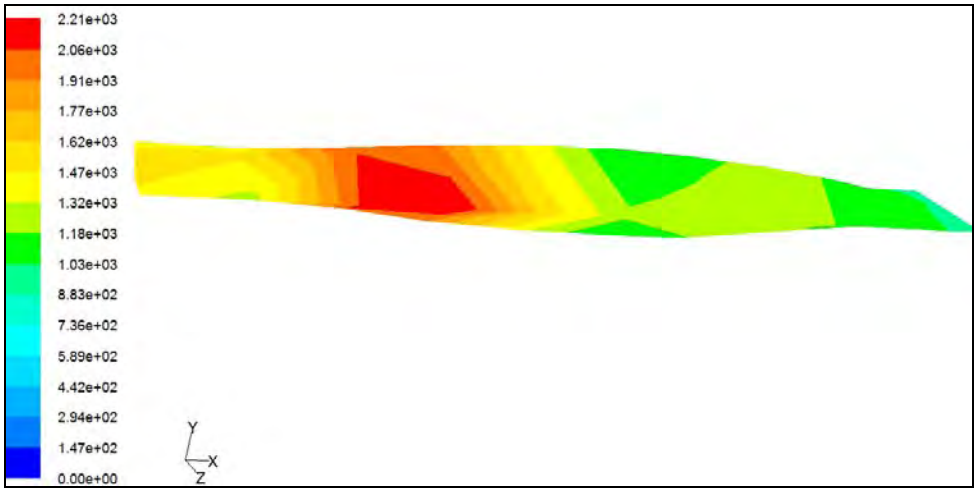
2.21e+03
2.06e+03
1.91e+03
1.77e+03
1.62e+03
1.47e+03
1.32e+03
1.18e+03
1.03e+03
8.83e+02
7.36e+02
5.89e+02
4.42e+02
2.94e+02
1.47e+02
0.00e+00
Y
X
Z

(b)

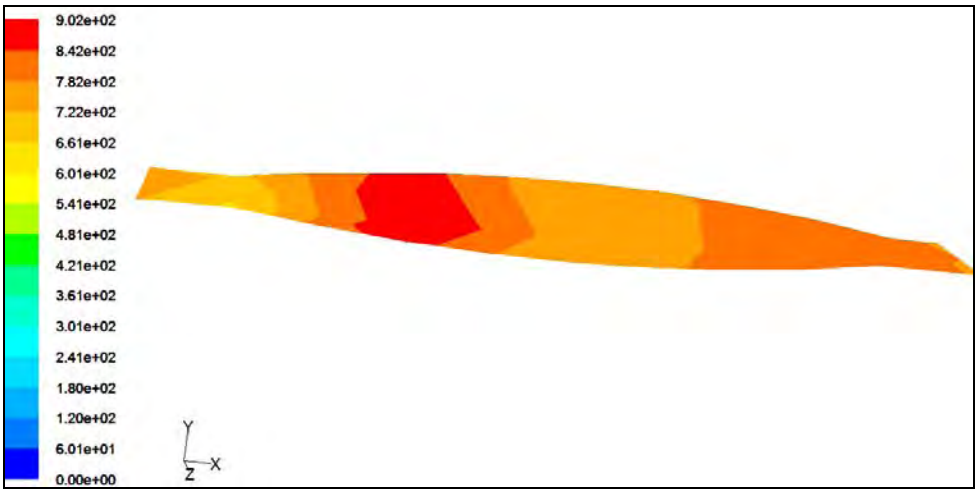
9.02e+02
8.42e+02
7.82e+02
7.22e+02
6.61e+02
6.01e+02
5.41e+02
4.81e+02
4.21e+02
3.61e+02
3.01e+02
2.41e+02
1.80e+02
1.20e+02
6.01e+01
0.00e+00
Y
X
Z

(c)

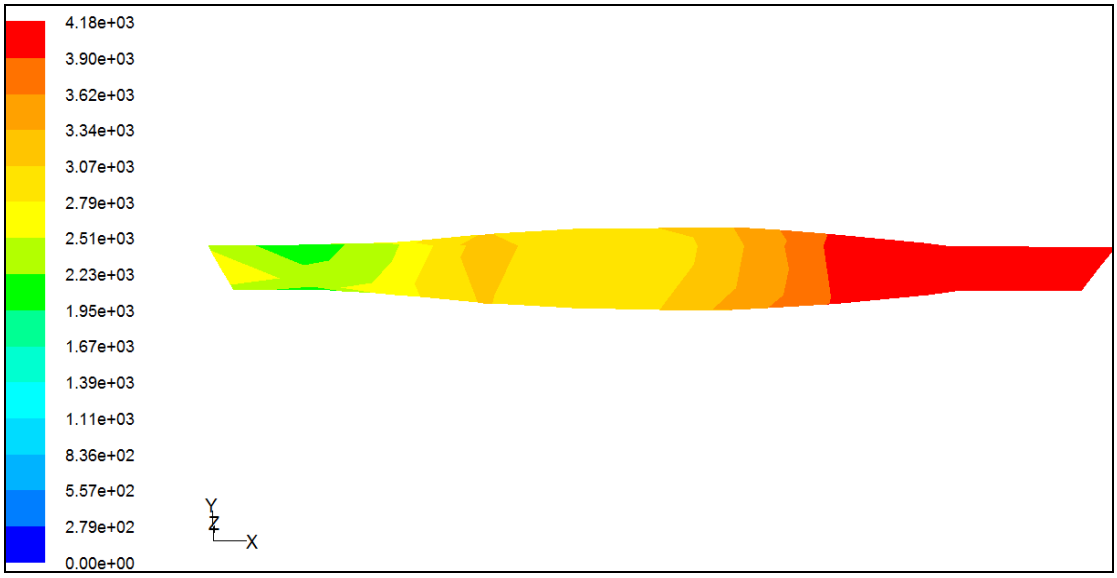

(d)

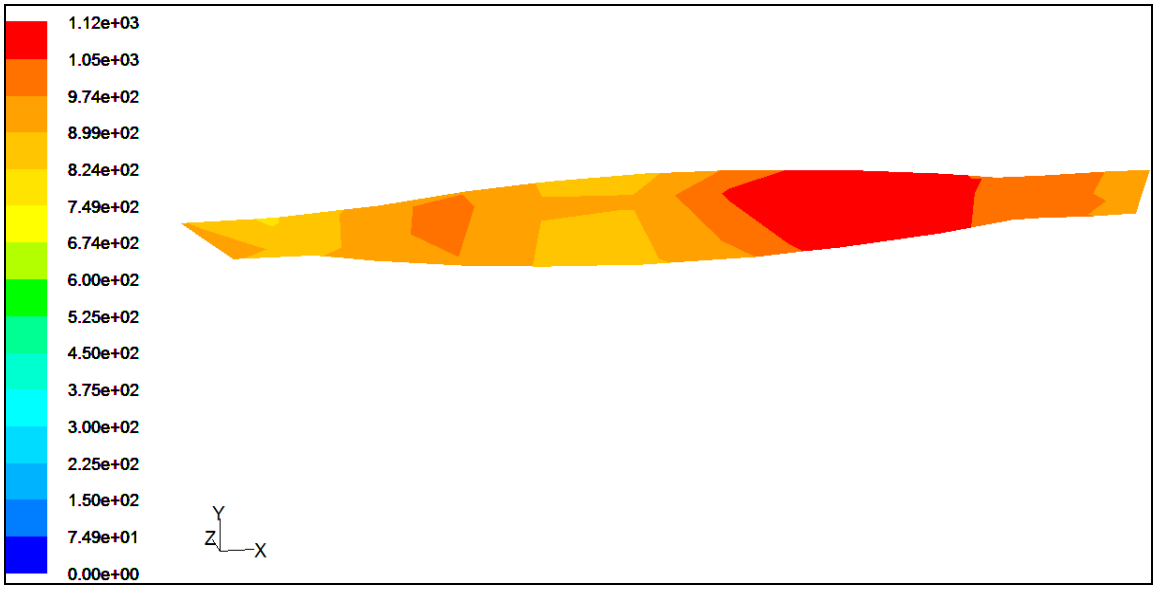

(e)

Figures 5.18: Contours of Wall Y+ of Wigley Hull for
a)Fn = 0.173,b)Fn = 0.205, c) Fn = 0.267,
d) Fn = 0.355 and e) Fn = 0.476.

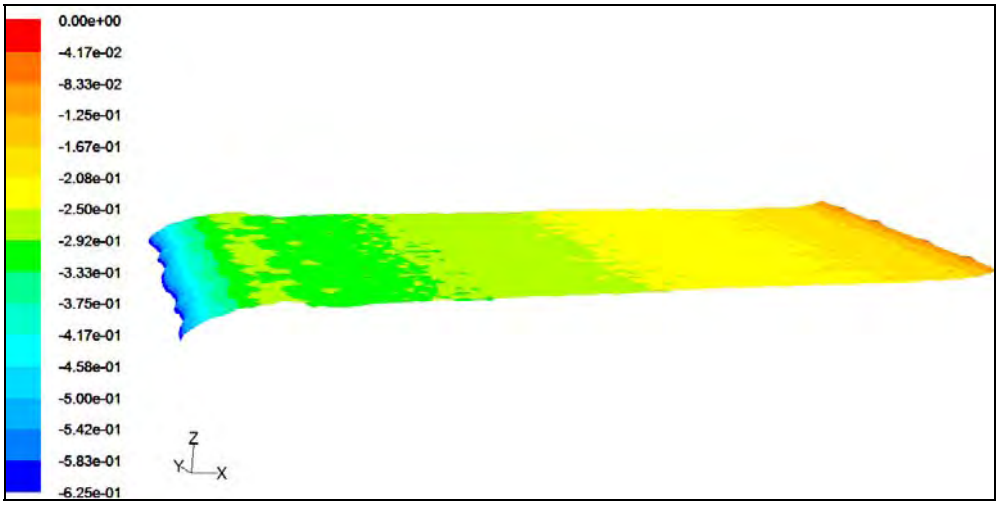
0.00e+00
-4.17e-02
-8.33e-02
-1.25e-01
-1.67e-01
-2.08e-01
-2.50e-01
-2.92e-01
-3.33e-01
-3.75e-01
-4.17e-01
-4.58e-01
-5.00e-01
-5.42e-01
-5.83e-01
-6.25e-01
Z
Y
X

(a)

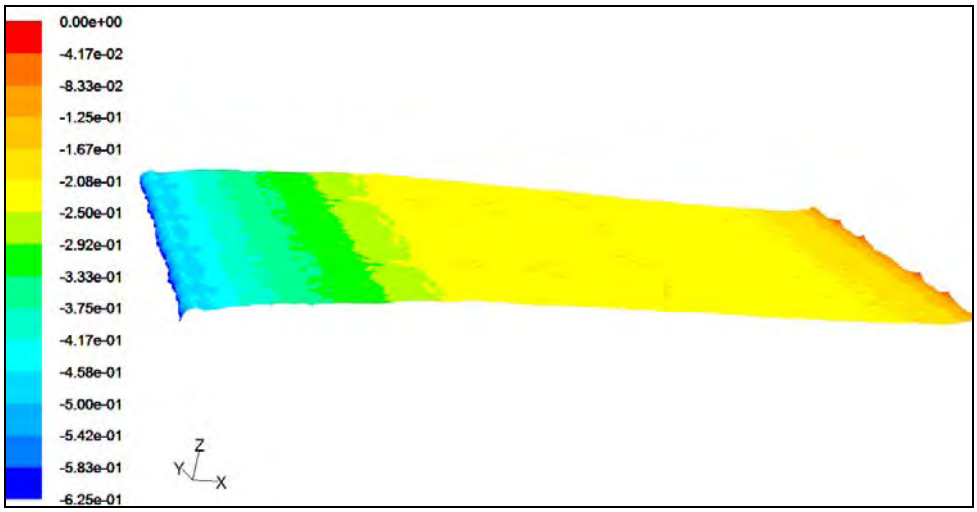
0.00e+00
-4.17e-02
-8.33e-02
-1.25e-01
-1.67e-01
-2.08e-01
-2.50e-01
-2.92e-01
-3.33e-01
-3.75e-01
-4.17e-01
-4.58e-01
-5.00e-01
-5.42e-01
-5.83e-01
-6.25e-01
Z
Y
X

(b)

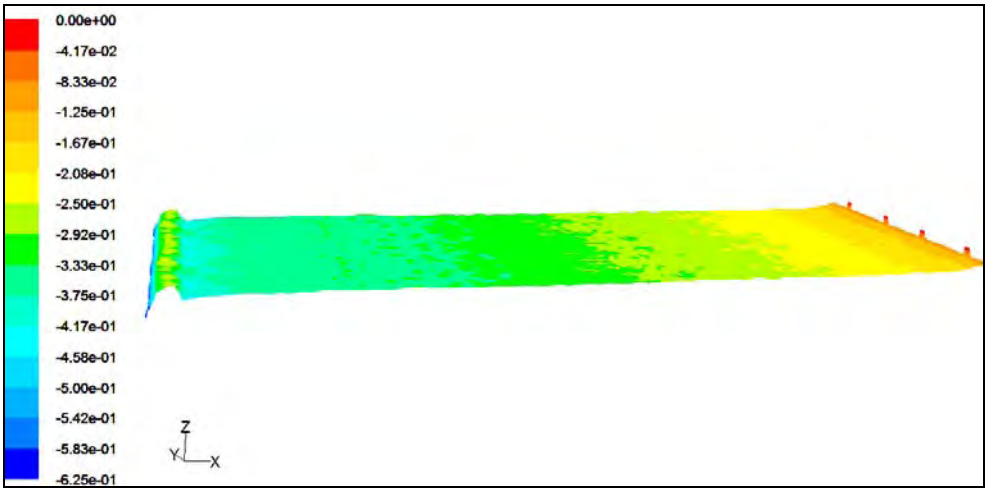
0.00e+00
-4.17e-02
-8.33e-02
-1.25e-01
-1.67e-01
-2.08e-01
-2.50e-01
-2.92e-01
-3.33e-01
-3.75e-01
-4.17e-01
-4.58e-01
-5.00e-01
-5.42e-01
-5.83e-01
-6.25e-01
Z
Y
X

(c)

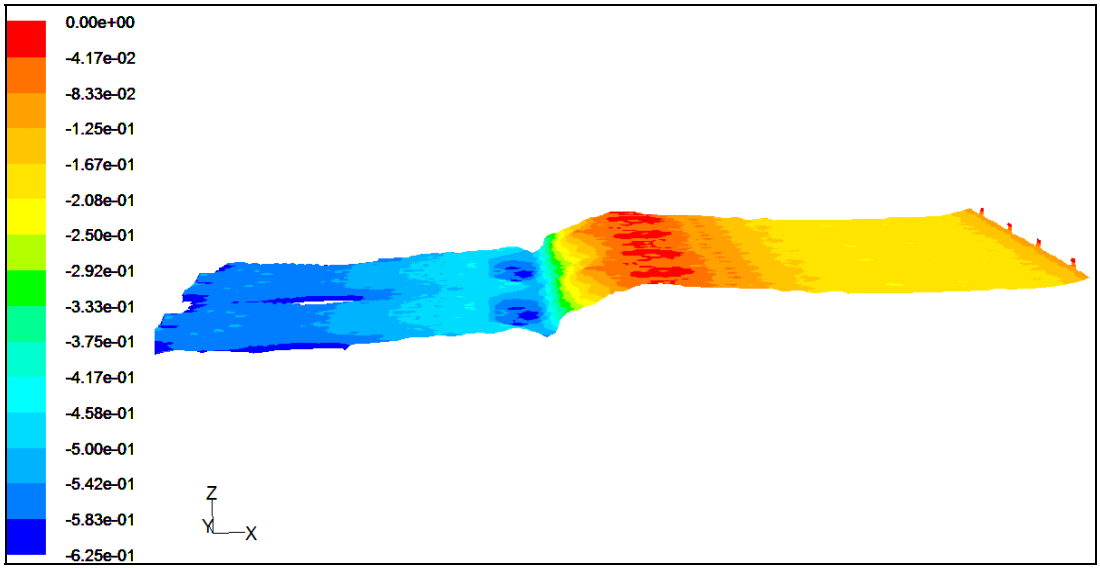

(d)

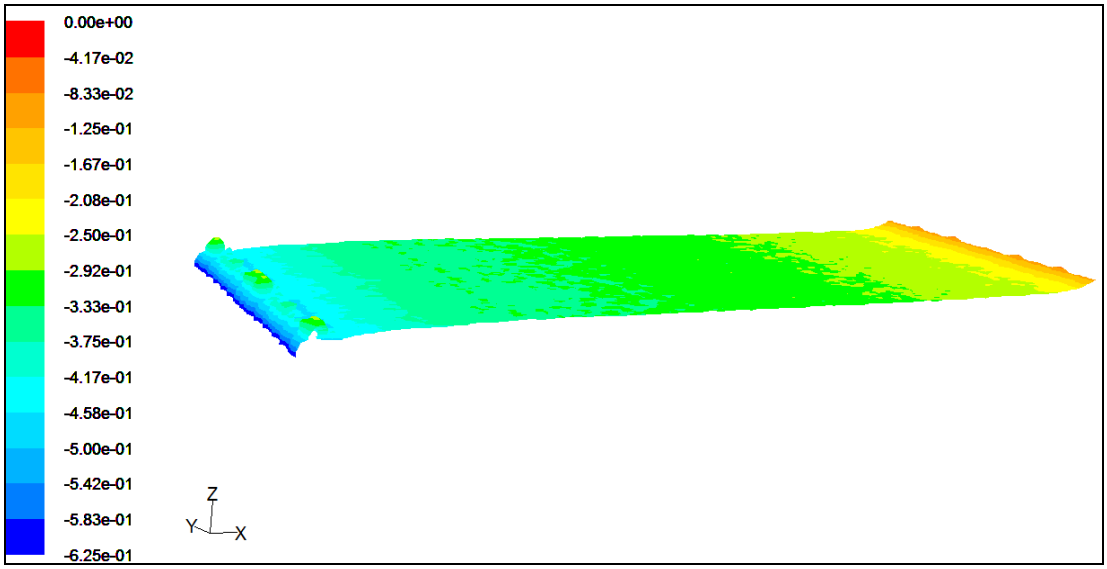

(e)

Figures 5.19: Contour Position of Free Surface About z Axis of Wigley Hull for (a) Fn = 0.173, (b) Fn = 0.205, (c) Fn = 0.267, d) Fn = 0.355 and e) Fn = 0.476.

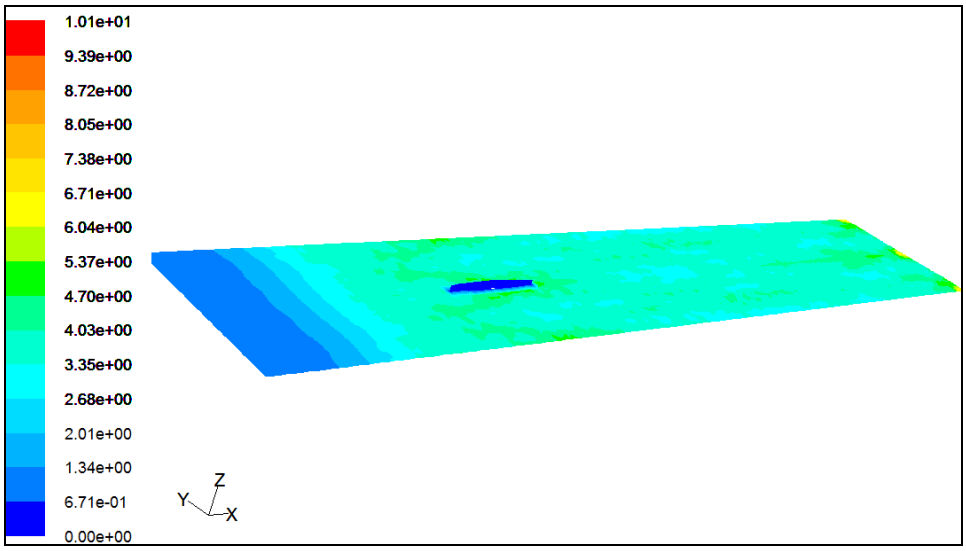
1.01e+01
9.39e+00
8.72e+00
8.05e+00
7.38e+00
6.71e+00
6.04e+00
5.37e+00
4.70e+00
4.03e+00
3.35e+00
2.68e+00
2.01e+00
1.34e+00
6.71e-01
0.00e+00
Z
Y
X

(a)

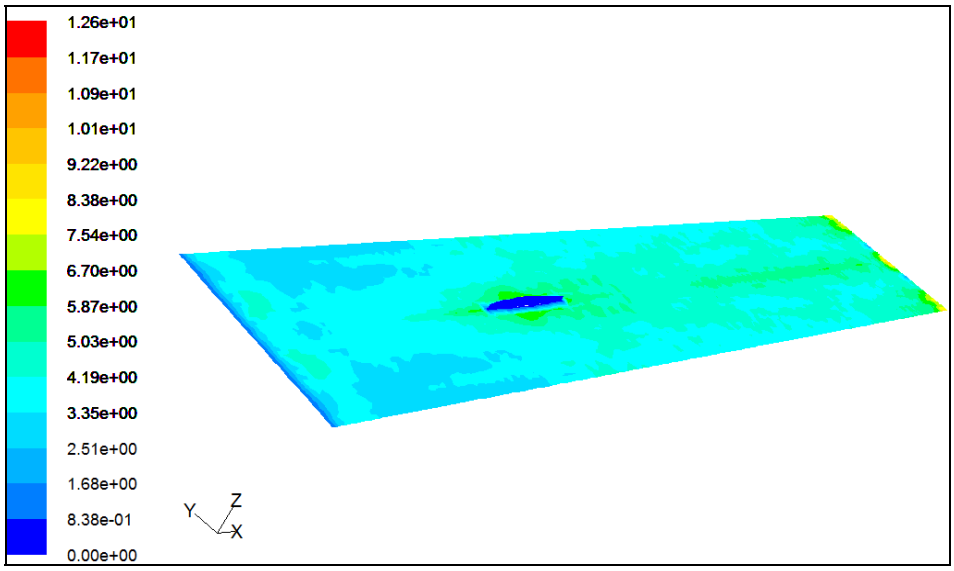
1.26e+01
1.17e+01
1.09e+01
1.01e+01
9.22e+00
8.38e+00
7.54e+00
6.70e+00
5.87e+00
5.03e+00
4.19e+00
3.35e+00
2.51e+00
1.68e+00
8.38e-01
0.00e+00
Z
Y
X

(b)

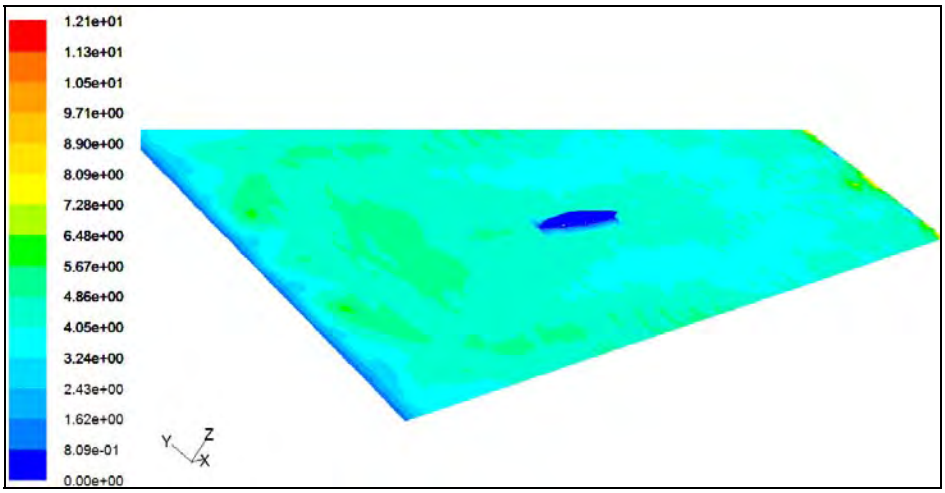
1.21e+01
1.13e+01
1.05e+01
9.71e+00
8.90e+00
8.09e+00
7.28e+00
6.48e+00
5.67e+00
4.86e+00
4.05e+00
3.24e+00
2.43e+00
1.62e+00
8.09e-01
0.00e+00
Z
Y
X

(c)

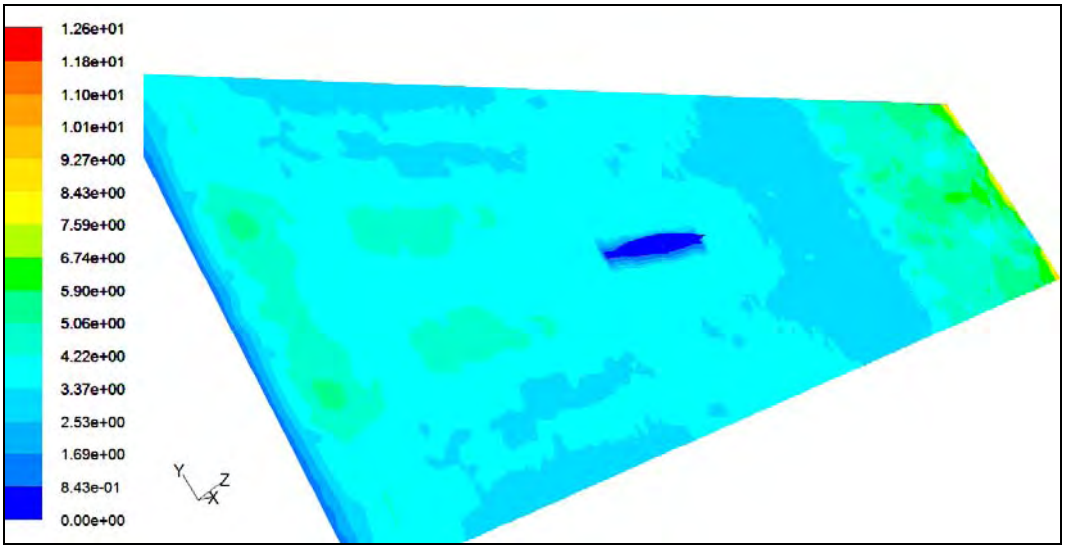

(d)

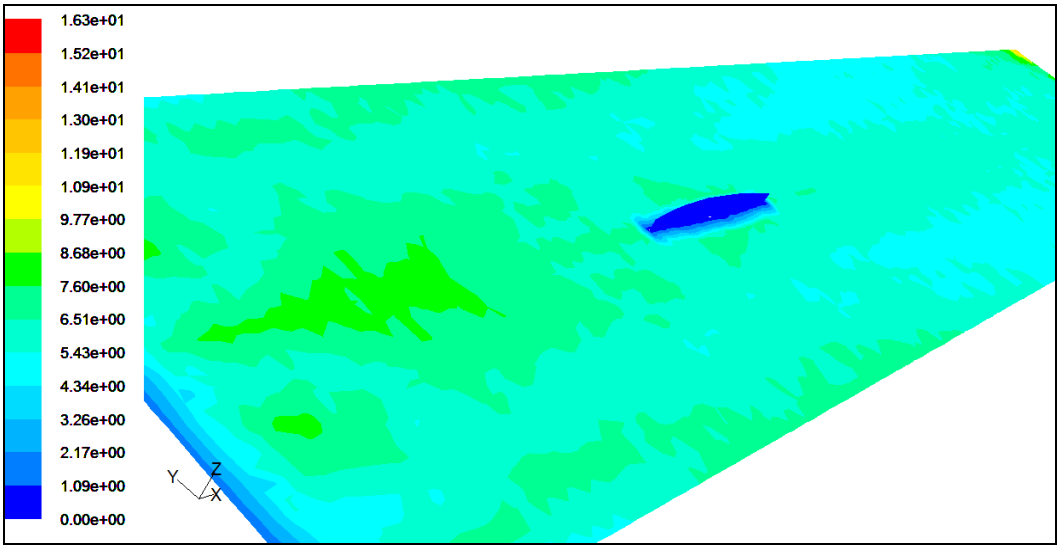

(e)

Figures 5.20: Contours of Velocity Magnitude of Wigley Hull and the Reference Surface for a)Fn = 0.173,b)Fn = 0.205, c) Fn = 0.267, d) Fn = 0.355 and e) Fn = 0.476.

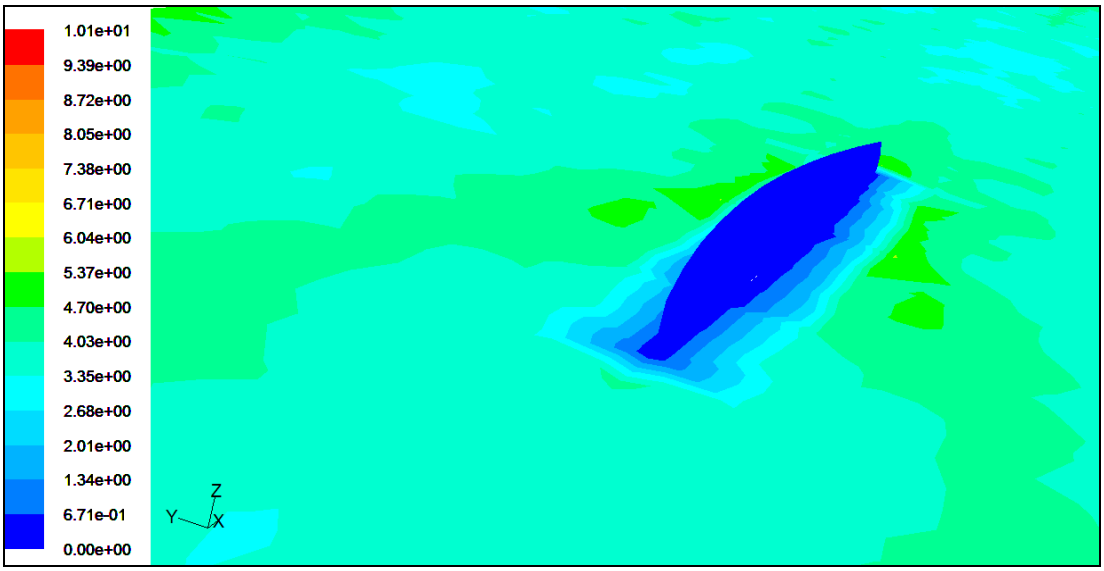
1.01e+01
9.39e+00
8.72e+00
8.05e+00
7.38e+00
6.71e+00
6.04e+00
5.37e+00
4.70e+00
4.03e+00
3.35e+00
2.68e+00
2.01e+00
1.34e+00
6.71e-01
0.00e+00
Z
Y
X

(a)

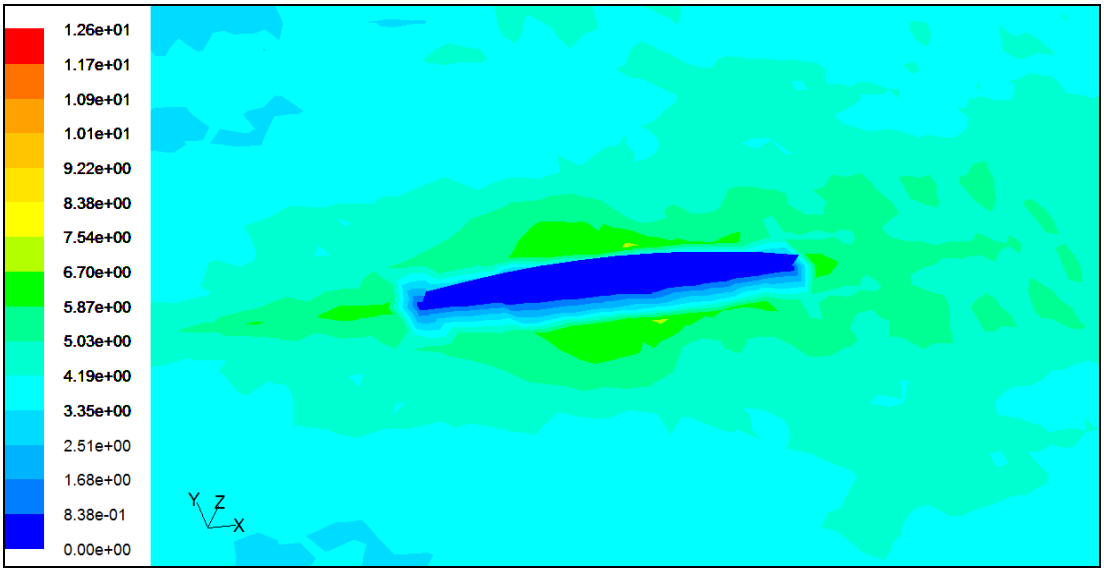
1.26e+01
1.17e+01
1.09e+01
1.01e+01
9.22e+00
8.38e+00
7.54e+00
6.70e+00
5.87e+00
5.03e+00
4.19e+00
3.35e+00
2.51e+00
1.68e+00
8.38e-01
0.00e+00
Y
Z
X

(b)

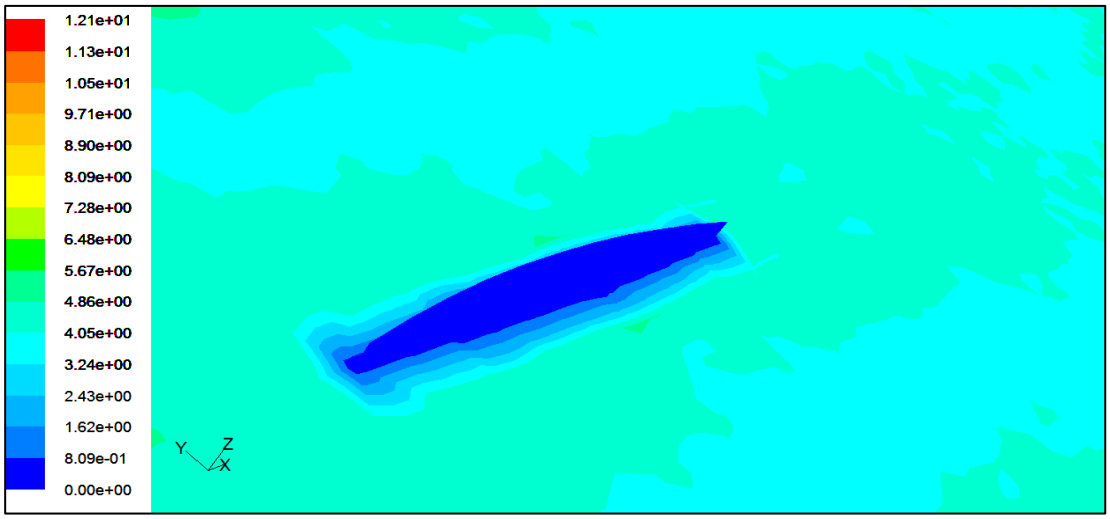
1.21e+01
1.13e+01
1.05e+01
9.71e+00
8.90e+00
8.09e+00
7.28e+00
6.48e+00
5.67e+00
4.86e+00
4.05e+00
3.24e+00
2.43e+00
1.62e+00
8.09e-01
0.00e+00
Y
Z
X

(c)

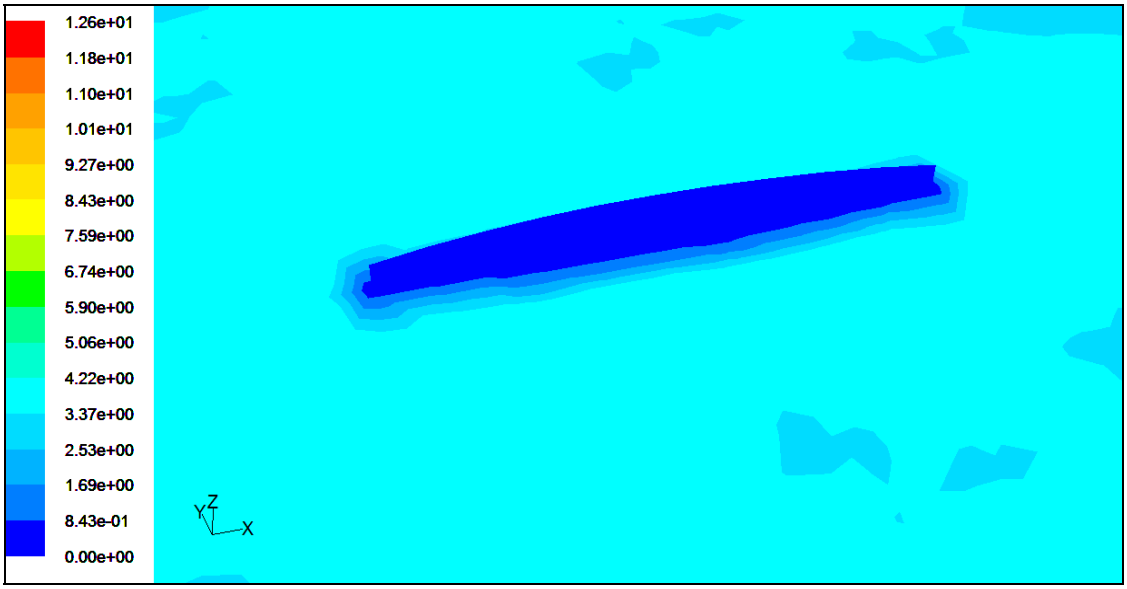

(d)

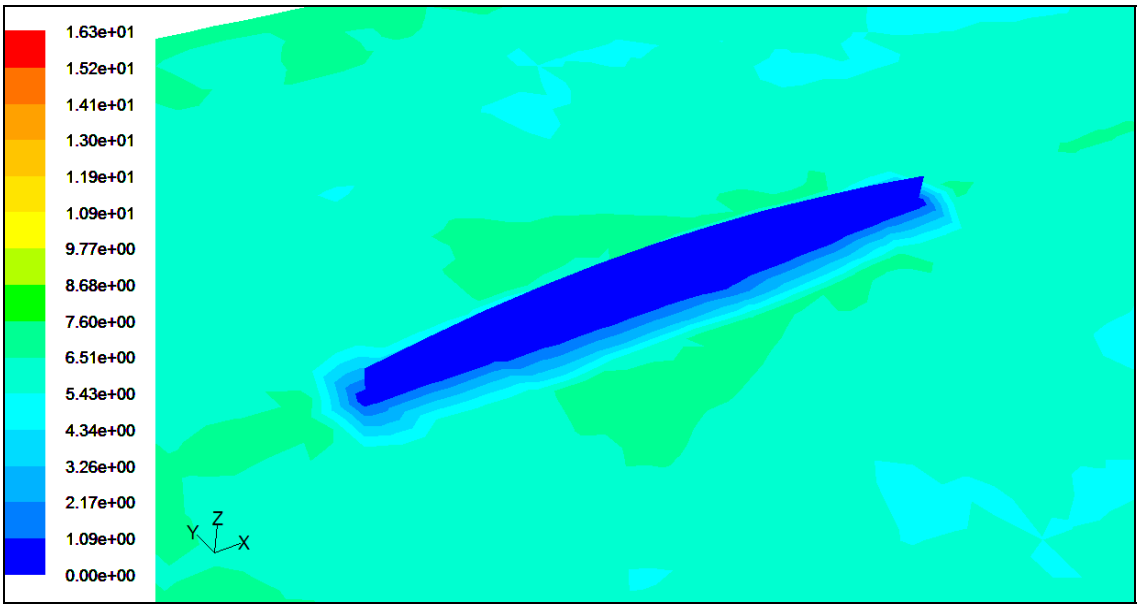

(e)

Figures 5.21: Contours of Close up View of Velocity Magnitude of Wigley Hull and the Reference Surface for a)Fn = 0.173,b)Fn = 0.205, c) Fn = 0.267, d) Fn = 0.355 and e) Fn = 0.476.

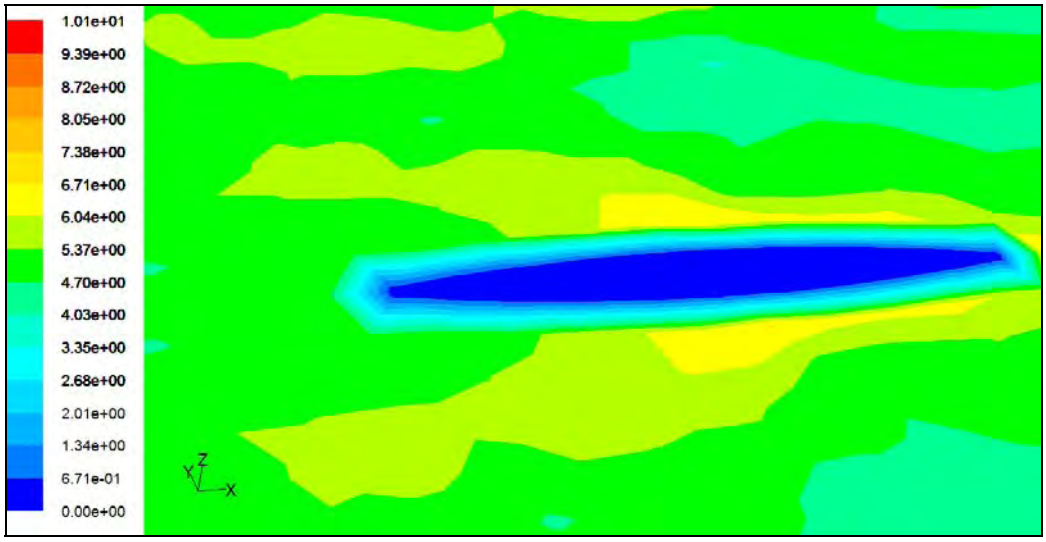
1.01e+01
9.39e+00
8.72e+00
8.05e+00
7.38e+00
6.71e+00
6.04e+00
5.37e+00
4.70e+00
4.03e+00
3.35e+00
2.68e+00
2.01e+00
1.34e+00
6.71e-01
0.00e+00
Z
Y
X

(a)

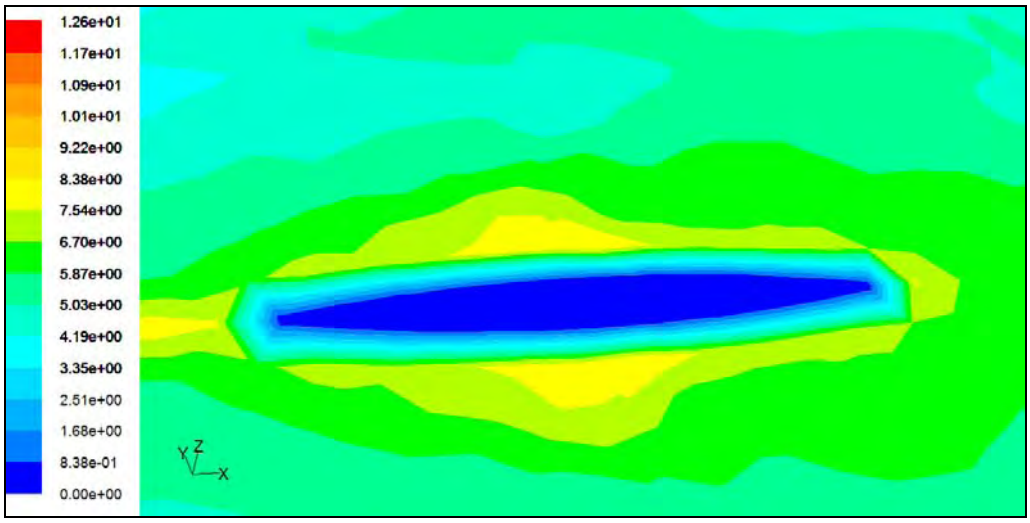
1.26e+01
1.17e+01
1.09e+01
1.01e+01
9.22e+00
8.38e+00
7.54e+00
6.70e+00
5.87e+00
5.03e+00
4.19e+00
3.35e+00
2.51e+00
1.68e+00
8.38e-01
0.00e+00
Z
Y
X

(b)

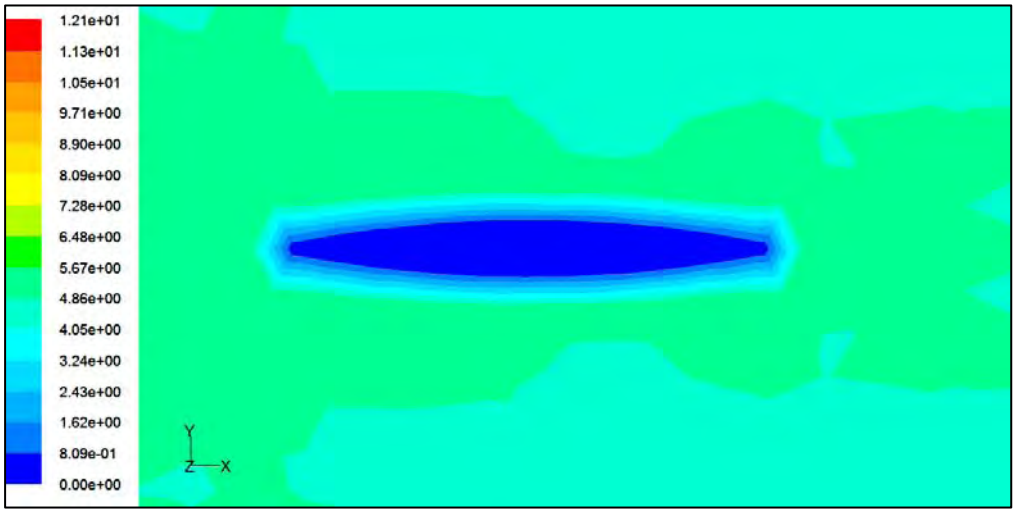
1.21e+01
1.13e+01
1.05e+01
9.71e+00
8.90e+00
8.09e+00
7.28e+00
6.48e+00
5.67e+00
4.86e+00
4.05e+00
3.24e+00
2.43e+00
1.62e+00
8.09e-01
0.00e+00
Y
Z
X

(c)

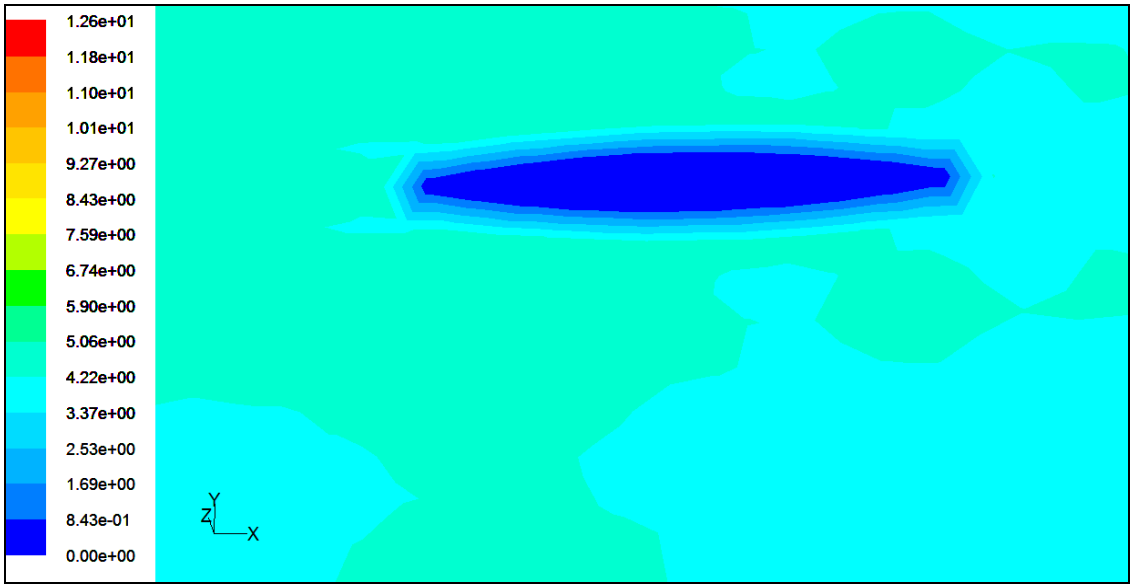

(d)

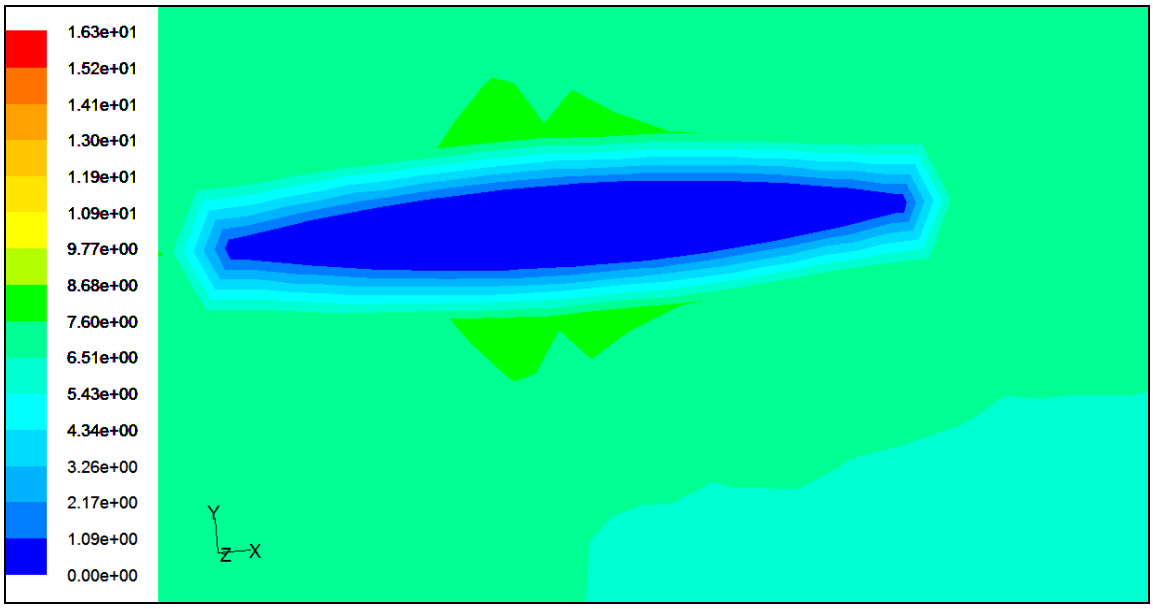

(e)

Figures 5.22: Contours of Velocity Magnitude of Wigley Hull and Symmetric Top Side of the Volume for a)Fn = 0.173,b)Fn = 0.205, c) Fn = 0.267,d) Fn = 0.355 and e) Fn = 0.476.

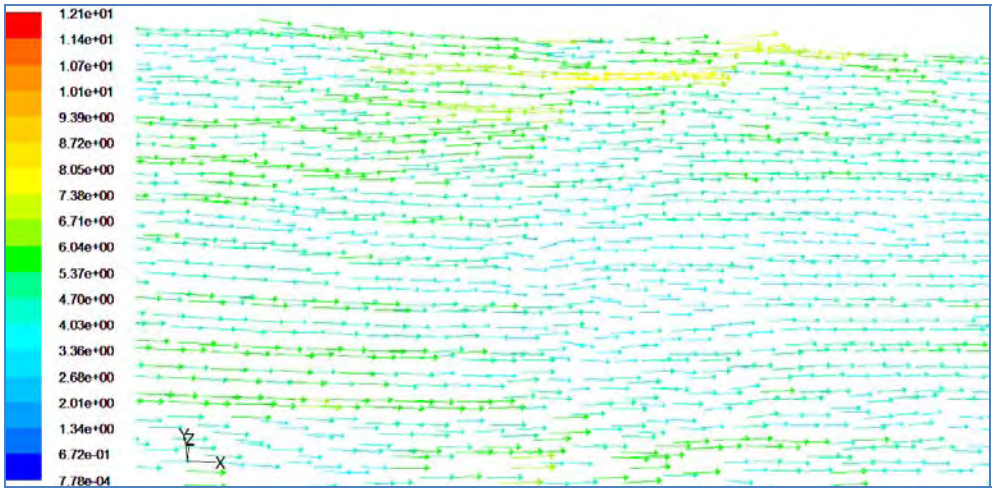
1.21e+01
1.14e+01
1.07e+01
1.01e+01
9.39e+00
8.72e+00
8.05e+00
7.38e+00
6.71e+00
6.04e+00
5.37e+00
4.70e+00
4.03e+00
3.36e+00
2.68e+00
2.01e+00
1.34e+00
6.72e-01
7.78e-04
Y
Z
X

(a)

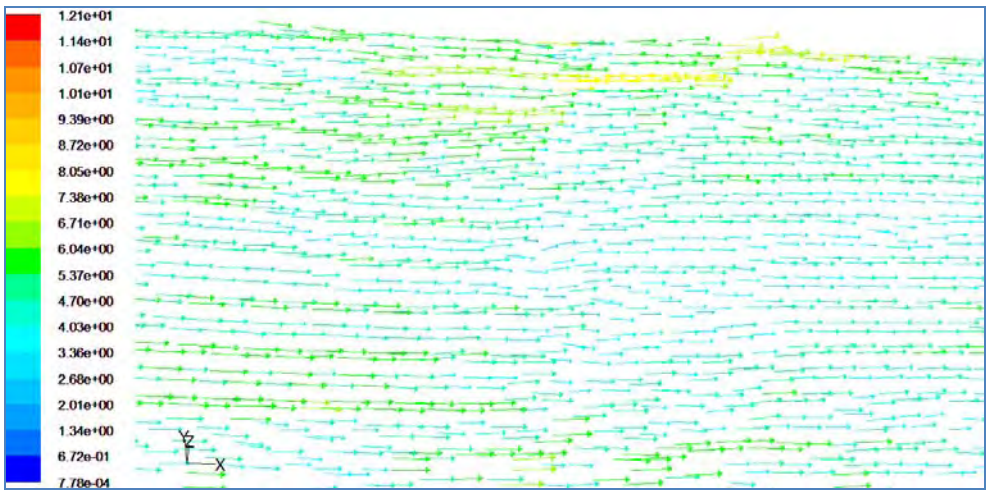
1.21e+01
1.14e+01
1.07e+01
1.01e+01
9.39e+00
8.72e+00
8.05e+00
7.38e+00
6.71e+00
6.04e+00
5.37e+00
4.70e+00
4.03e+00
3.36e+00
2.68e+00
2.01e+00
1.34e+00
6.72e-01
7.78e-04
Y
Z
X

(b)

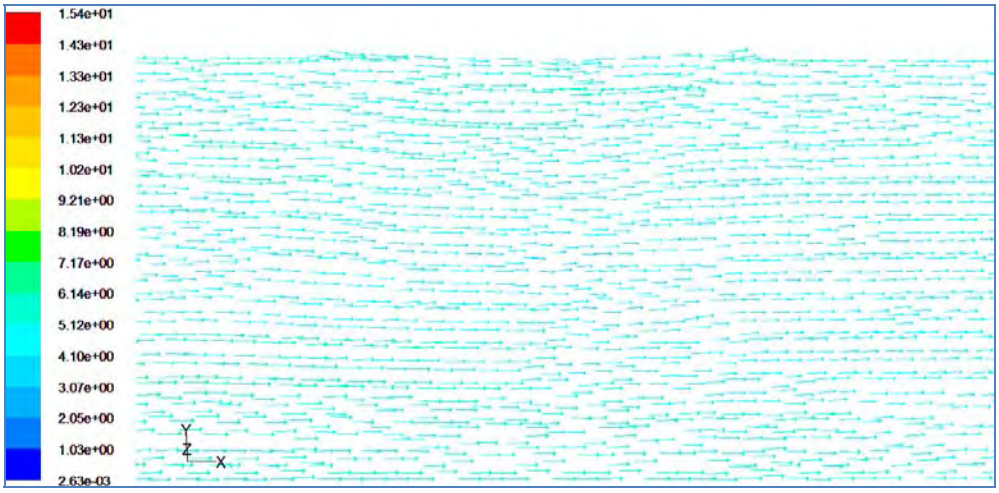
1.54e+01
1.43e+01
1.33e+01
1.23e+01
1.13e+01
1.02e+01
9.21e+00
8.19e+00
7.17e+00
6.14e+00
5.12e+00
4.10e+00
3.07e+00
2.05e+00
1.03e+00
2.63e-03
Y
Z
X

(c)

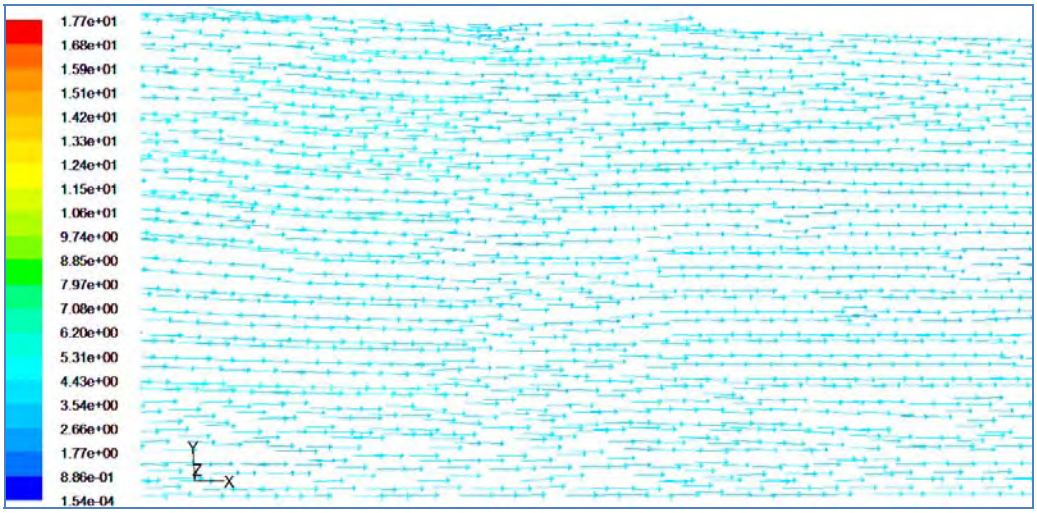

(d)

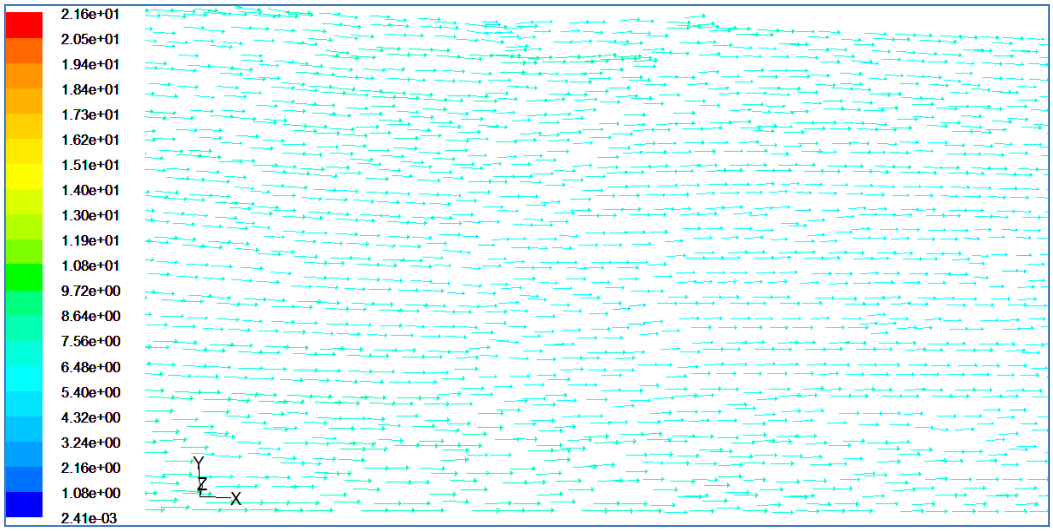

(e)

Figures 5.23: Contours of Velocity Vectors of Wigley Hull and the Reference Surface for a)Fn = 0.173,b)Fn = 0.205, c) Fn = 0.267,d) Fn = 0.355 and e) Fn = 0.476.

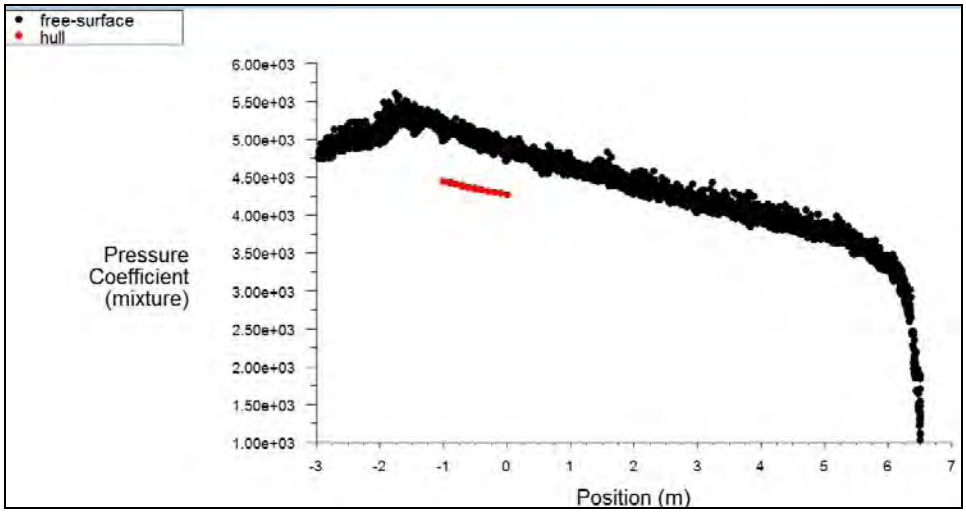
free-surface
hull
Pressure Coefficient (mixture)
6.00e+03
5.50e+03
5.00e+03
4.50e+03
4.00e+03
3.50e+03
3.00e+03
2.50e+03
2.00e+03
1.50e+03
1.00e+03
-3 -2 -1 0 1 2 3 4 5 6 7
Position (m)

(a)

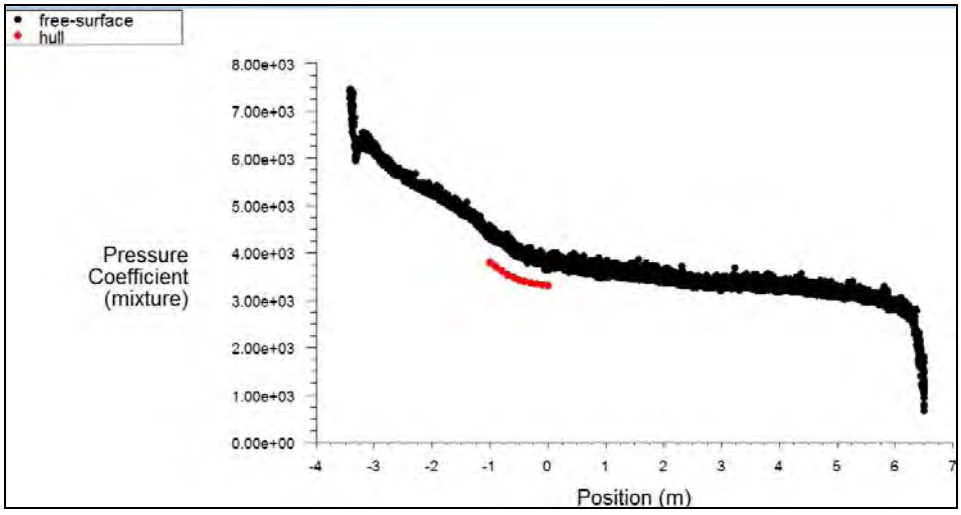
free-surface
hull
Pressure Coefficient (mixture)
8.00e+03
7.00e+03
6.00e+03
5.00e+03
4.00e+03
3.00e+03
2.00e+03
1.00e+03
0.00e+00
-4 -3 -2 -1 0 1 2 3 4 5 6 7
Position (m)

(b)

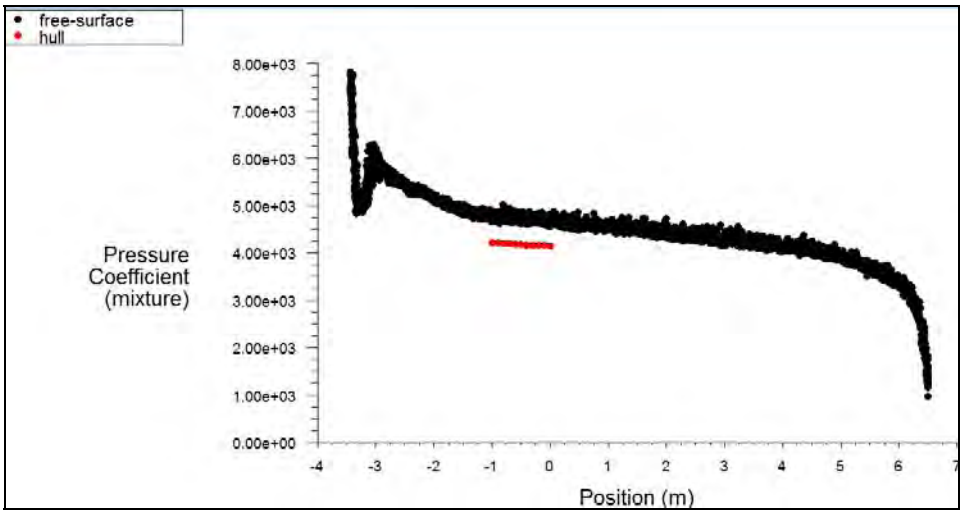
free-surface
hull
Pressure Coefficient (mixture)
8.00e+03
7.00e+03
6.00e+03
5.00e+03
4.00e+03
3.00e+03
2.00e+03
1.00e+03
0.00e+00
-4 -3 -2 -1 0 1 2 3 4 5 6 7
Position (m)

(c)

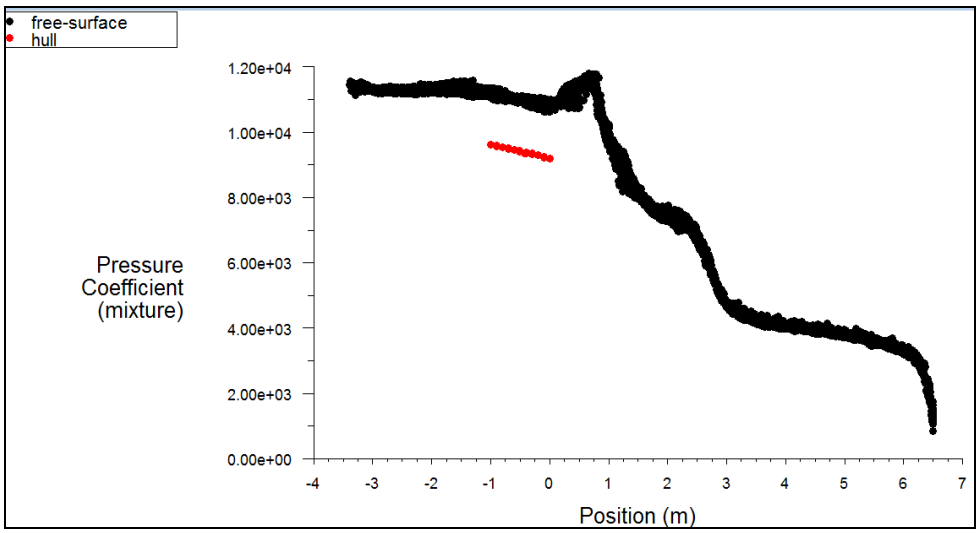

(d)

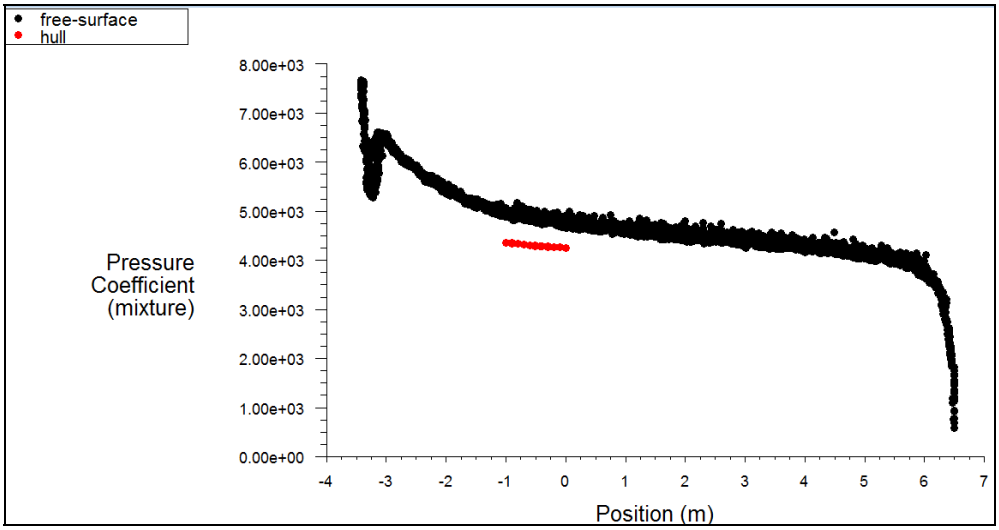

(e)

Figures 5.24: Plot of Pressure Co-Efficient of Wigley Hull and its Free Surface for a) Fn = 0.173,b)Fn = 0.205, c) Fn = 0.267,d) Fn = 0.355 and e) Fn = 0.476

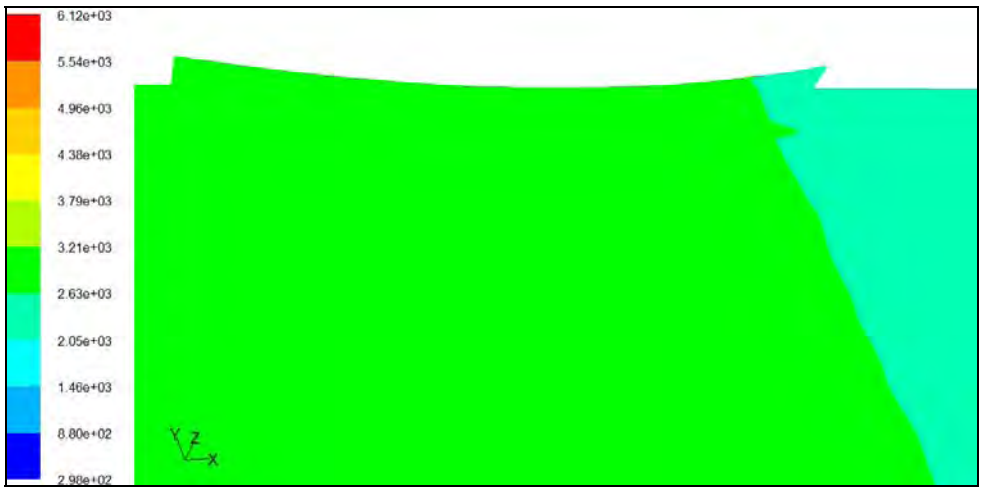
6.12e+03
5.54e+03
4.96e+03
4.38e+03
3.79e+03
3.21e+03
2.63e+03
2.05e+03
1.46e+03
8.80e+02
2.98e+02
Y
Z
X

(a)

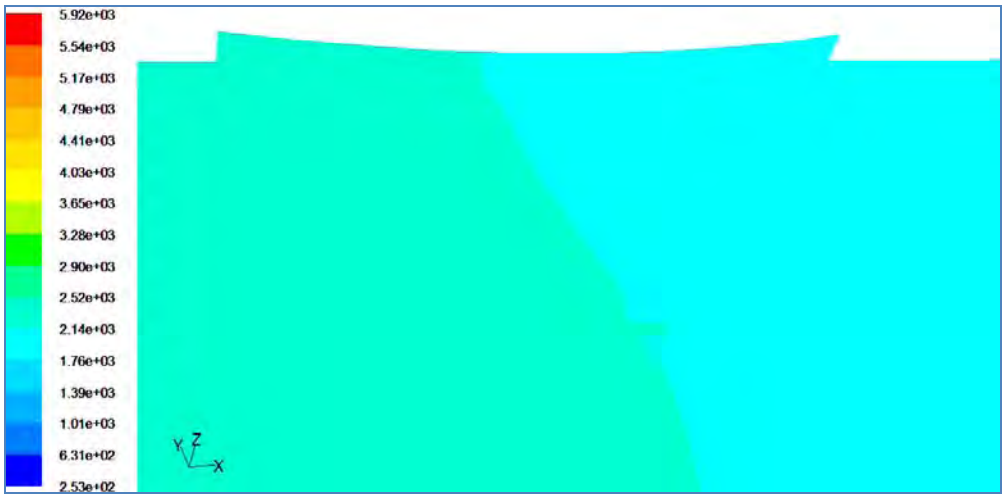
5.92e+03
5.54e+03
5.17e+03
4.79e+03
4.41e+03
4.03e+03
3.65e+03
3.28e+03
2.90e+03
2.52e+03
2.14e+03
1.76e+03
1.39e+03
1.01e+03
6.31e+02
2.53e+02
Y
Z
X

(b)

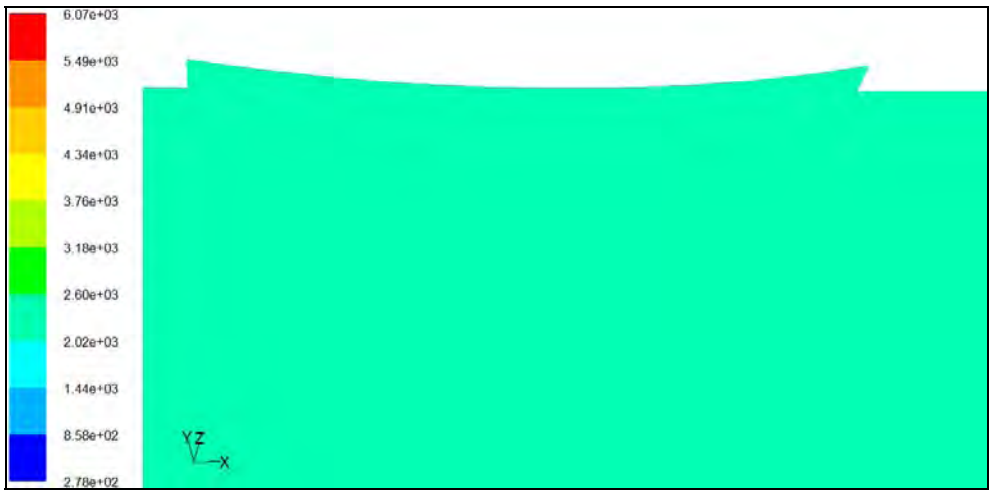
6.07e+03
5.49e+03
4.91e+03
4.34e+03
3.76e+03
3.18e+03
2.60e+03
2.02e+03
1.44e+03
8.58e+02
2.78e+02
Y
Z
X

(c)

(d)

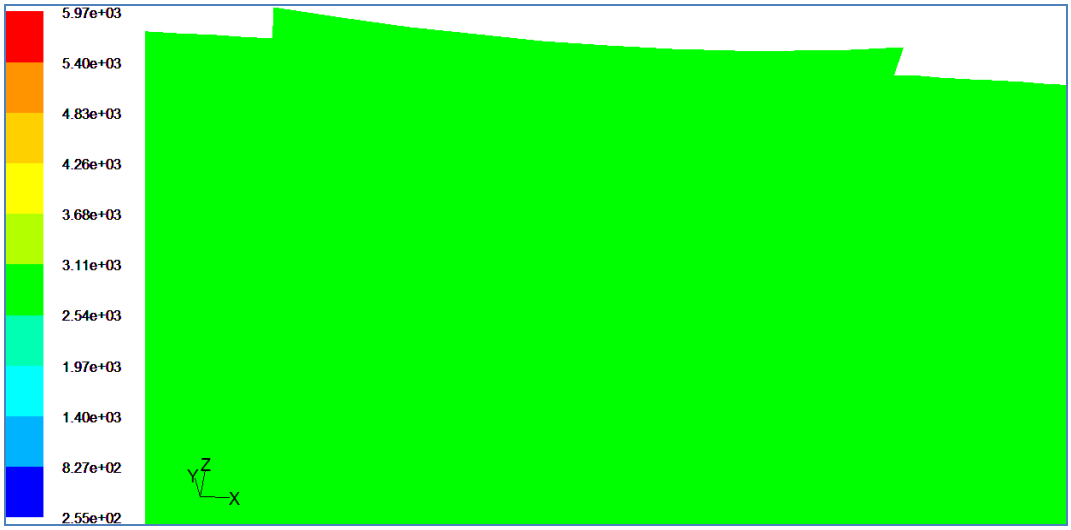

(e)

Figures 5.25: Close Up View of Pressure Co-Efficient of Wigley Hull and the Reference Surface for a)Fn = 0.173,b)Fn = 0.205, c) Fn = 0.267,d) Fn = 0.355 and e) Fn = 0.476.

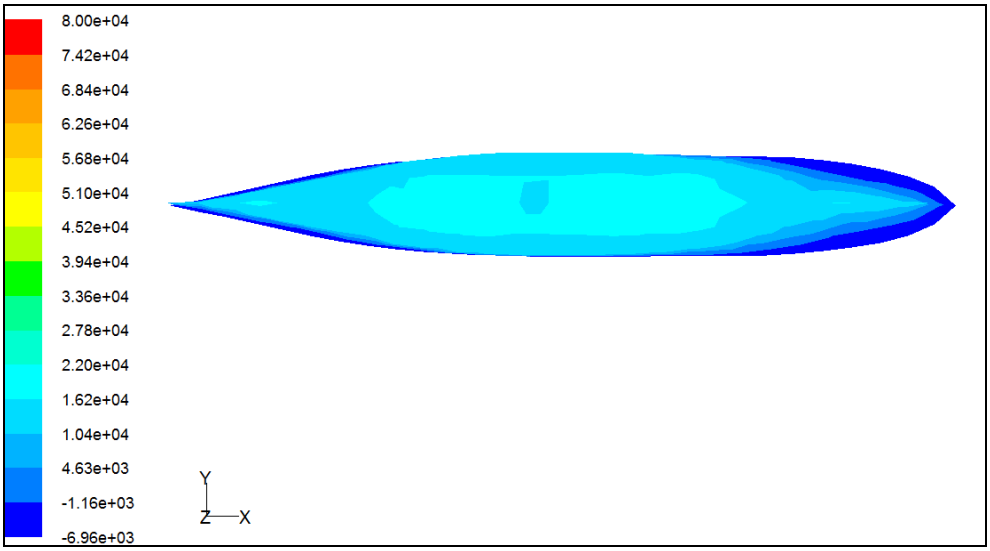
8.00e+04
7.42e+04
6.84e+04
6.26e+04
5.68e+04
5.10e+04
4.52e+04
3.94e+04
3.36e+04
2.78e+04
2.20e+04
1.62e+04
1.04e+04
4.63e+03
-1.16e+03
-6.96e+03
Y
Z
X

(a)

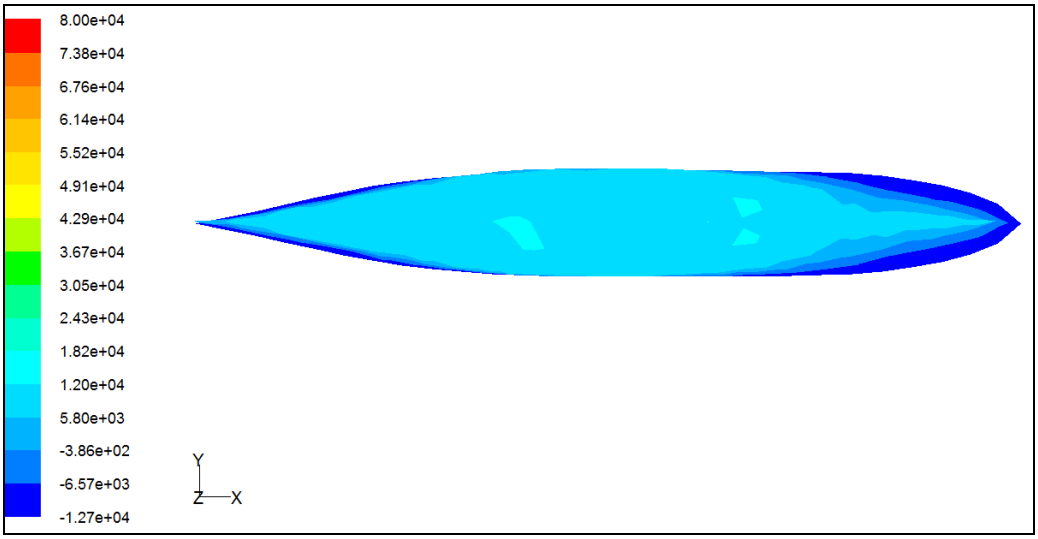
8.00e+04
7.38e+04
6.76e+04
6.14e+04
5.52e+04
4.91e+04
4.29e+04
3.67e+04
3.05e+04
2.43e+04
1.82e+04
1.20e+04
5.80e+03
-3.86e+02
-6.57e+03
-1.27e+04
Y
Z
X

(b)

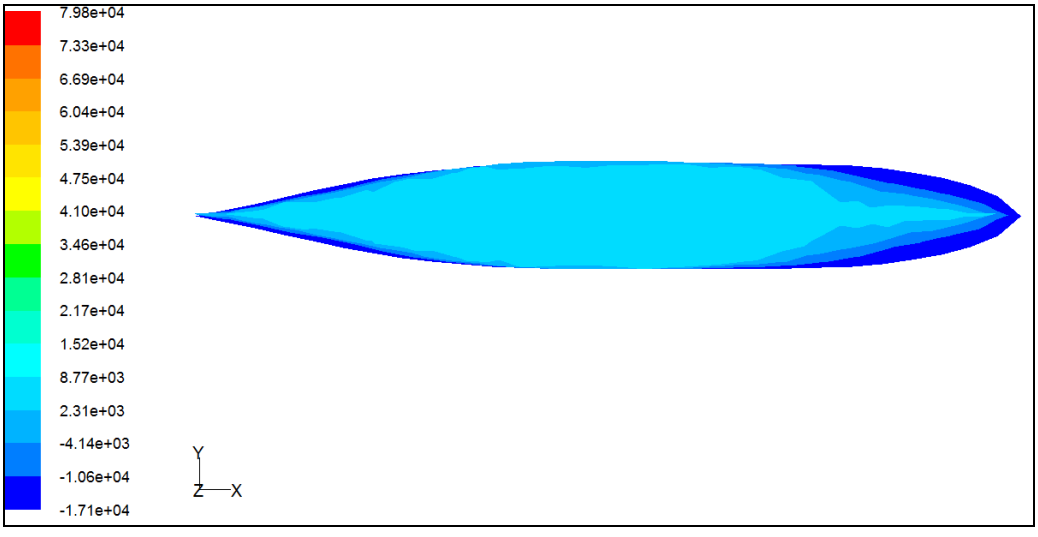
7.98e+04
7.33e+04
6.69e+04
6.04e+04
5.39e+04
4.75e+04
4.10e+04
3.46e+04
2.81e+04
2.17e+04
1.52e+04
8.77e+03
2.31e+03
-4.14e+03
-1.06e+04
-1.71e+04
Y
Z
X

(c)

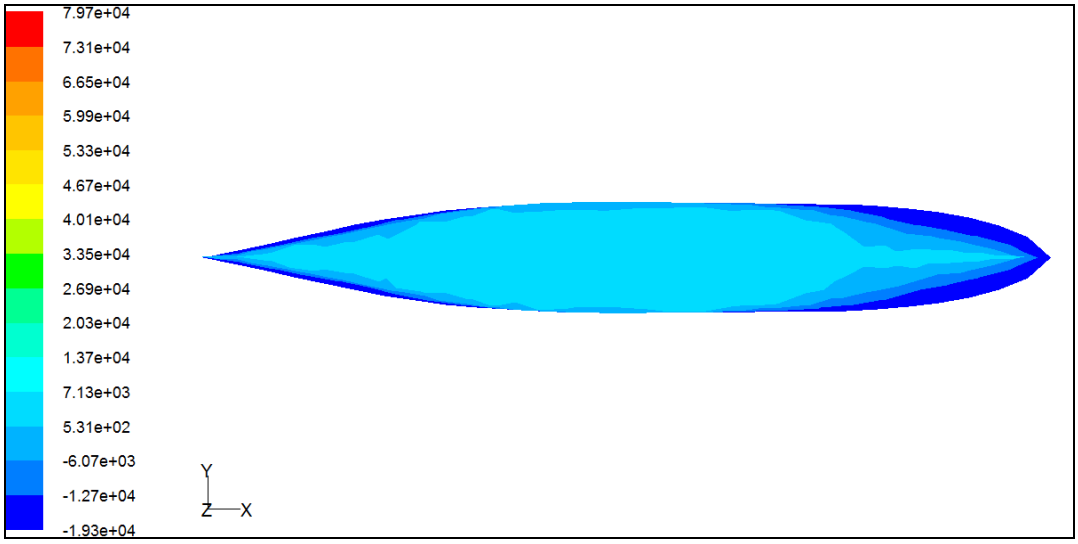

(d)

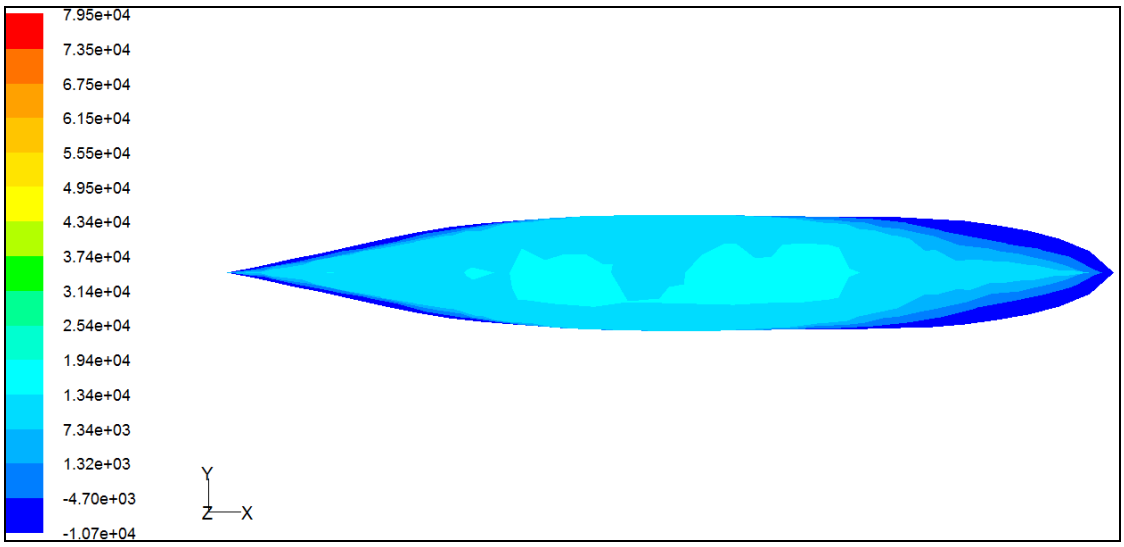

(e)

Figures 5.26: Contours of Pressure Coefficient of Series 60 Hull for a)Fn = 0.173,b)Fn = 0.205, c) Fn = 0.267, d) Fn = 0.355 and e) Fn = 0.476.

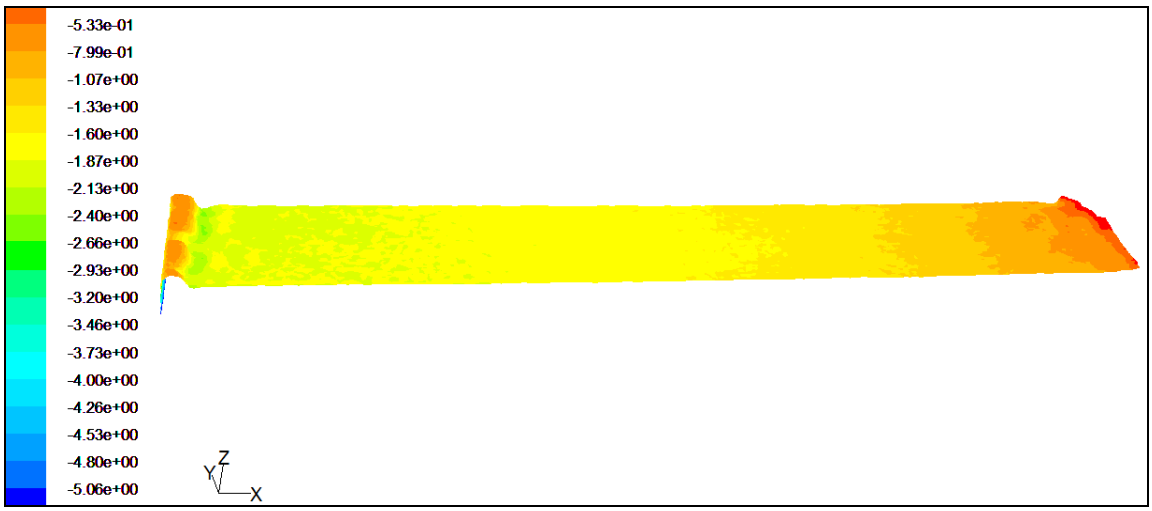
-5.33e-01
-7.99e-01
-1.07e+00
-1.33e+00
-1.60e+00
-1.87e+00
-2.13e+00
-2.40e+00
-2.66e+00
-2.93e+00
-3.20e+00
-3.46e+00
-3.73e+00
-4.00e+00
-4.26e+00
-4.53e+00
-4.80e+00
-5.06e+00
Z
Y
X

(a)

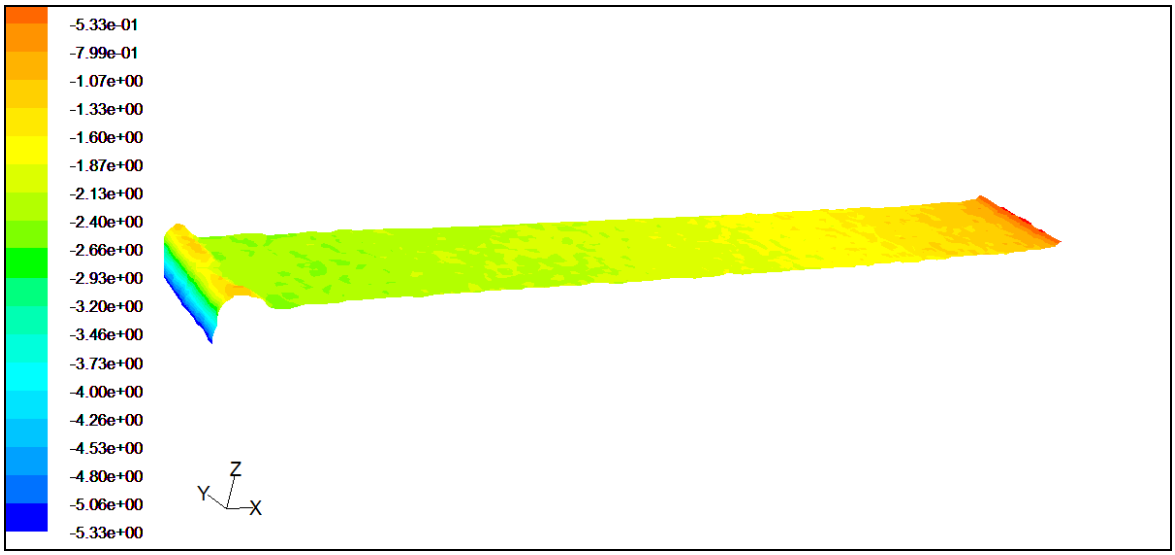
-5.33e-01
-7.99e-01
-1.07e+00
-1.33e+00
-1.60e+00
-1.87e+00
-2.13e+00
-2.40e+00
-2.66e+00
-2.93e+00
-3.20e+00
-3.46e+00
-3.73e+00
-4.00e+00
-4.26e+00
-4.53e+00
-4.80e+00
-5.06e+00
-5.33e+00
Z
Y
X

(b)

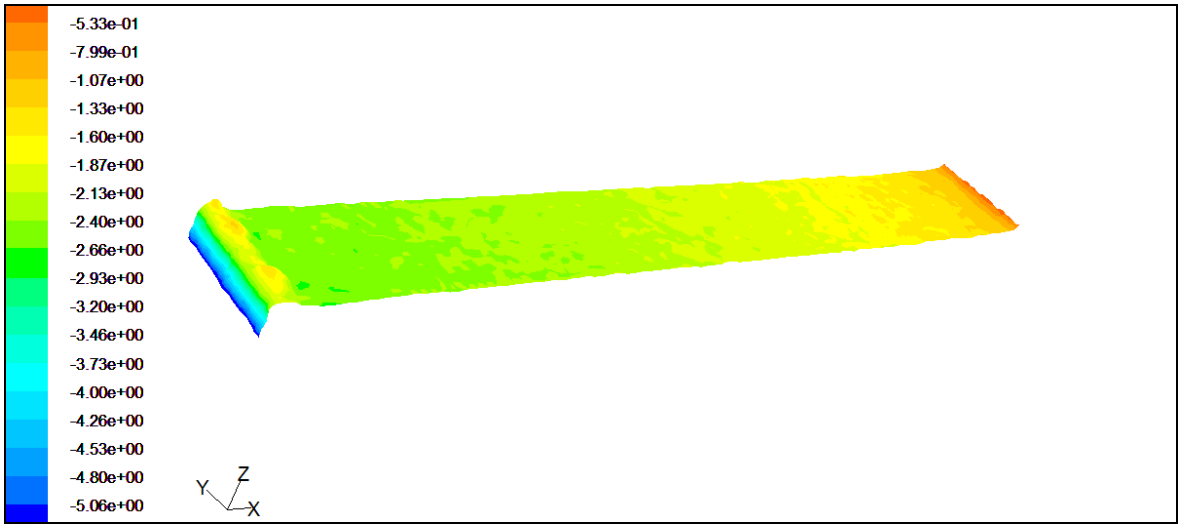
-5.33e-01
-7.99e-01
-1.07e+00
-1.33e+00
-1.60e+00
-1.87e+00
-2.13e+00
-2.40e+00
-2.66e+00
-2.93e+00
-3.20e+00
-3.46e+00
-3.73e+00
-4.00e+00
-4.26e+00
-4.53e+00
-4.80e+00
-5.06e+00
Z
Y
X

(c)

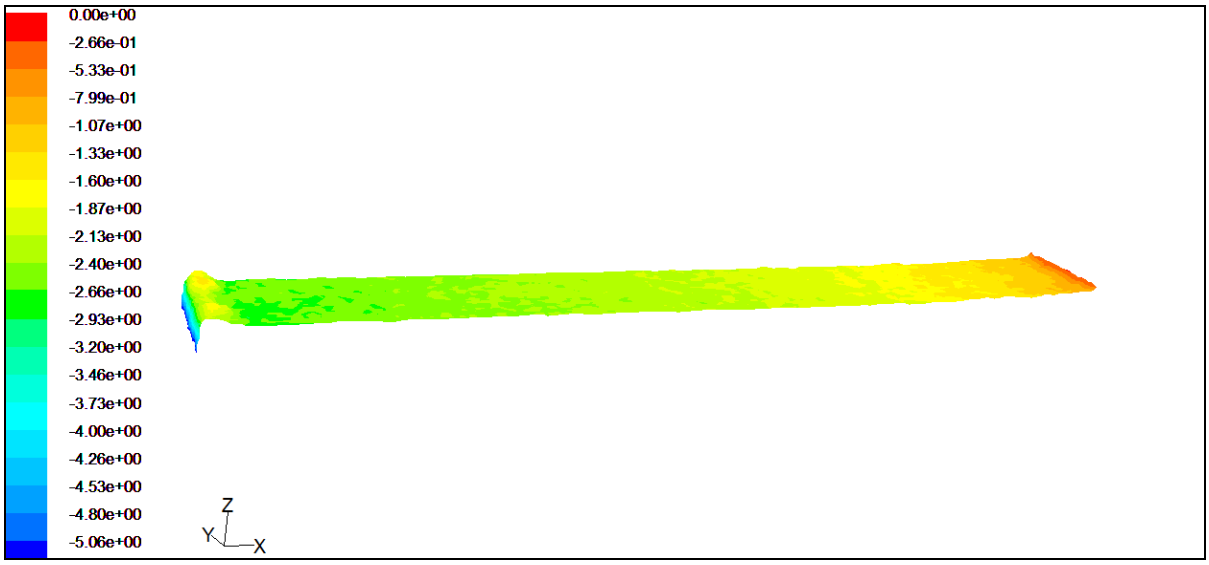

(d)

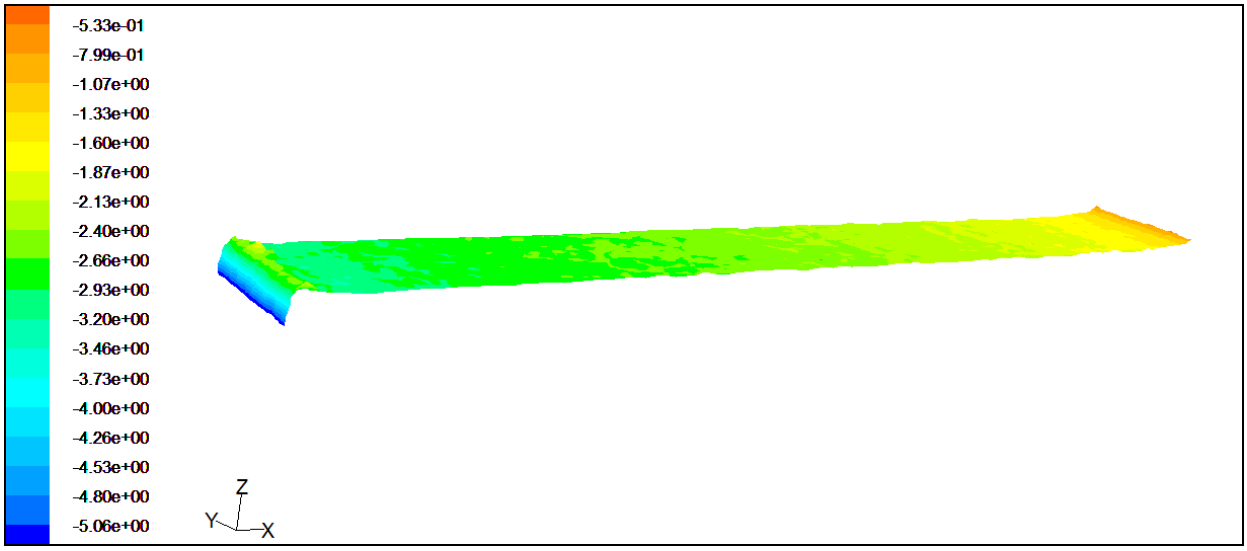

(e)

Figures 5.27: Contour Position of Free Surface About z Axis of Series 60 Hull for (a) Fn = 0.173, (b) Fn = 0.205, (c) Fn = 0.267, d) Fn = 0.355 and e) Fn = 0.476.

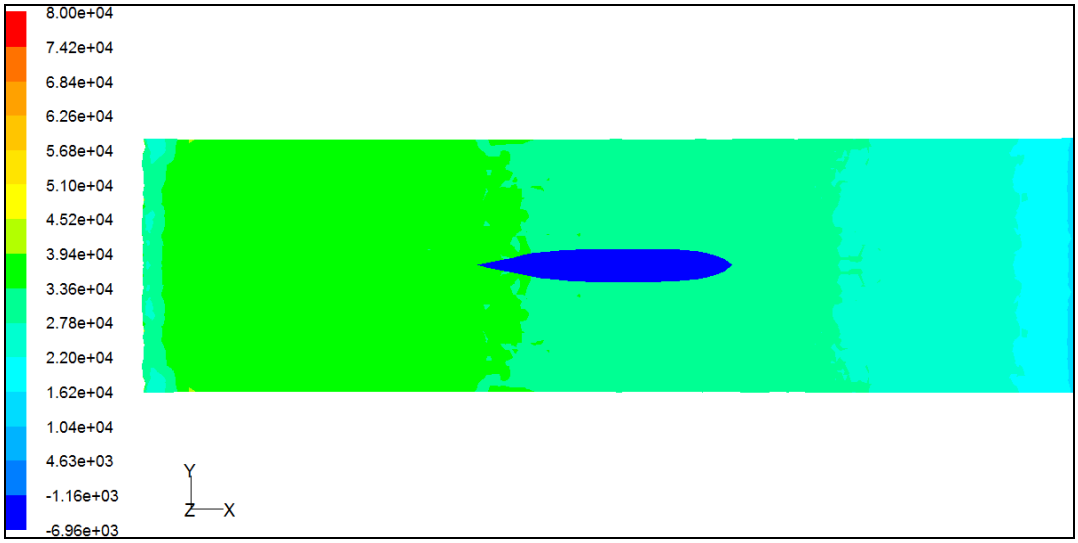
8.00e+04
7.42e+04
6.84e+04
6.26e+04
5.68e+04
5.10e+04
4.52e+04
3.94e+04
3.36e+04
2.78e+04
2.20e+04
1.62e+04
1.04e+04
4.63e+03
-1.16e+03
-6.96e+03
Y
Z
X

(a)

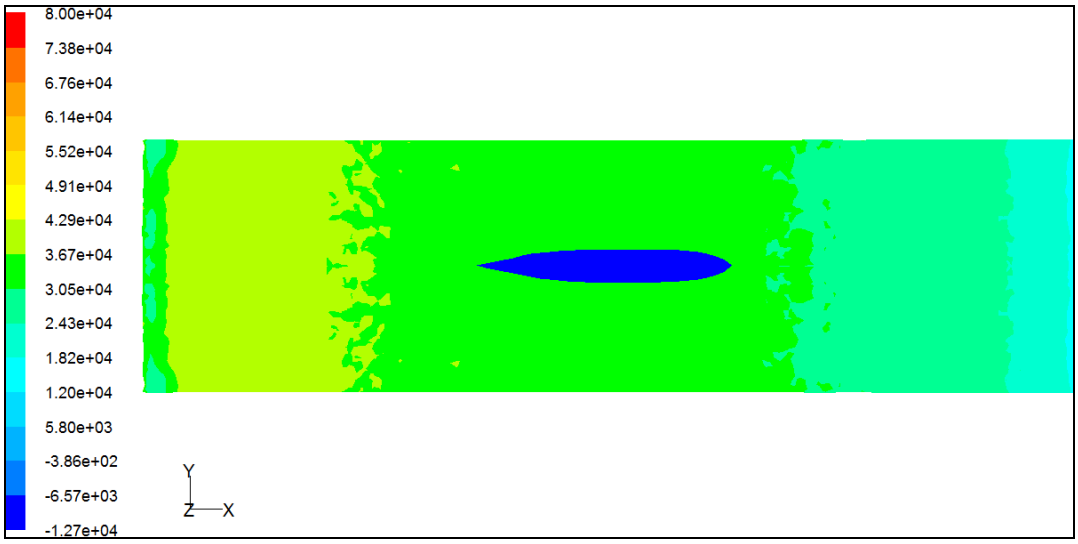
8.00e+04
7.38e+04
6.76e+04
6.14e+04
5.52e+04
4.91e+04
4.29e+04
3.67e+04
3.05e+04
2.43e+04
1.82e+04
1.20e+04
5.80e+03
-3.86e+02
-6.57e+03
-1.27e+04
Y
Z
X

(b)

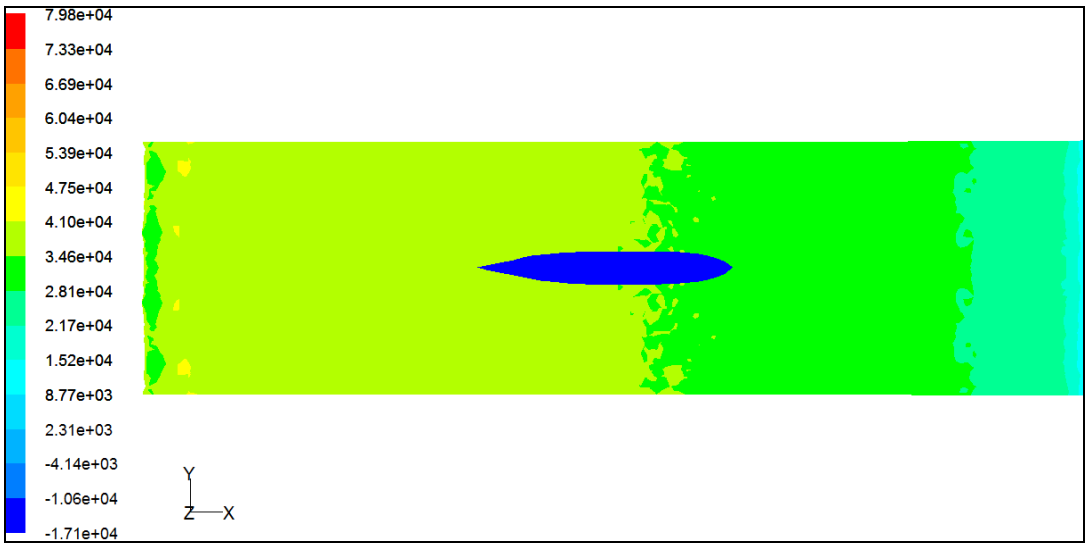
7.98e+04
7.33e+04
6.69e+04
6.04e+04
5.39e+04
4.75e+04
4.10e+04
3.46e+04
2.81e+04
2.17e+04
1.52e+04
8.77e+03
2.31e+03
-4.14e+03
-1.06e+04
-1.71e+04
Y
Z
X

(c)

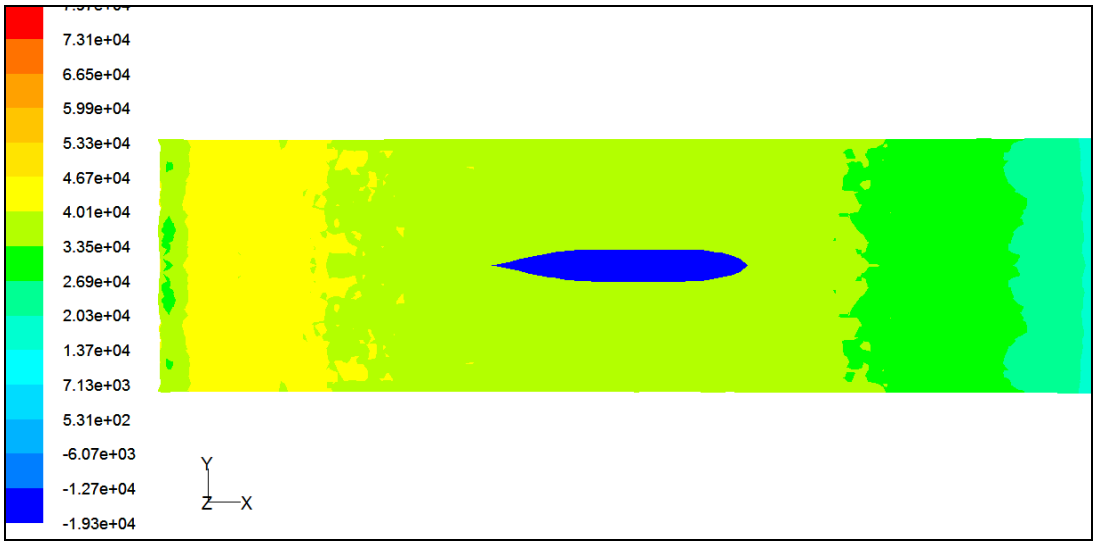

(d)

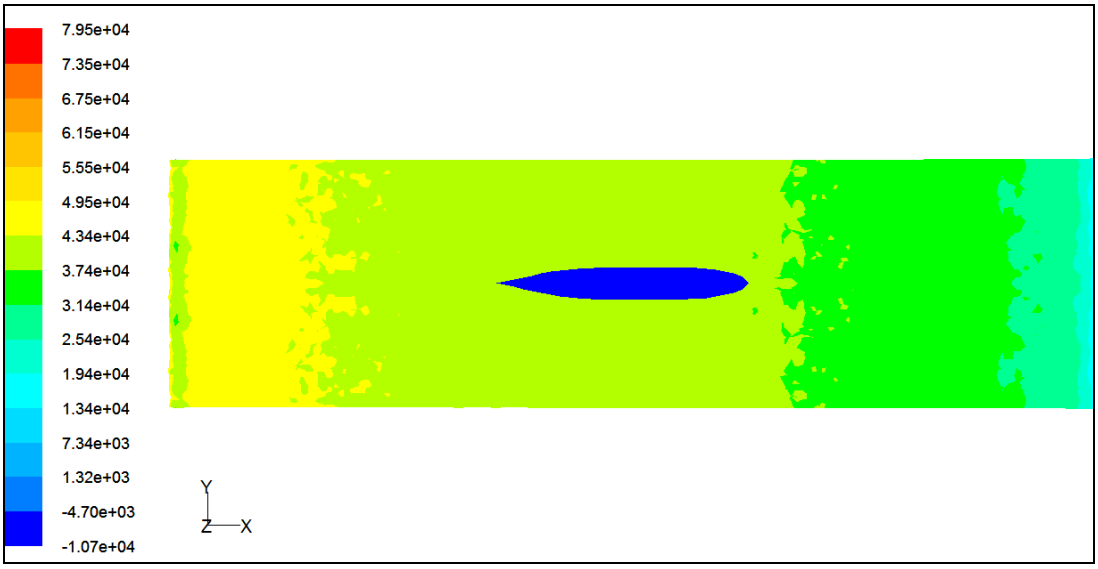

(e)

Figures 5.28: Contours of Pressure Coefficient of Series 60 Hull and its Free Surface for a)Fn = 0.173,b)Fn = 0.205, c) Fn = 0.267,d) Fn = 0.355 and e) Fn = 0.476.

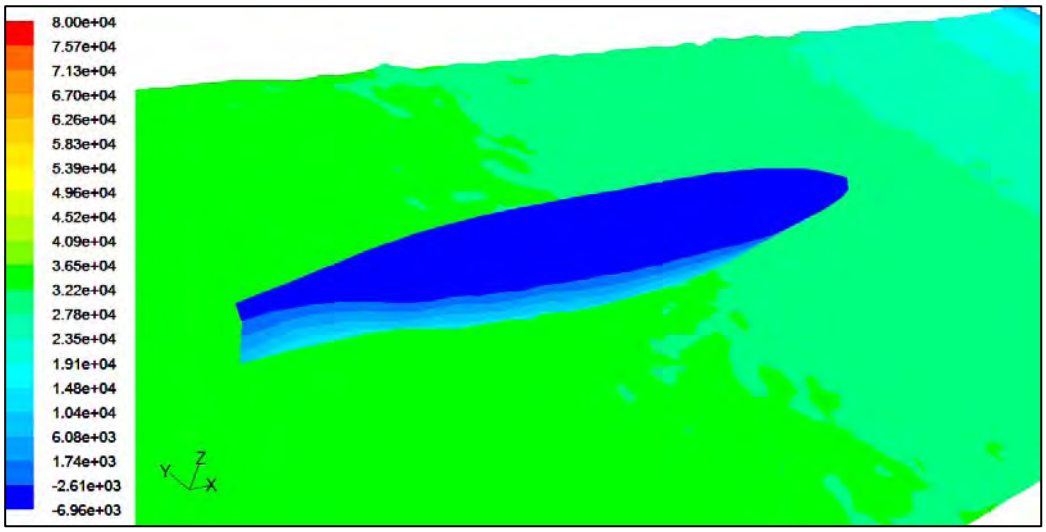
8.00e+04
7.57e+04
7.13e+04
6.70e+04
6.26e+04
5.83e+04
5.39e+04
4.96e+04
4.52e+04
4.09e+04
3.65e+04
3.22e+04
2.78e+04
2.35e+04
1.91e+04
1.48e+04
1.04e+04
6.08e+03
1.74e+03
-2.61e+03
-6.96e+03
Y
Z
X

(a)

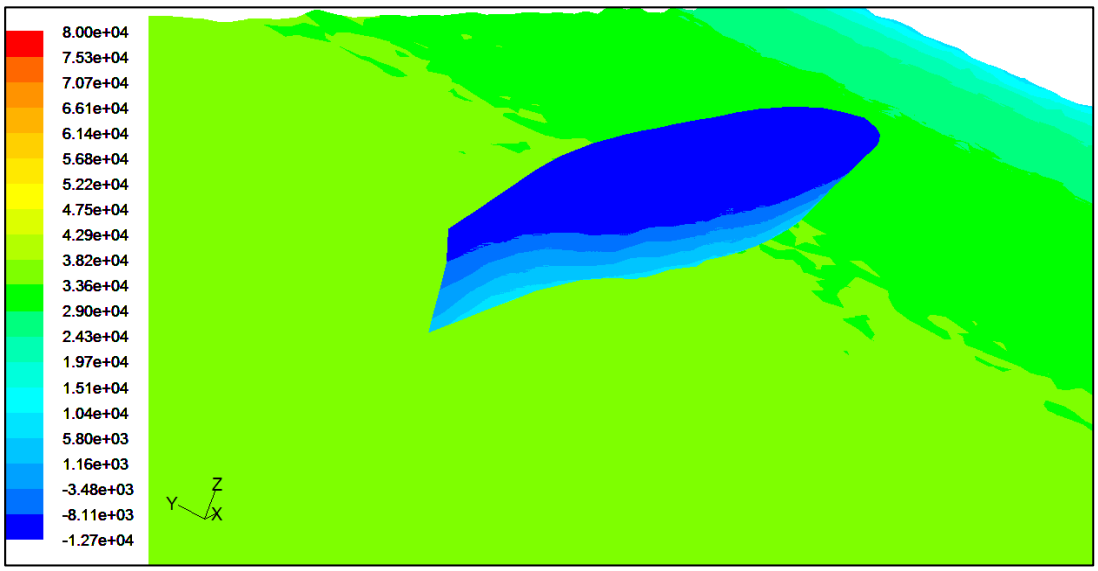
8.00e+04
7.53e+04
7.07e+04
6.61e+04
6.14e+04
5.68e+04
5.22e+04
4.75e+04
4.29e+04
3.82e+04
3.36e+04
2.90e+04
2.43e+04
1.97e+04
1.51e+04
1.04e+04
5.80e+03
1.16e+03
-3.48e+03
-8.11e+03
-1.27e+04
Y
Z
X

(b)

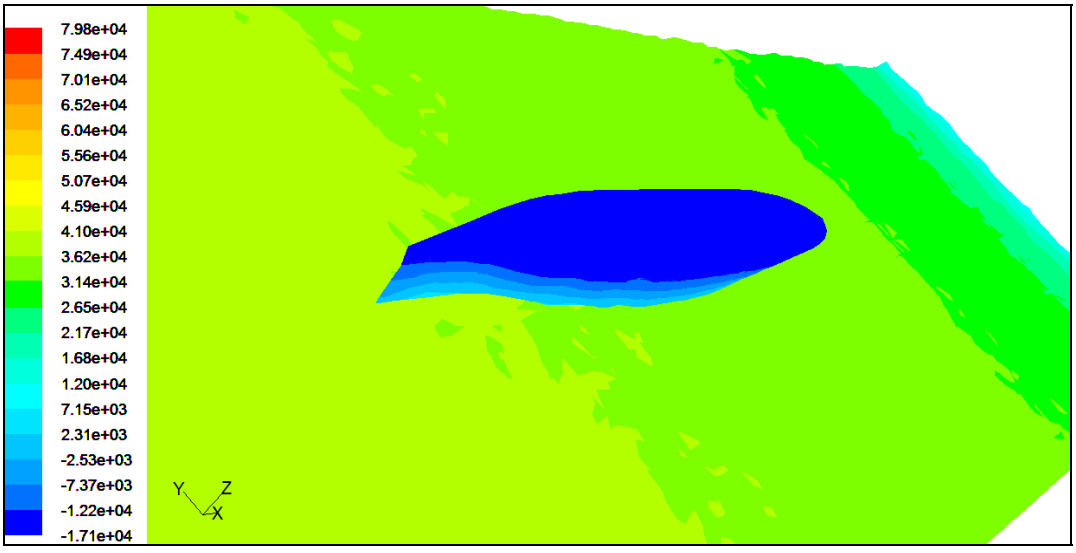
7.98e+04
7.49e+04
7.01e+04
6.52e+04
6.04e+04
5.56e+04
5.07e+04
4.59e+04
4.10e+04
3.62e+04
3.14e+04
2.65e+04
2.17e+04
1.68e+04
1.20e+04
7.15e+03
2.31e+03
-2.53e+03
-7.37e+03
-1.22e+04
-1.71e+04
Y
Z
X

(c)

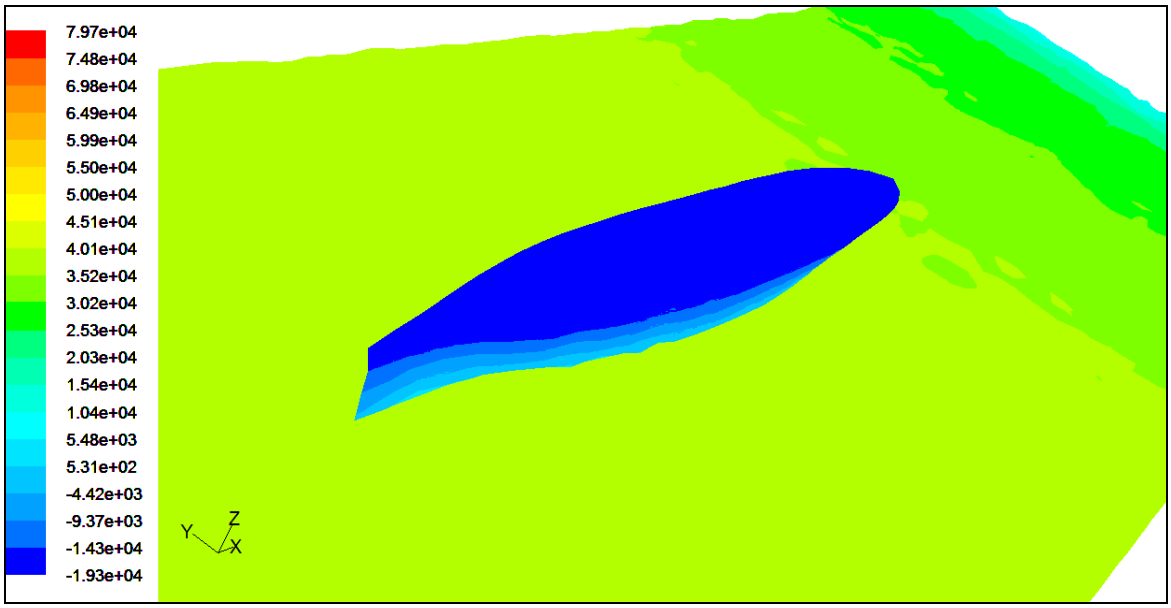

(d)

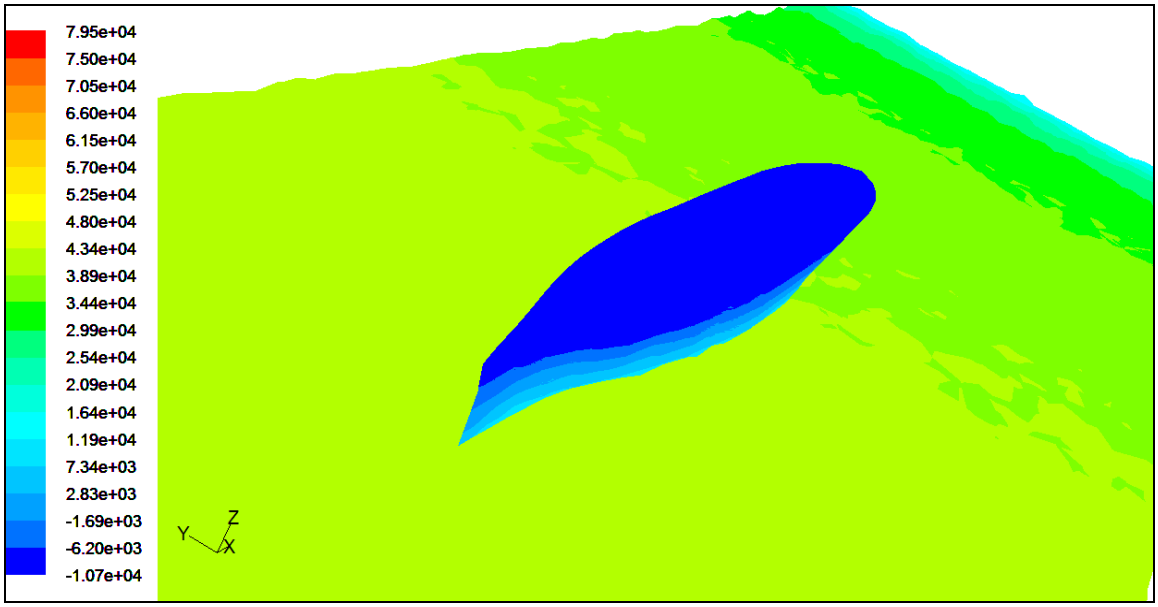

(e)

Figures 5.29: Close Up View of Contours of Pressure Coefficient of Series 60 Hull and its Free Surface for a)Fn = 0.173,b)Fn = 0.205, c) Fn = 0.267, d) Fn = 0.355 and e) Fn = 0.476.

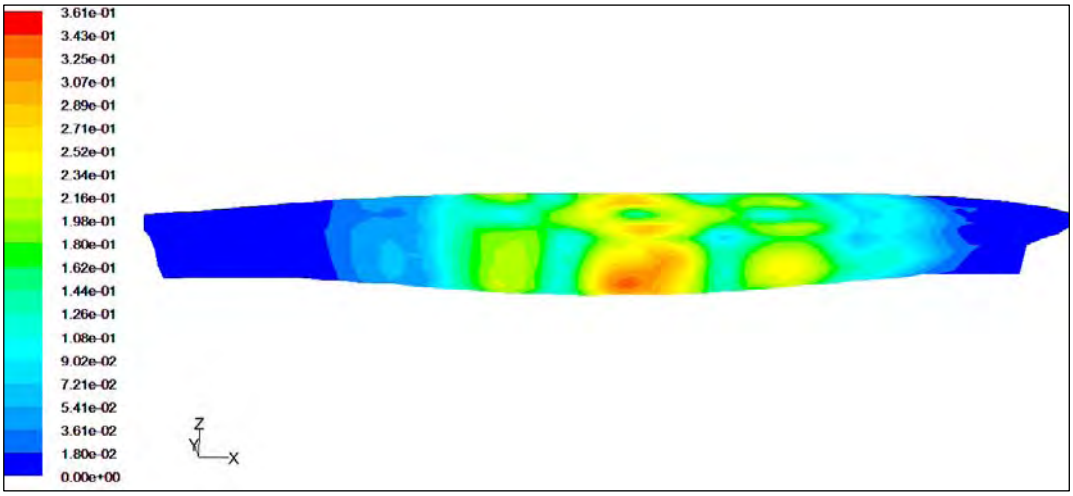
3.61e-01
3.43e-01
3.25e-01
3.07e-01
2.89e-01
2.71e-01
2.52e-01
2.34e-01
2.16e-01
1.98e-01
1.80e-01
1.62e-01
1.44e-01
1.26e-01
1.08e-01
9.02e-02
7.21e-02
5.41e-02
3.61e-02
1.80e-02
0.00e+00
Z
Y
X

(a)

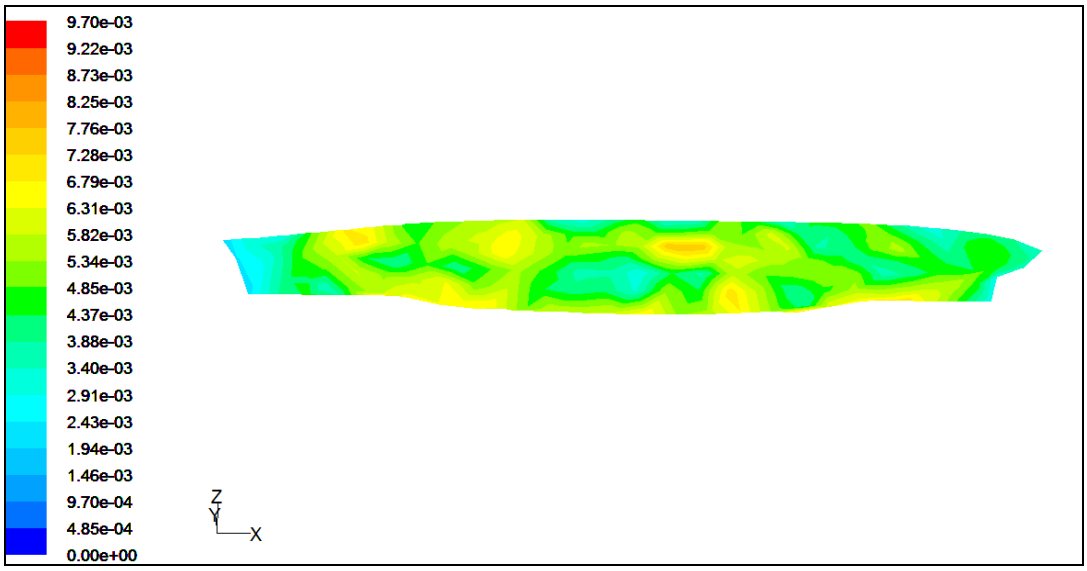
9.70e-03
9.22e-03
8.73e-03
8.25e-03
7.76e-03
7.28e-03
6.79e-03
6.31e-03
5.82e-03
5.34e-03
4.85e-03
4.37e-03
3.88e-03
3.40e-03
2.91e-03
2.43e-03
1.94e-03
1.46e-03
9.70e-04
4.85e-04
0.00e+00
Z
Y
X

(b)

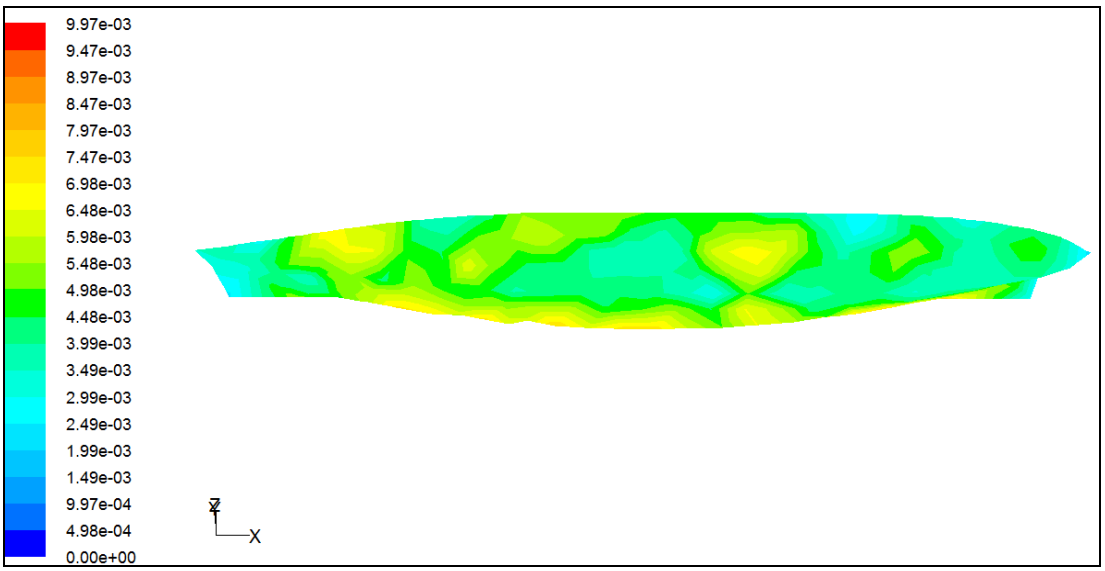
9.97e-03
9.47e-03
8.97e-03
8.47e-03
7.97e-03
7.47e-03
6.98e-03
6.48e-03
5.98e-03
5.48e-03
4.98e-03
4.48e-03
3.99e-03
3.49e-03
2.99e-03
2.49e-03
1.99e-03
1.49e-03
9.97e-04
4.98e-04
0.00e+00
Z
X

(c)

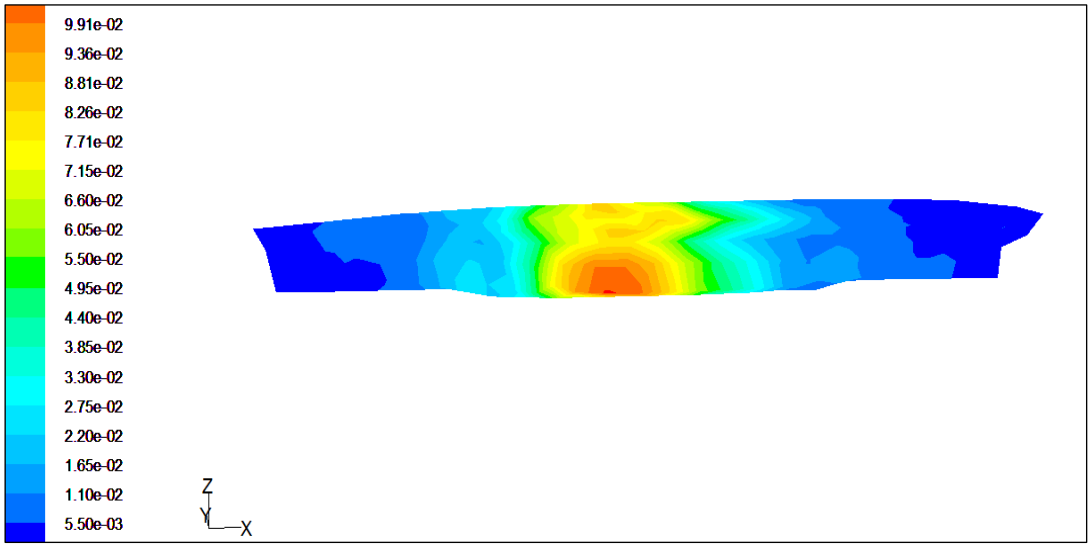

(d)

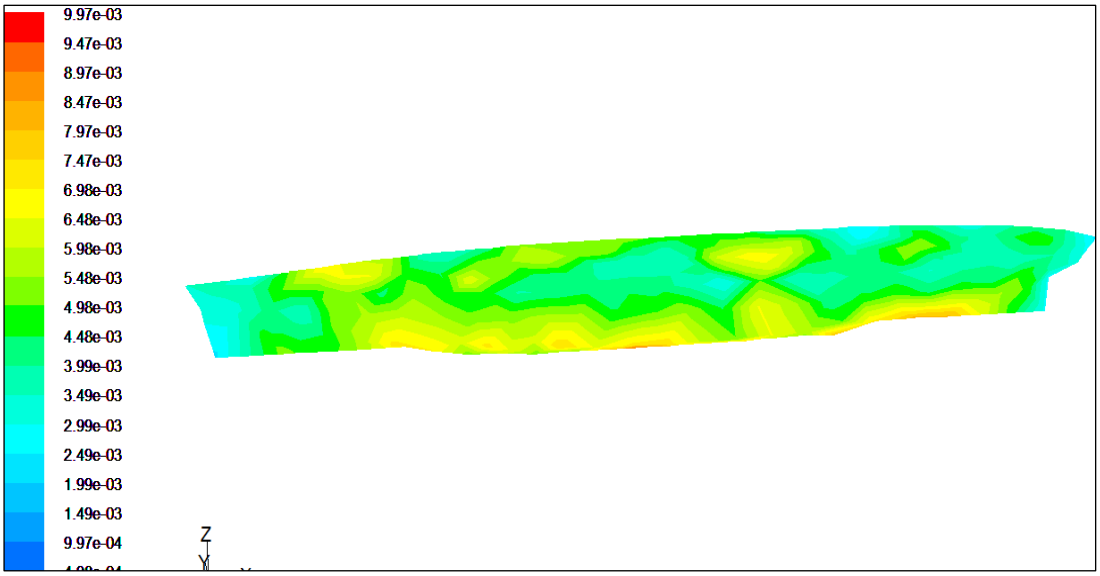

(e)

Figures 5.30: Contours of Wall Y+ of Series 60 Hull for
a)Fn = 0.173,b)Fn = 0.205, c) Fn = 0.267,
d) Fn = 0.355 and e) Fn = 0.476.

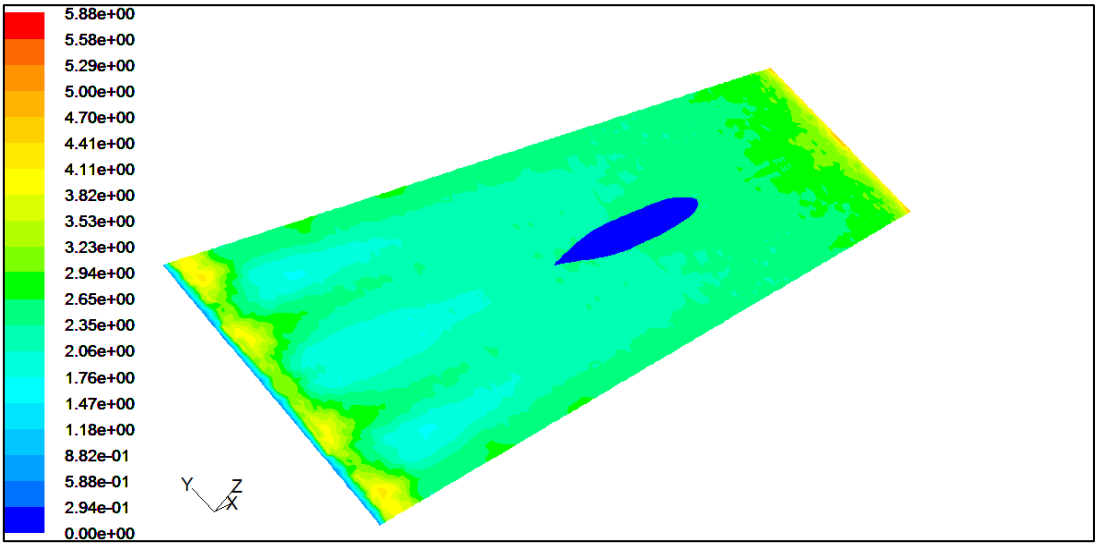
5.88e+00
5.58e+00
5.29e+00
5.00e+00
4.70e+00
4.41e+00
4.11e+00
3.82e+00
3.53e+00
3.23e+00
2.94e+00
2.65e+00
2.35e+00
2.06e+00
1.76e+00
1.47e+00
1.18e+00
8.82e-01
5.88e-01
2.94e-01
0.00e+00
Y
Z
X

(a)

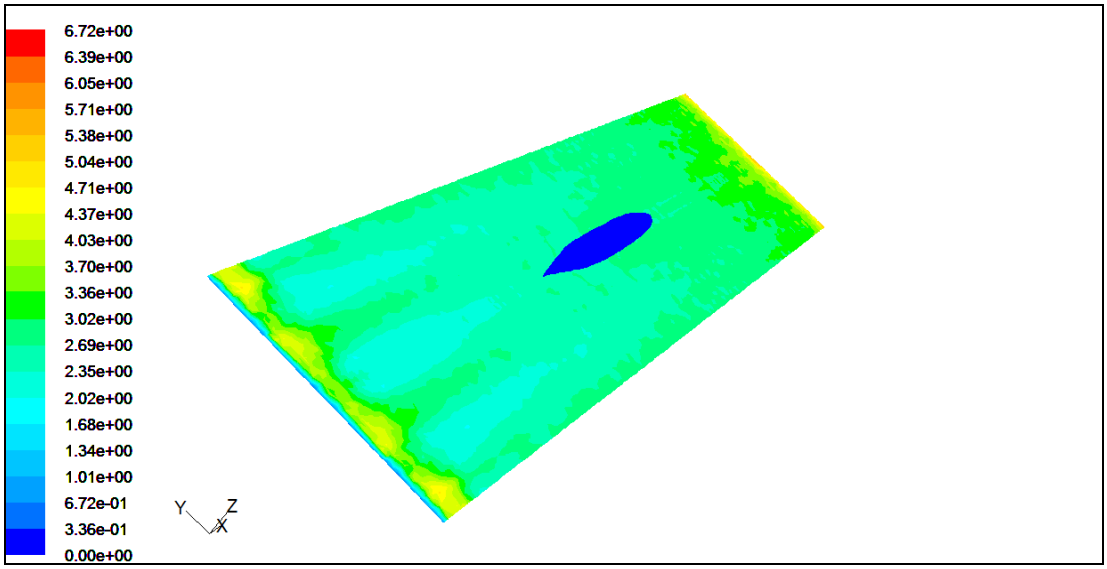
6.72e+00
6.39e+00
6.05e+00
5.71e+00
5.38e+00
5.04e+00
4.71e+00
4.37e+00
4.03e+00
3.70e+00
3.36e+00
3.02e+00
2.69e+00
2.35e+00
2.02e+00
1.68e+00
1.34e+00
1.01e+00
6.72e-01
3.36e-01
0.00e+00
Y
Z
X

(b)

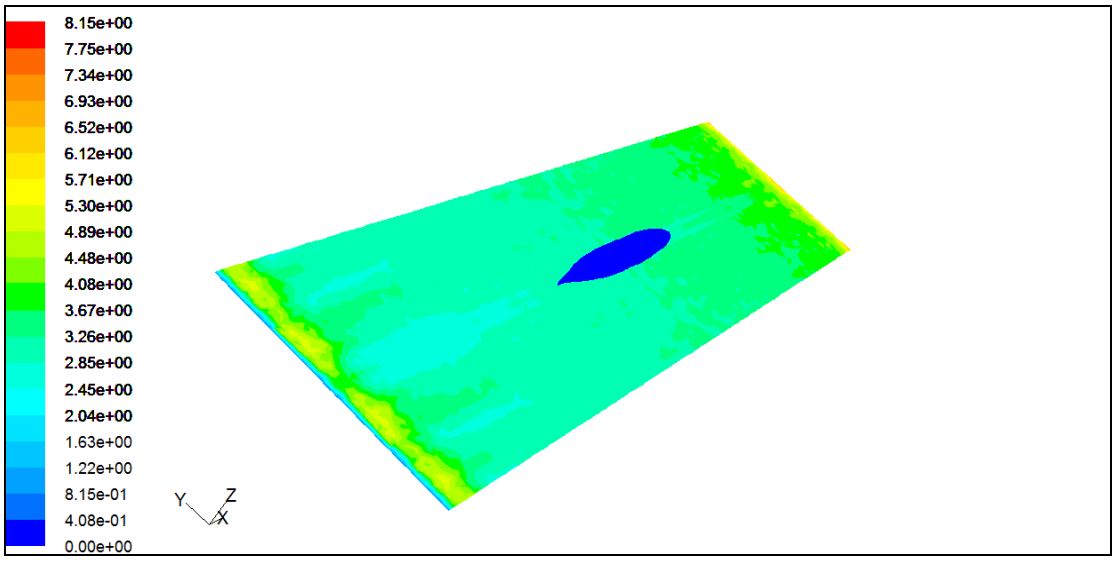
8.15e+00
7.75e+00
7.34e+00
6.93e+00
6.52e+00
6.12e+00
5.71e+00
5.30e+00
4.89e+00
4.48e+00
4.08e+00
3.67e+00
3.26e+00
2.85e+00
2.45e+00
2.04e+00
1.63e+00
1.22e+00
8.15e-01
4.08e-01
0.00e+00
Y
Z
X

(c)

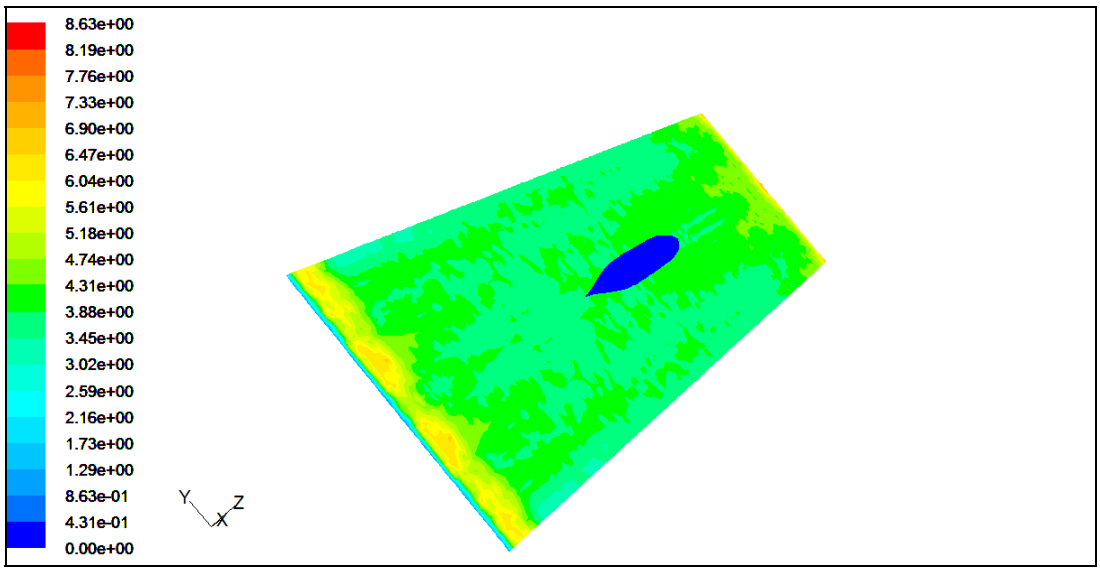

(d)

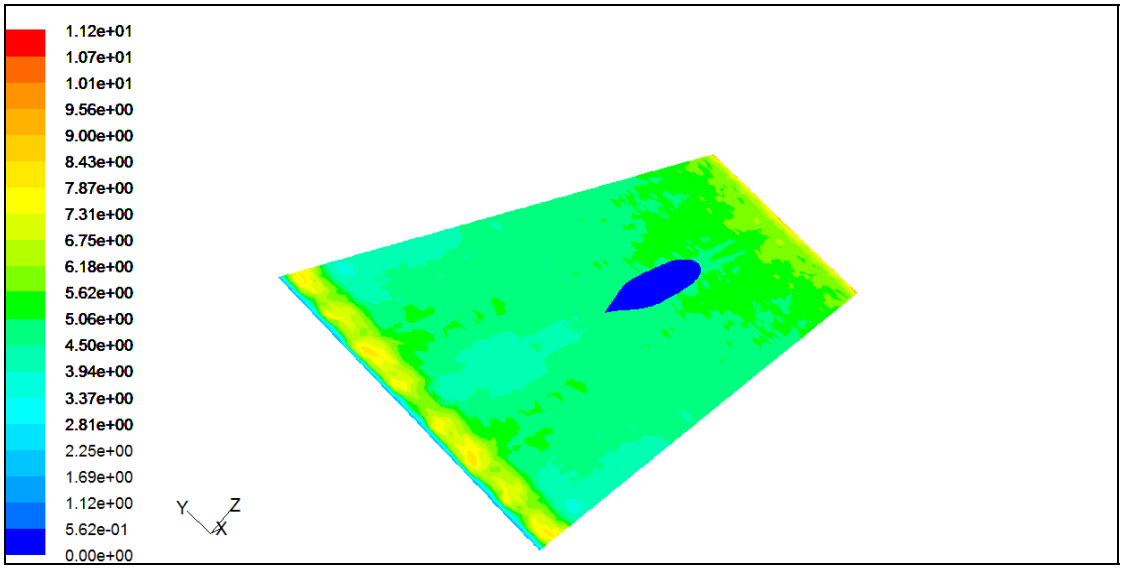

(e)

Figures 5.31: Contours of Velocity Magnitude of Series 60 Hull and the Reference Surface for a)Fn = 0.173,b)Fn = 0.205, c) Fn = 0.267, d) Fn = 0.355 and e) Fn = 0.476.

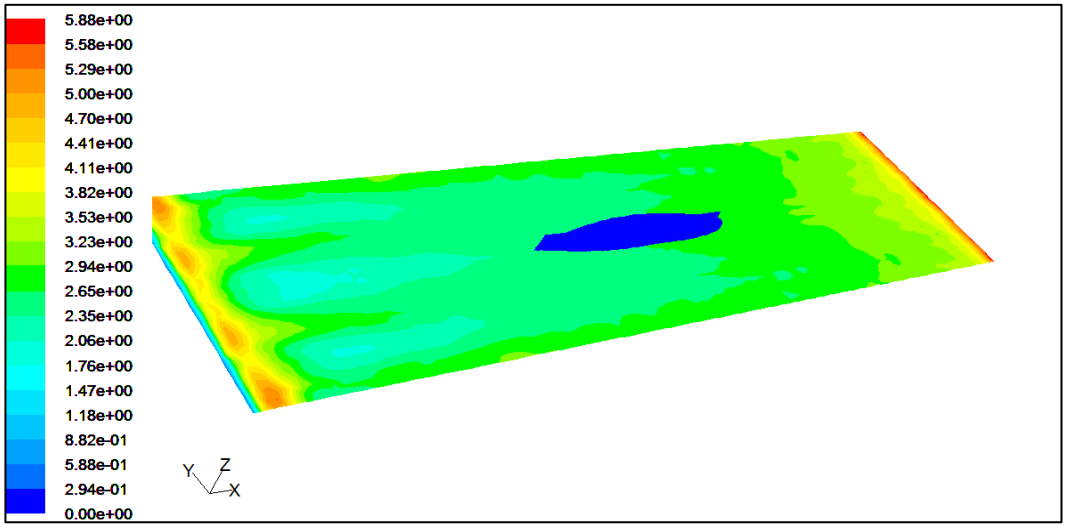
5.88e+00
5.58e+00
5.29e+00
5.00e+00
4.70e+00
4.41e+00
4.11e+00
3.82e+00
3.53e+00
3.23e+00
2.94e+00
2.65e+00
2.35e+00
2.06e+00
1.76e+00
1.47e+00
1.18e+00
8.82e-01
5.88e-01
2.94e-01
0.00e+00
Y
Z
X

(a)

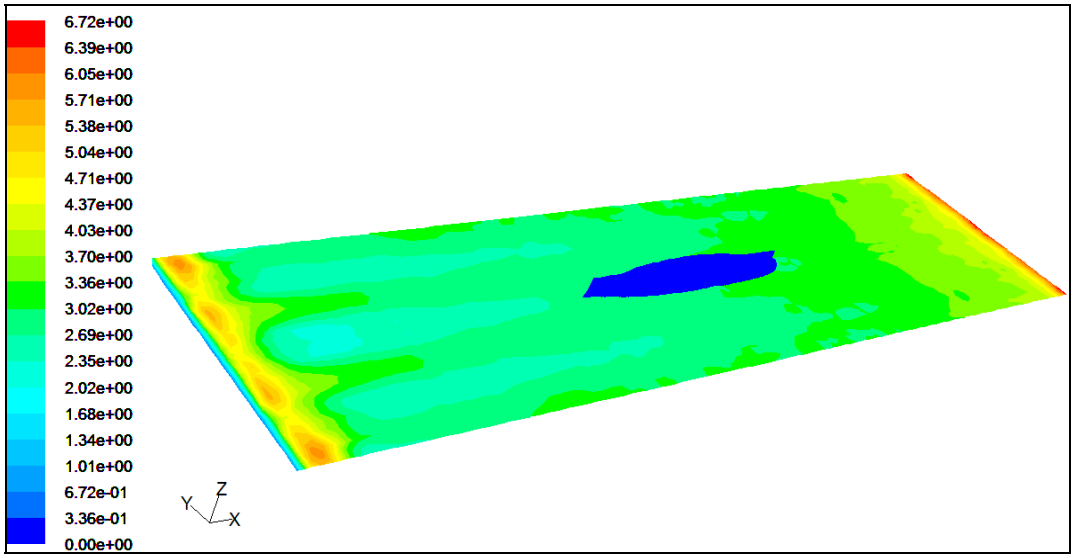
6.72e+00
6.39e+00
6.05e+00
5.71e+00
5.38e+00
5.04e+00
4.71e+00
4.37e+00
4.03e+00
3.70e+00
3.36e+00
3.02e+00
2.69e+00
2.35e+00
2.02e+00
1.68e+00
1.34e+00
1.01e+00
6.72e-01
3.36e-01
0.00e+00
Y
Z
X

(b)

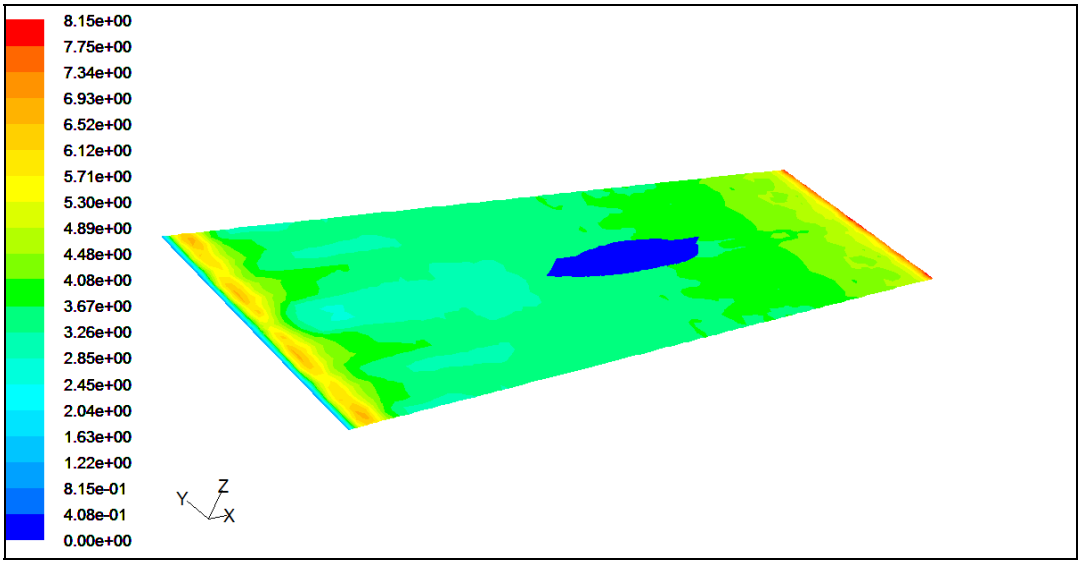
8.15e+00
7.75e+00
7.34e+00
6.93e+00
6.52e+00
6.12e+00
5.71e+00
5.30e+00
4.89e+00
4.48e+00
4.08e+00
3.67e+00
3.26e+00
2.85e+00
2.45e+00
2.04e+00
1.63e+00
1.22e+00
8.15e-01
4.08e-01
0.00e+00
Y
Z
X

(c)

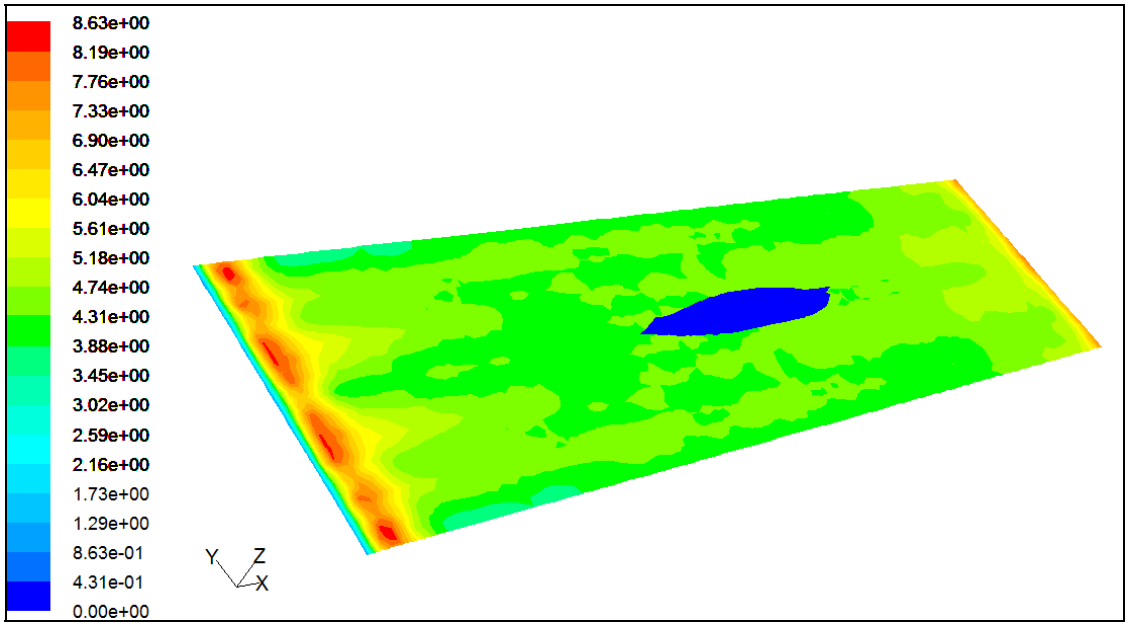

(d)

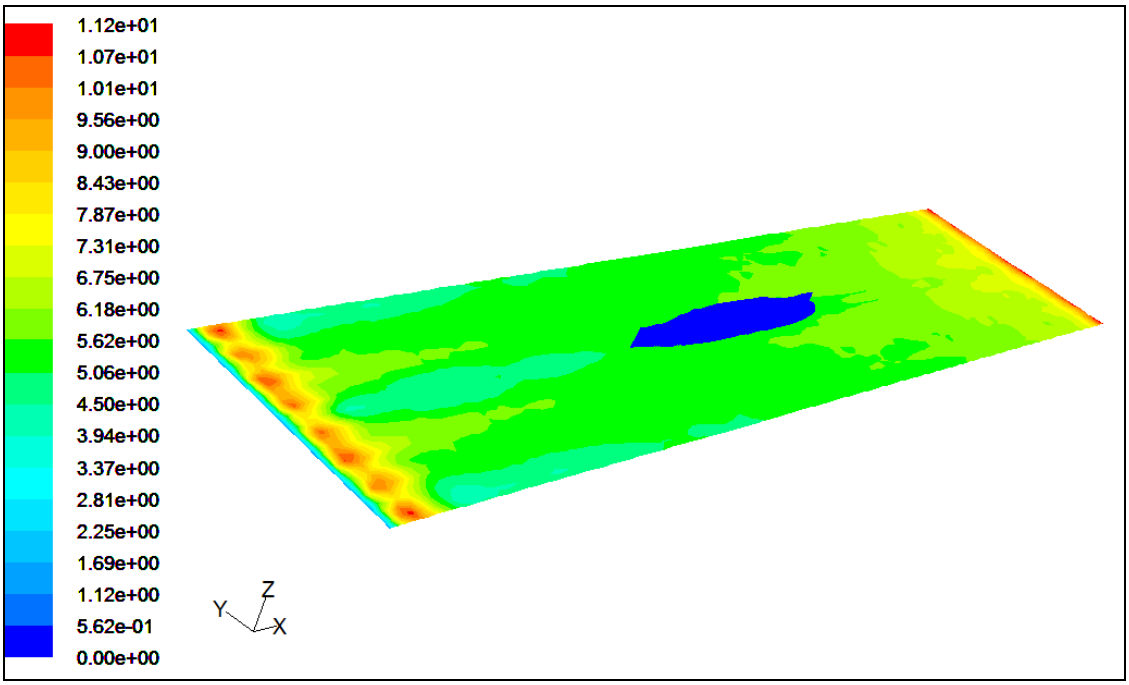

(e)

Figures 5.32: Contours of Velocity Magnitude of Series 60 Hull and Symmetric top Side of the Volume for a)Fn = 0.173,b)Fn = 0.205, c) Fn = 0.267,d) Fn = 0.355 and e) Fn = 0.476.

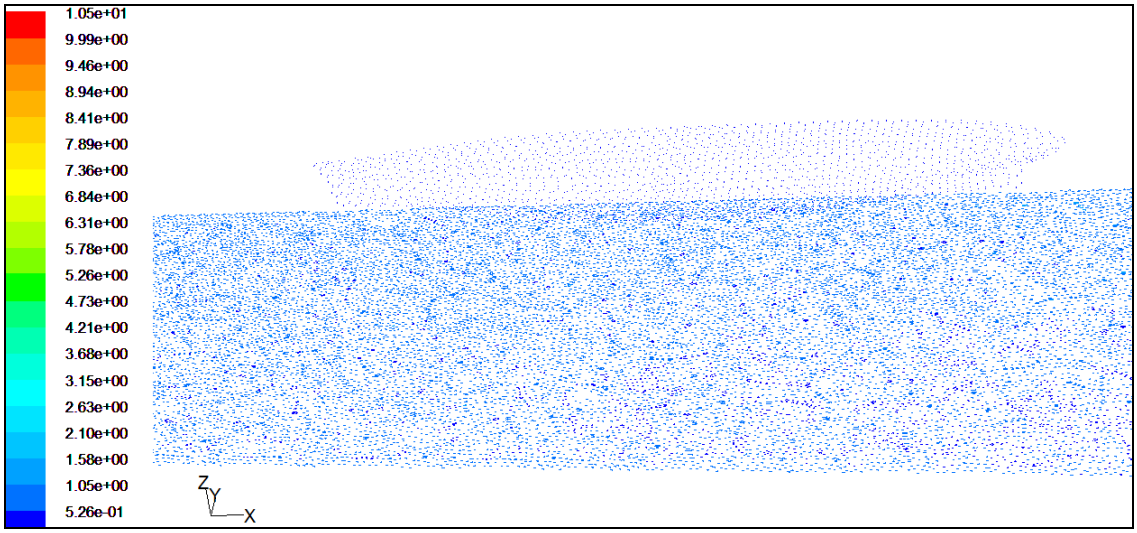
1.05e+01
9.99e+00
9.46e+00
8.94e+00
8.41e+00
7.89e+00
7.36e+00
6.84e+00
6.31e+00
5.78e+00
5.26e+00
4.73e+00
4.21e+00
3.68e+00
3.15e+00
2.63e+00
2.10e+00
1.58e+00
1.05e+00
5.26e-01
Z
Y
X

(a)

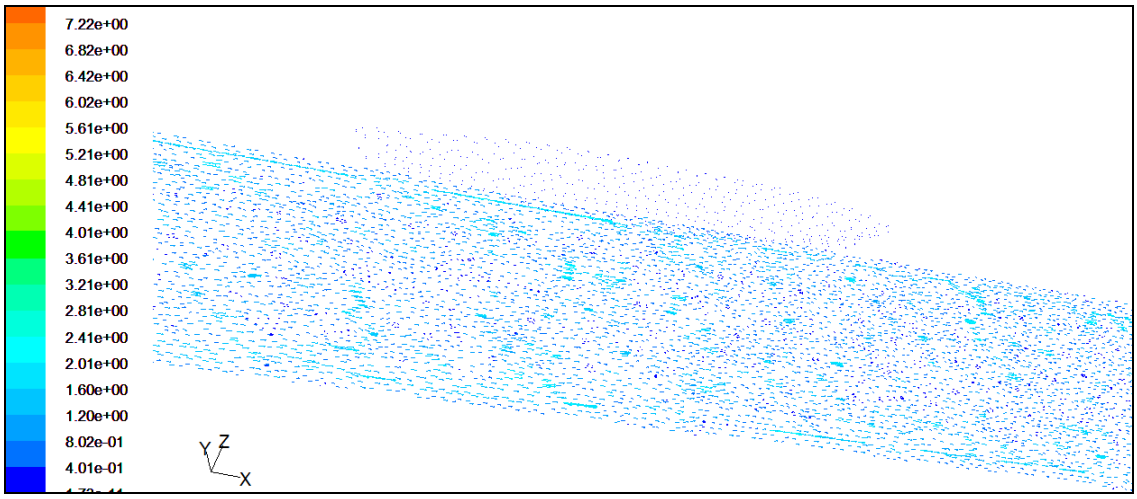
7.22e+00
6.82e+00
6.42e+00
6.02e+00
5.61e+00
5.21e+00
4.81e+00
4.41e+00
4.01e+00
3.61e+00
3.21e+00
2.81e+00
2.41e+00
2.01e+00
1.60e+00
1.20e+00
8.02e-01
4.01e-01
Y
Z
X

(b)

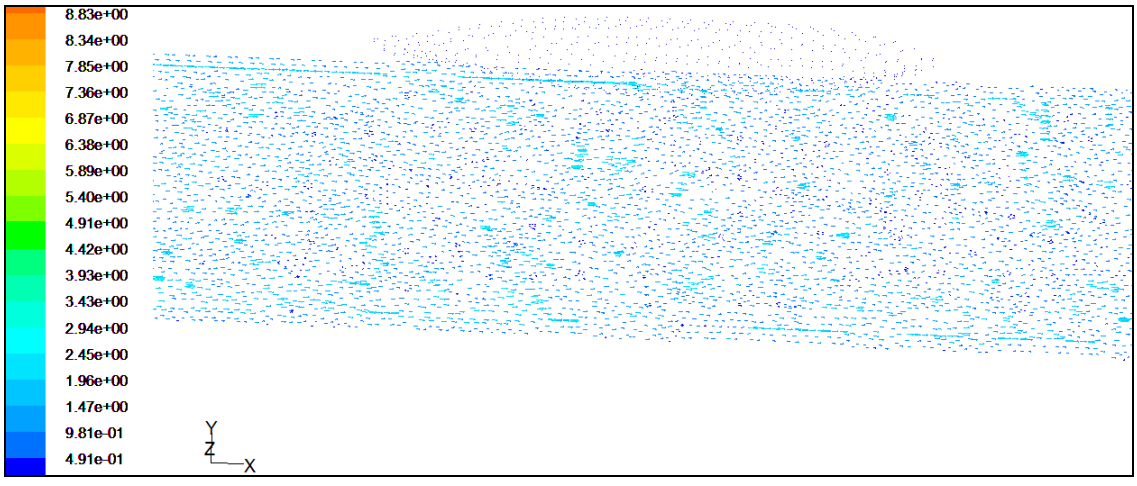
8.83e+00
8.34e+00
7.85e+00
7.36e+00
6.87e+00
6.38e+00
5.89e+00
5.40e+00
4.91e+00
4.42e+00
3.93e+00
3.43e+00
2.94e+00
2.45e+00
1.96e+00
1.47e+00
9.81e-01
4.91e-01
Y
Z
X

(c)

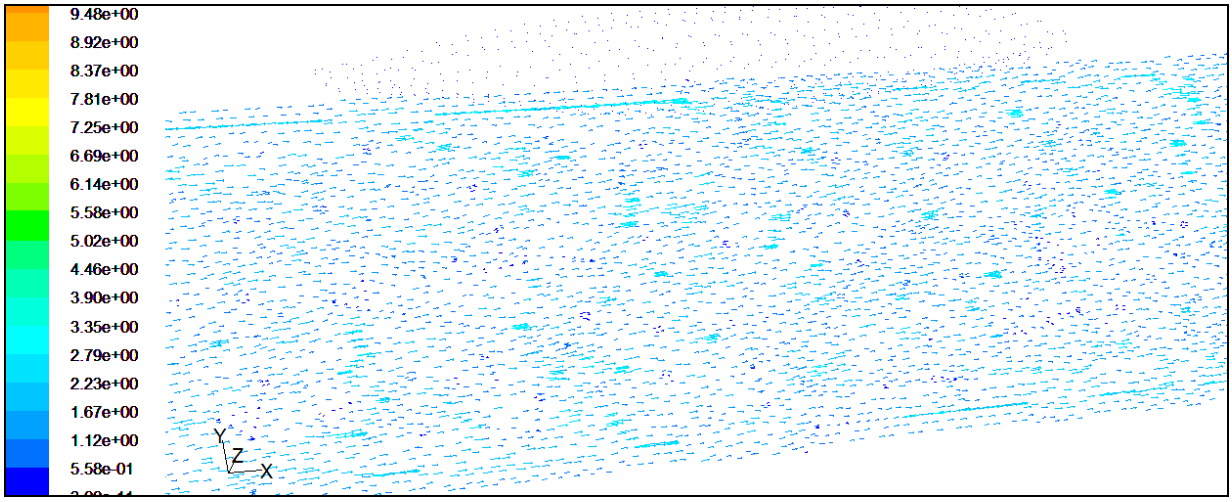

(d)

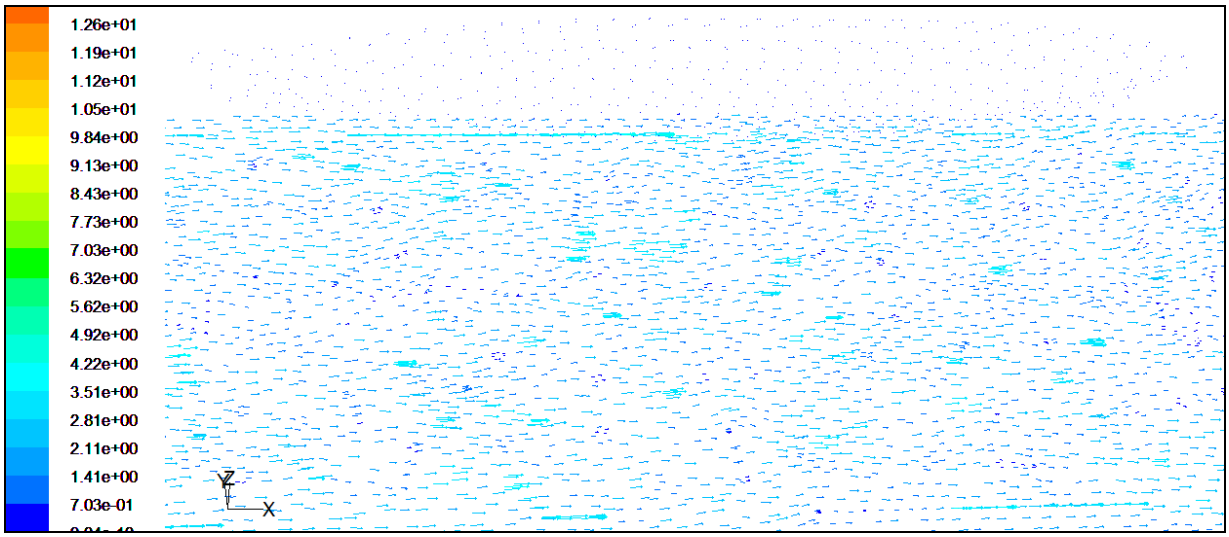

(e)

Figures 5.33: Contours of Velocity Vectors of Series 60 Hull and the Reference Surface for a)Fn = 0.173,b)Fn = 0.205, c) Fn = 0.267,d) Fn = 0.355 and e) Fn = 0.476.

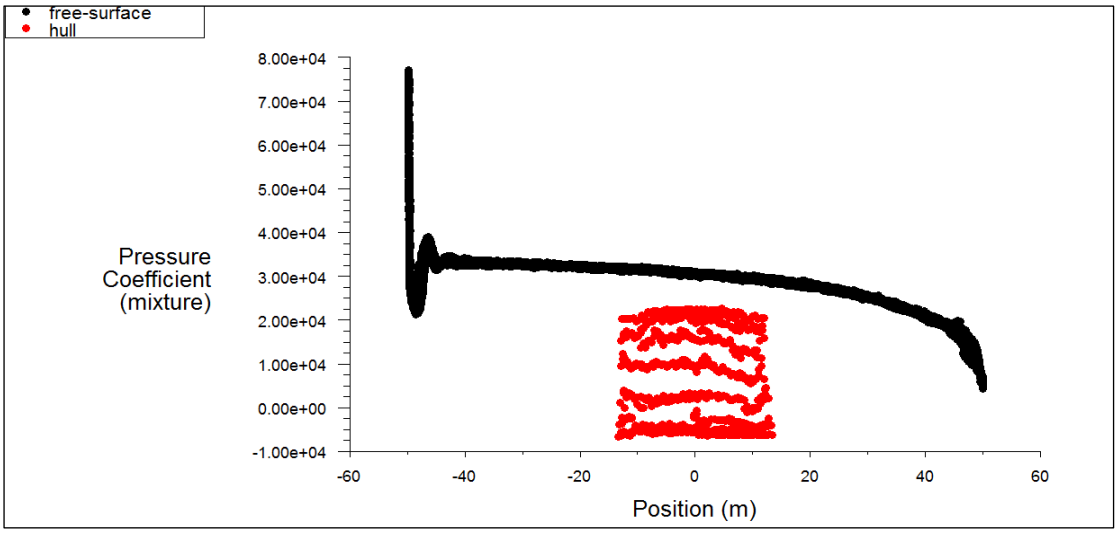
free-surface
hull
Pressure Coefficient (mixture)
8.00e+04
7.00e+04
6.00e+04
5.00e+04
4.00e+04
3.00e+04
2.00e+04
1.00e+04
0.00e+00
-1.00e+04
-60
-40
-20
0
20
40
60
Position (m)

(a)

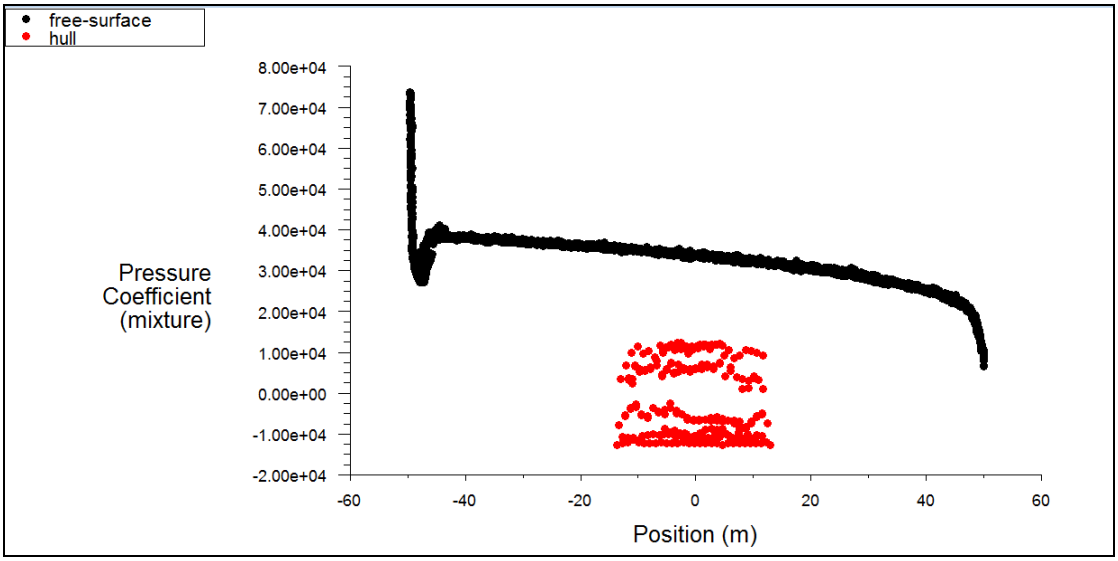
free-surface
hull
Pressure Coefficient (mixture)
8.00e+04
7.00e+04
6.00e+04
5.00e+04
4.00e+04
3.00e+04
2.00e+04
1.00e+04
0.00e+00
-1.00e+04
-2.00e+04
-60
-40
-20
0
20
40
60
Position (m)

(b)

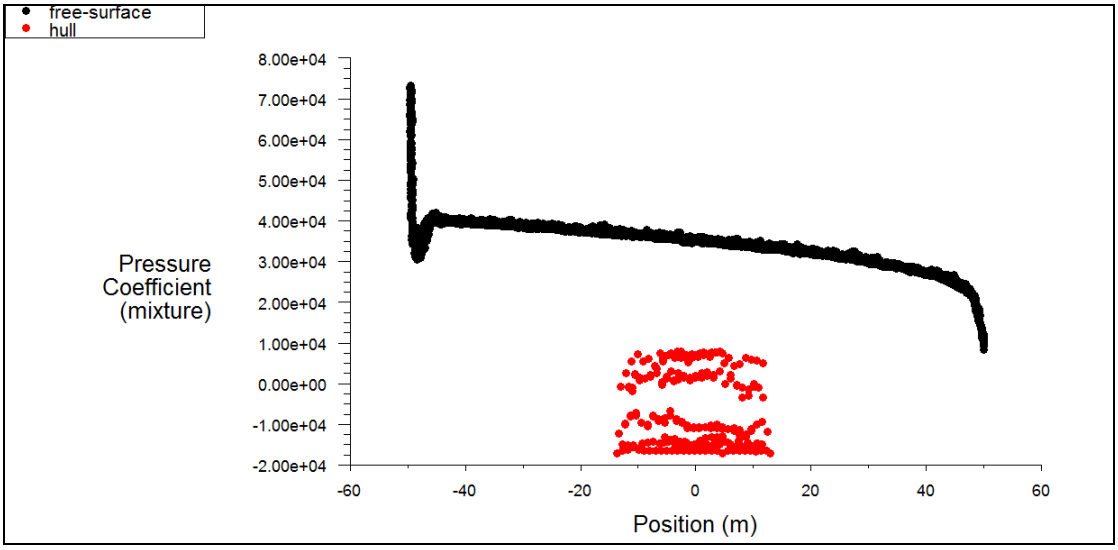
free-surface
hull
Pressure Coefficient (mixture)
8.00e+04
7.00e+04
6.00e+04
5.00e+04
4.00e+04
3.00e+04
2.00e+04
1.00e+04
0.00e+00
-1.00e+04
-2.00e+04
-60
-40
-20
0
20
40
60
Position (m)

(c)

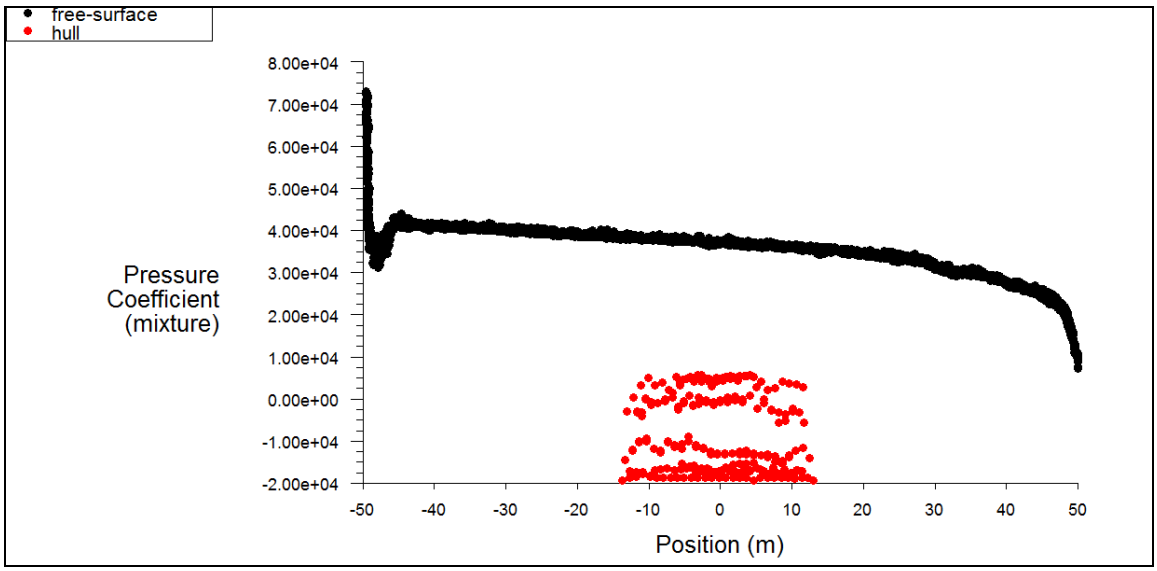

(d)

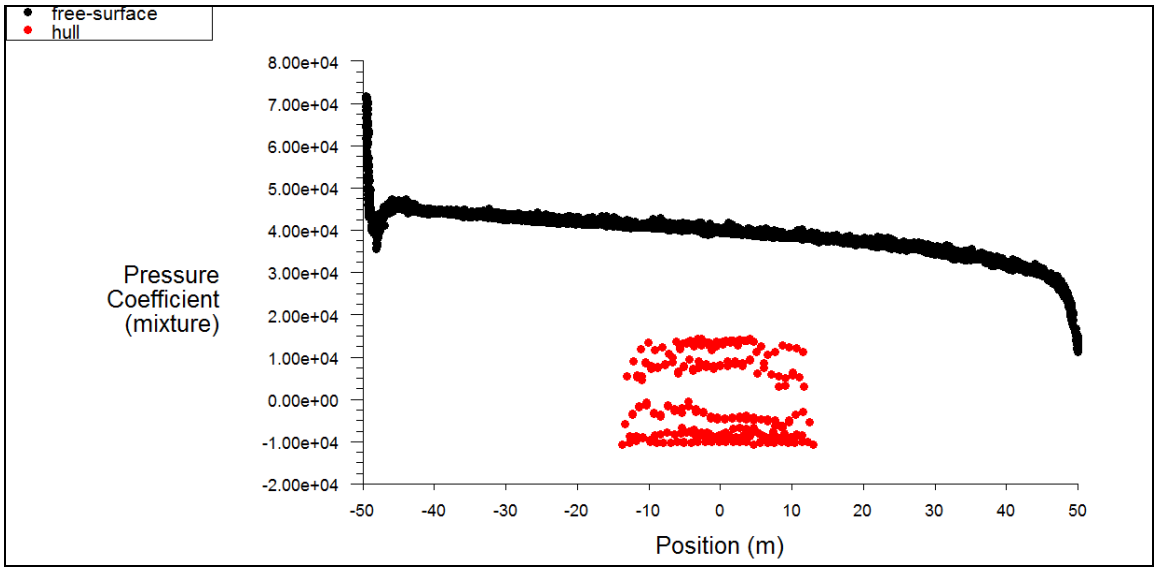

(e)

Figures 5.34: Plot of Pressure Co-Efficient of Series 60 Hull and its Free Surface for a) Fn = 0.173,b)Fn = 0.205, c) Fn = 0.267,d) Fn = 0.355 and e) Fn = 0.476.

CHAPTER 6

6. CONCLUSION AND RECOMMENDATIONS

6.1 Conclusion

Three-dimensional finite volume method has been applied to simulate incompressible flow around Wigley parabolic and Series 60 hull using CFD software FLUENT 6.3.26. From the above study, following conclusions can be drawn:

1) Finite volume method is very much prospective for simulation of flow around ship in both hexahedral and tetrahedral grid resolution.
2) Three turbulence models such as Standard k-ε, Realizable k-ε with standard wall functions and Shear Stress Transport (SST) k-ω models are used to capture boundary layer in the simulation of steady flow around hulls in viscous turbulent flow. It is observed that the Standard k-ε model with standard wall functions compute the drag coefficient accurately. However, only SST k-ω model with transitional flow is used for simulation of turbulent flow because of its better performance.
3) In this research the Volume of Fluid (VOF) method implemented in the RANS software FLUENT is employed to determine the free-surface wave flow around the Wigely parabolic hull advancing in calm water. Particular care was given to the grid generation to avoid problems of reflection of the waves and to minimize the computational efforts. It was shown that the convergence can be improved by increasing the density ratio between air and water without any relevant lack of accuracy in both free-surface and resistance predictions.
4) Both the Standard k-ε and the SST k-ω turbulence models gave similar results concerning the coefficient of total resistance calculation for the Wigely parabolic hull form. Variation of result appeared in the case of Series 60 hull when the Froude number Fn > 0.3. This variation can be minimized by changing the mesh size, refining mesh and using super computers like SGI 900,8 processor. Based on the results of a CFD simulation, a ship designer can

choose optimum speed with minimum power and then proceed to a model test for experimental result.

5) The numerical model based on SIMPLE algorithm, associated with two different single hulls is used to simulate turbulent flow at different Reynolds number from $5.3x10^6$ from $1.48x10^7$. The computed value of drag coefficient agrees satisfactorily with experimental results. In this case, the viscous coefficient is 2.975% of the total drag coefficient of the hull. The flow is very well predicted by k-ε turbulence model.
6) Particulars importance is attached to the grid topology for the RANS simulation to minimize computational efforts without any lack of accuracy of the numerical solution. Indeed, all the computations presented here are carried out on a dual core processor personal computer avoiding expensive hardware.

6.2 Recommendation for further study

Following are recommendations for further study:

(i) In this study, although three-dimensional model is used for a single hull however three dimensional models also can be used in multihull models and for a full scale model like a ship.
(ii) This research is restricted only to measure drag coefficients with free surface effects. This may be done to show the effects of sinkage and trim with different angle of attack.
(iii) More study may be done to model the laminar-to-turbulent flow transition.
(iv) The unsteady turbulent flow with other viscous models like Spalart-Allmaras, Reynolds Stress models can also be considered.
(v) Wave profile and wave pattern along the two shapes of hulls may be investigated.
(vi) More study may be done to model the laminar-to-turbulent flow transition.

REFERENCE

Alza, P.I., Rojas,L.P.and Basanez, J.F.N., “Drag Reduction Through Special Paints Coated on the Wall” , International Conference on Ship Drag Reduction,20-21 May,2010.

Anon.,Co-operative experiment on Wigely Parabolic Models in Japan,17th ITTC Resistance Committee Report,, University of Tokyo,1983.

Azcueta, R., “ Ship Resistance Prediction by Free-Surface RANS Computation”, Ship Technology Research,Vol.47, No.2, pp. 47-62,TU Hamburg, 2000.

Banawan, A. A. and Ahmed, Y. M., “ Use of Computational Fluid Dynamics for The Calculation of Ship Résistance, and Its Variation with The Ship Hull Form Parameters”,Alexandria Engineering Journal, Vol. 45, No.1, 2006.

Fluent Inc., FLUENT 6.2 User’s Guide, 2005.

Fonfach, J. M. A. and Soares, C. G., Improving The Resistance of a Series 60 Vessel with CFD CODE”, European Conference on Computational Fluid Dynamics, ECCOMAS CFD 2010, Lisbon, Portugal, 14–17 June 2010.

Gray, A. W., Preliminary Study on The Use of Computational Fluid Dynamics to Determine The Frictional Resistance of a Trimaran Ship, M.S thesis, Department of Mechanical and Aerospace Engineering, West Virginia University, Morgantown, USA, 2007.

Hino, T. (ed.), “Proceedings of the CFD Workshop Tokyo 2005”, Tokyo, Japan, 2005.

Hirt, C.W. and Nichols, B. D., “Volume of Fluid (VOF) Method for the Dynamics of Free Boundaries”, Journal of Computational Physics,Vol.39,pp201-225,1981.

http://www.cfd-online.com/Wiki/Turbulence_modeling

Jones , D.A. and Clarke , D.B., “Fluent Code Simulation of Flow around a Naval Hull: The DTMB 5415”, Maritime Platforms Division, Defence Science and Technology Organisation, Australian Government, Department of Defence,2010.

Jones , D.A. and Clarke , D.B., “Simulation of Flow Past a Sphere using the Fluent Code”, Maritime Platforms Division, Defence Science and Technology Organisation,Australian Government,Department of Defence, 2008.

Kodoma,Y. ,Takeshi, H., Hinatsu,M., Hino, T.,Uto,S., Hirata,N. and MurashigeS., "Proceedings of the 1994 CFD Workshop",Ship Research Institute,Japan,1994.

Larsson, L., Pate l, V. C. and Dyne ,G.,(Eds.) "Ship Viscous Flow-Proceedings of 1990 SSPA-CTH-IIHR Workshop", Flowtech International Research Report, No 2, Githenburg,Swedwn,1991.

Larsson,L., Stern,F. and Bertram,V., "Benchmarking of Computational Fluid Dynamics for Ship Flows: The Gothenburg 2000 Workshop", Journal of Ship Research,47,No.1,pp 63-81,March 2003.

Lonjo. J., Stern,F. and Toda,Y., "Mean- Flow Measurements in the Boundary Layer and Wake and Wave Field of a Series 60 C_B=0.6 Ship Model-Part2: Scale Effects On Near Field Wave Patterns and Comparisons with Inviscid Theory". Journal of Ship Research,Vol. 37, No.1,pp 16-24,1993.

Mucientes, D.F., "Numerical Simulation of Free Surface Viscous Flows around Single and Multiple Hulls" ,M.S Thesis, Department of Mechanical and Aerospace Engineering, California State University,Long Beach, December, 2010.

Mulvany, N. J., Chen, L., Tu, J. Y. and Anderson, B., "Steady-State Evaluation of Two-Equation RANS (Reynolds-averaged Navier Stokes) Turbulence Models for High-Reynolds Number Hydrodynamic Flow Simulations",. Maritime Platforms Division, Defence Size and Technology Organization, Deparment of Defence, Australian Government, 2004.

Olivieri, A.,Pistani, F.,Avanzini, A.,Stern,F.and Penna, R., "Towing Tank Experiments of Resistance,Sinkage and Trim,Boundary Layer,Wake,and Free Surface Flow around a Naval Combatant Insean 2340 Model" IIHR Technical Report No.421,September 2001.

Ozdemir, Y. H., Bayraktar, S. and Yilmaz, T., " Computational Investigation of a Hull", 2nd International Conference on Marine Research and Transportation, Ischia, Naples, Italy, 28th-30th June, 2007.

Pranzitelli, A., Nicola,C.D. and Miranda,S., "Steady-State Calculations of Free Surface Flow around Ship Hulls and Resistance Predictions", IX HSMV Naples, 25-27 May ,2011.

Rahman, M. M, Application of Finite Volume Method for Solving Fluid Structure Interaction Problem, M.Phil Thesis, Department of Mathematics, Bangladesh University of Engineering and Technology (BUET), Dhaka, Bangladesh,2008.

Repetto, R.A., Computation of Turbulent Free-Surface Flows Around Ships and Floating Bodies, PhD. Thesis, Technical University Hamburg-Harburg, Argentina ,2001.

Rhee, S.H., "Unsteady ReynoldsAveraged Navier-Stokes Method for Free-Surface Wave Flows around Surface-Piercing Cylindrical Structures", Journal of Waterway,Port,Coastal and Ocean Engineering, 2009.

Rhee, S.H., Makrov,B.P. ,Krishinan ,H. and Ivanov,V., "Assessment of the Volume of Fluid Method for Free Surface Wave Flow",Journal of Marine Science and Technology,Vol.10, pp.173-180, 2005.

Saha, G.K., Numerical optimization of ship hull forms from viewpoint of wave making resistance based on panel method , P.H.D Thesis, Yokohama National University, Yokohama, Japan ,2004.

Sangseon, J., "Study of Total and Viscous Resistance for The Wigley Parabolic Ship Form", Iowa Institute of Hydraulic Research, IIHR Report No.261, 1983.

Schwabacher, G.J., Computational Fluid Dynamics Testing for Drag Reduction of an Aircraft Laser Turret, Masters thesis, Department of the Air Force, Air Force Institute of Technology, Air University, Wright-Patterson Air Force Base, Ohio, 2000.

Senocak, I and Iaccarino,G, "Progress towards RANS simulation of free-surface flow around modern ships", Center for Turbulence Research Annual Research Briefs, 2005.

Toda, Y., Stern, F. and Longo,L., "Mean- Flow Measurements in the Boundary Layer and Wake and Wave Field of a Series 60 C_B=0.6 Ship Model-Part1: Froude Numbers 0.1 and 0.316." Journal of Ship Research, Vol. 36, No.4, pp. 360-377, 1992.

Ungureanu, C., Lungu, A. and Maria,V. G., "Numerical Breaking Waves around a Surface Piercing NACA 0012 Hydrofoil", AIP Conference Proceedings,2011.

Versteeg, H. K. and Malalasekera, W., "An Introduction To Computational Fluid Dynamics- The Finite Volume Method", Longman Scientific & Technical, England, 1995.

Wanderely, J.B.V., Vitola,M., Sphaier, S.H.and Levi,C., "A Three-Dimensional Numerical Simulation of the Free Surface Flow Around A Ship Hull", Laboceano-COPPE/UFRJ, Brazil ,2011.

APPENDICES

Appendix A:

Verification of Friction Coefficient

Velocity $V = Fn \times \sqrt{gL}$

Reynolds Number $Re = \frac{(\rho v L)}{\mu}$

Coefficient of friction $C_f = \frac{0.075}{(\log_{10} Rn - 2)^2}$

Frictional Drag Coefficient $C_F = \frac{R_F}{0.5 \rho V^2 A}$

Viscous drag coefficient $C_V = (1+k)\, C_F$

Density ρ = 998.2 kg/m^3

Viscosity μ=0.001003 kg/m-s

Form factor k = 0.100

1. Fn =0.173, V=0.173× $\sqrt{9.81 \times 1}$ = 0.173×3.13 =0.54

   Re = (998.2×0.54×1.00)/ 0.001003 = 5.4 × 10^6

   $\log_{10}$ Re = 5.730

   $C_f = \frac{0.075}{(5.730 - 2)^2} = \frac{0.075}{13.91} = 5.39 \times 10^{-3}$

2. Fn =0.205, V=0.205× $\sqrt{9.81 \times 1}$ = 0.205×3.13 =0.64

Re = (998.2×0.64×1.00)/ 0.001003 = 6.4×10^6

$\log_{10}$ Re = 5.80

$$C_f = \frac{0.075}{(5.80-2)^2} = \frac{0.075}{14.44} = 5.19\times10^{-3}$$

3. Fn =0.267, V=0.267× $\sqrt{9.81\times1}$ = 0.267×3.13 =0.84

Re = (998.2×0.84×1.00)/ 0.001003 = 8.4×10^6

$\log_{10}$ Re = 5.92

$$C_f = \frac{0.075}{(5.92-2)^2} = \frac{0.075}{15.36} = 4.88\times10^{-3}$$

4. Fn =0.355, V=0.355× $\sqrt{9.81\times1}$ = 0.355×3.13 =1.11

Re = (998.2×1.11×1.00)/ 0.001003 = 1.1×10^7

$\log_{10}$ Re = 6.04

$$C_f = \frac{0.075}{(6.04-2)^2} = \frac{0.075}{16.32} = 4.60\times10^{-3}$$

5. Fn =0.476, V=0.476× $\sqrt{9.81\times1}$ = 0.476×3.13 =1.49

Re = (998.2×1.49×1.00)/ 0.001003 = 1.48×10^7

$\log_{10}$ Re = 6.17

$$C_f = \frac{0.075}{(6.17-2)^2} = \frac{0.075}{17.38} = 4.31\times10^{-3}$$

Appendix B:

Verification of Wigley Parabolic Hull

Data is provided for a Length=1m, Beam=0.1 m, Draft=0.0625 m and Block coefficient C_B =0.44.

Volumetric Displacement Δ = LBD C_B×1.00

= 1×0.1×0.0625×0.44

= 2.75×10^{-3} m^3

Wetted Surface Area A =$2.58\sqrt{\nabla L}$ = 0.135 m^2

0.5ρ A = 0.5×998.2×0.135 = 67.37

1. Fn = 0.173

$$C_F = \frac{\left(5.39\times10^{-3}\right)}{\left\{67.37\times(0.54)^2\right\}}$$

$= 0.274\times 10^{-3}$

C_V = (1+k)C_F

$=1.001\times 0.274\times 10^{-3}$

$= 0.274\times 10^{-3}$

2. Fn = 0.205

$$C_F = \frac{\left(5.19\times10^{-3}\right)}{\left\{67.37\times(0.64)^2\right\}}$$

$= 0.264\times 10^{-3}$

C_V = (1+k)C_F

$=1.001\times 0.264\times 10^{-3}$

$= 0.264\times 10^{-3}$

3. Fn = 0.267

$$C_F = \frac{\left(4.88\times10^{-3}\right)}{\left\{67.37\times(0.84)^2\right\}}$$

$$= 0.102\times 10^{-3}$$

$$C_V = (1+k)C_F$$

$$= 1.001\times 0.102\times 10^{-3}$$

$$= 0.102\times 10^{-3}$$

4. Fn =0.355

$$C_F = \frac{\left(4.60\times10^{-3}\right)}{\left\{67.37\times(1.11)^2\right\}}$$

$$= 0.056\times 10^{-3}$$

$$C_V = (1+k)C_F$$

$$=1.001\times 0.056\times 10^{-3}$$

$$= 0.056\times 10^{-3}$$

5. Fn= 0.476

$$C_F = \frac{\left(4.31\times10^{-3}\right)}{\left\{67.37\times(1.49)^2\right\}}$$

$$= 0.028\times 10^{-3}$$

$$C_V = (1+k)C_F$$

$$= 1.001\times 0.028\times 10^{-3}$$

$$= 0.028\times 10^{-3}$$

Appendix C:

Verification of Series 60 Hull

Data is provided for a Length=1m, Beam=0.1333 m, Draft=0.0533 m and Block coefficient C_B =0.60.

Volumetric Displacement Δ = LBD C_B×1.00

= 1×0.1×0.0625×0.44

= 4.26×10^{-3} m^3

Wetted Surface Area A =$2.58\sqrt{\nabla L}$ = 0.168 m^2

0.5ρ A = 0.5×998.2×0.168 = 83.84

1. Fn = 0.173

$$C_F = \frac{\left(5.39\times10^{-3}\right)}{\left\{83.84\times(0.54)^2\right\}}$$

$= 0.22\times 10^{-3}$

C_V = (1+k)C_F

$= 1.001\times 0.22\times 10^{-3}$

$= 0.22\times 10^{-3}$

2. Fn = 0.205

$$C_F = \frac{\left(5.19\times10^{-3}\right)}{\left\{83.84\times(0.64)^2\right\}}$$

$= 0.15\times 10^{-3}$

C_V = (1+k)C_F

$= 1.001\times 0.15\times 10^{-3}$

$= 0.15\times 10^{-3}$

3. Fn = 0.267

$$C_F = \frac{\left(4.88\times10^{-3}\right)}{\left\{83.84\times(0.84)^2\right\}}$$

$$= 0.08\times 10^{-3}$$

$$C_V = (1+k)C_F$$

$$= 1.001\times 0.08\times 10^{-3}$$

$$= 0.08\times 10^{-3}$$

4. Fn =0.355

$$C_F = \frac{\left(4.60\times10^{-3}\right)}{\left\{83.84\times(1.11)^2\right\}}$$

$$= 0.045\times 10^{-3}$$

$$C_V = (1+k)C_F$$

$$=1.001\times 0.045\times 10^{-3}$$

$$= 0.045\times 10^{-3}$$

5.Fn= 0.476

$$C_F = \frac{\left(4.31\times10^{-3}\right)}{\left\{83.84\times(1.49)^2\right\}}$$

$$= 0.023\times 10^{-3}$$

$$C_V = (1+k)\, C_F$$

$$=1.001\times 0.023\times 10^{-3}$$

$$= 0.023\times 10^{-3}$$

Appendix D:

Boundary Element Method(BEM)

The flow around a ship moving with a steady forward speed *U* under the influence of incoming waves defines a boundary value problem for the velocity potential.

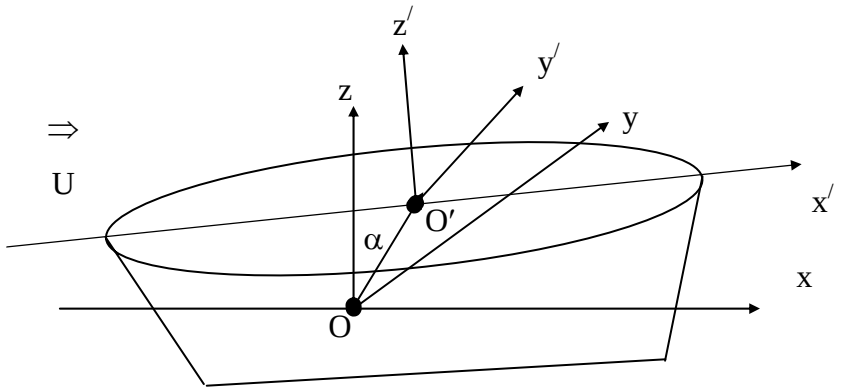

Figure: Co-ordinate system

The fluid is assumed to be inviscid and incompressible and the flow is irrotational such that the velocity potential Φ can be defined as

$$\Phi = U.x + \phi$$

The velocity potential Φ satisfies the Laplace equation

$$\nabla^2 \Phi = 0$$

The hull boundary condition requires that normal velocity potential on the hull must be zero.

$$\nabla \Phi \cdot n = 0$$

The kinematic and dynamic boundary conditions on the free surface can be respectively written as:

$$\Phi_x \zeta_x + \Phi_y \zeta_y - \Phi_z = 0 \quad \text{at} \quad z = \zeta$$

$$g\zeta + \frac{1}{2}\left[\nabla\Phi.\nabla\Phi - U^2\right] = 0 \quad \text{at} \quad z = \zeta$$

Combining the above two equations

$$\nabla\Phi.\nabla\left[\frac{1}{2}\left(\nabla\Phi.\nabla\Phi\right)\right] + g\Phi_z = 0 \quad \text{at} \quad z = \zeta$$

Wave Making Resistance using BEM

The pressure at any point on the hull surfaces $p - p_\infty = \frac{1}{2}\rho\left(\mathbf{U}^2 - \nabla\Phi\cdot\nabla\Phi\right) - \rho gz$

$\nabla\Phi = U + \nabla\varphi_1 + \nabla\varphi_2$ for 2nd order approximation

The hydrodynamic force in the x-direction is obtained by integrating the pressure over the instantaneous wetted hull surface as follows

$$R_W = -\int_{S+S'}(p - p_\infty)n_x dS$$

$$R_w = -\int_S\left[\frac{1}{2}\rho\left(U^2 - \nabla\Phi\cdot\nabla\Phi\right) - \rho gz\right]n_x dS - \int_{S'}\left[\frac{1}{2}\rho\left(U^2 - \nabla\Phi\cdot\nabla\Phi\right) - \rho gz\right]n_x dS$$

Where S is the mean wetted surface and S' is the fluctuating part of the wetted surface between still water plane , $z = 0$ and the waterline along the hull , $z = \zeta$.

S = mean wetted surface and S' = fluctuating part of the wetted surface

Pressure along the water line, $p = p_\infty$.

$$\frac{1}{2}\rho\left(U^2 - \nabla\Phi\cdot\nabla\Phi\right) = \rho g\zeta$$

The force on the hull surface in the x-direction can be expressed as

$$R_w = -\int_S\left[\frac{1}{2}\rho\left(U^2 - \nabla\Phi\cdot\nabla\Phi\right) - \rho gz\right]n_x dS - \int_{S'}\left(\rho g\zeta - \rho gz\right)n_x dz\, dL$$

After calculating the pressure coefficient on the hull surface , the wave making resistance coefficient can be obtained as

$$C_w = \frac{R_w}{\frac{1}{2}\rho S U^2}$$

Appendix E:

Comparison of Computed C_D by Various Turbulent Models

For Wigely Parabolic Hull

Different Froude Numbers(Fn)	Viscous Turbulent Models		
	Standard k- ε $C_D \times 10^{-3}$	Realizable k- ε $C_D \times 10^{-3}$	SST k-ω $C_D \times 10^{-3}$
0.173	1.91	2.96	2.19
0.205	2.30	3.52	2.55
0.267	3.12	4.66	3.41
0.355	4.24	6.10	4.59
0.476	6.13	8.31	6.57

For Series 60 Hull

Different Froude Numbers(Fn)	Viscous Turbulent Models		
	Standard k- ε $C_D \times 10^{-3}$	Realizable k- ε $C_D \times 10^{-3}$	SST k-ω $C_D \times 10^{-3}$
0.173	2.37	2.09	1.56
0.205	3.08	3.52	2.19
0.267	1.98	2.08	2.78
0.355	7.44	7.75	19.43
0.476	23.34	76.35	134.90

Computed Value of C_D, C_V and C_W by Standard k-ε(SKE) Model

For Wigely Parabolic Hull

Different Froude Numbers(Fn)	$C_D \times 10^{-3}$	$C_V \times 10^{-3}$	$C_W \times 10^{-3}$
0.173	1.91	0.30	1.60
0.205	2.30	0.29	2.01
0.267	3.12	0.11	3.01
0.355	4.24	0.06	4.18
0.476	6.13	0.03	6.10

For Series 60 Hull

Different Froude Numbers(Fn)	$C_D \times 10^{-3}$	$C_V \times 10^{-3}$	$C_W \times 10^{-3}$
0.173	2.37	0.24	2.13
0.205	3.08	0.16	2.92
0.267	1.98	0.09	1.89
0.355	7.44	0.05	7.39
0.476	23.34	0.03	23.31